

## APPROVAL SHEET

**Title of Thesis:** Comprehensive airborne in situ characterization of atmospheric aerosols: from angular light scattering to particle microphysics

**Name of Candidate:** W. Reed Espinosa  
Doctor of Philosophy, 2017

**Thesis and Abstract Approved:**



Dr. J. Vanderlei Martins  
Professor  
Department of Physics

**Date Approved:** Oct. 13, 2017

## ABSTRACT

Title of dissertation: COMPREHENSIVE AIRBORNE IN SITU  
CHARACTERIZATION OF ATMOSPHERIC  
AEROSOLS: FROM ANGULAR LIGHT  
SCATTERING TO PARTICLE MICROPHYSICS

W. Reed Espinosa

Directed by: Professor J. Vanderlei Martins  
Department of Atmospheric Physics

A comprehensive understanding of atmospheric aerosols is necessary both to understand Earth's climate as well as produce skillful air quality forecasts. In order to advance our understanding of aerosols, the Laboratory for Aerosols, Clouds and Optics (LACO) has recently developed the Imaging Polar Nephelometer instrument concept for the in situ measurement of aerosol scattering properties. Imaging Nephelometers provide measurements of absolute phase function and polarized phase function over a wide angular range, typically  $3^\circ$  to  $177^\circ$ , with an angular resolution smaller than one degree. The first of these instruments, the Polarized Imaging Nephelometer (PI-Neph), has taken part in five airborne field experiments and is the only modern aerosol polar nephelometer to have flown aboard an aircraft.

A method for the retrieval of aerosol optical and microphysical properties from I-Neph measurements is presented and the results are compared with existing measurement techniques. The resulting retrieved particle size distributions agree to within experimental error with measurements made by commercial optical particle counters.

Additionally, the retrieved real part of the refractive index is generally found to be within the predicted error of 0.02 from the expected values for three species of humidified salt particles, whose refractive index is well established.

A synopsis is then presented of aerosol scattering measurements made by the PI-Neph during the Studies of Emissions and Atmospheric Composition, Clouds and Climate Coupling by Regional Surveys (SEAC<sup>4</sup>RS) and the Deep Convection Clouds and Chemistry (DC3) field campaigns. To better summarize these extensive datasets a novel aerosol classification scheme is developed, making use of ancillary data that includes gas tracers, chemical composition, aerodynamic particle size and geographic location, all independent of PI-Neph measurements. Principal component analysis (PCA) is then used to reduce the dimensionality of the multi-angle PI-Neph scattering data and the results are examined as a function aerosol type. Strong clustering is observed in the PCA score space, corresponding to the ancillary classification results, suggesting a robust link between the angular scattering measurements and the aerosol type. Retrievals of the DC3 scattering data suggest the presence of a significant amount of mineral dust aerosol in the inflow of storms sampled during this campaign. The retrieved size distributions of all fine mode dominated aerosols measured during SEAC<sup>4</sup>RS were found to be remarkably similar. There were however consistent differences between the angular light scattering patterns of biomass burning samples and the other fine mode aerosols, which the GRASP retrieval attributed almost entirely to a higher real refractive index in the biomass burning samples.

COMPREHENSIVE AIRBORNE IN SITU CHARACTERIZATION OF  
ATMOSPHERIC AEROSOLS: FROM ANGULAR LIGHT SCATTERING TO  
PARTICLE MICROPHYSICS

by

W. Reed Espinosa

A DISSERTATION

Submitted to the Faculty Committee of University of Maryland Baltimore County  
in partial fulfillment of the requirements for the degree of

DOCTOR OF PHILOSOPHY

2017

ADVISORY COMMITTEE:

Dr. J. Vanderlei Martins (Chairman)

Dr. Zhibo Zhang

Dr. Todd Pittman

Dr. Lorraine Remer

Dr. Kirk Knobelspiesse





## Acknowledgments

It is difficult to overstate my appreciation for the guidance of my PhD advisor, Dr. Vanderlei Martins. His creativity and positive attitude always kept the group moving and provided a limitless stream of potential projects. This positivity was paired with a sharp, pragmatic approach that always managed to steer me away from dead ends in a way that never diminished my confidence in myself. His gift for compassionately motivating and guiding people was an indispensable resource throughout this work and I would not be the person I am today without it.

I want to thank Dr. Lorraine Remer for her sound scientific insight, encouragement and dedication to the publications on which most this dissertation is based. This work is founded in large part on the successes of Gergely Dolgos, who led the development of the first PI-Neph, and I am very grateful for his help. Over the course of my time at UMBC I would consistently find myself employing technical and philosophical approaches to instrument design that I first learned from Gergely. Lorraine and Gergely both served as mentors to me and this work would not have been possible without them.

I am indebted to the members of the LACO science team, whose help carried this work along throughout my graduate career. Dr. Daniel Orozco and I worked closely on many PI-Neph related projects and I am very grateful for the many labo-

ratory measurements he generously shared with me. Anin Puthukkudy helped with many of the PI-Neph retrievals and was instrumental in the development of the aerosol classification algorithm presented in this dissertation. I am also thankful for the comments and suggestions given by many other groups members, especially Dr. Adriana Lima, Dr. Henrique Barbosa, Dr. Roberto-Fernandez Borda and Brent McBride.

The engineering support of the LACO group has also been an indispensable resource for which I am extremely grateful. I especially want to thank John Hall whose competence and extra effort under pressure was critical to the early success of the OI-Neph instrument. Dominik Cieslak's general engineering support, as well as his gift for finding impossibly simple solutions to complex problems, was crucial in the construction and operation of both the PI-Neph and OI-Neph. Moreover, I've very grateful for the help in the design, construction and operation of these instruments that was provided by students employed by the group, especially Jitin Krishnan, Daniel Christner, Haotian Sun.

I would like to thank the LARGE group at NASA LANGLEY Research Center, who kindly helped us integrate the PI-Neph into their instrument rack during five different flight campaigns. Dr. Luke Ziemba and Dr. Andreas Beyersdorf were particularly helpful and I have always enjoyed working with them. I would also like to thank Dr. Oleg Dubovik and his team in at the University of Lille for helping us incorporate PI-Neph data into their GRASP retrieval algorithm. Additionally, I'm very thankful to Dr. Greg Schuster for giving me an opportunity to be part of the

STEAR project and for enlightening discussions regarding the application GRASP to PI-Neph data.

I am very thankful to the members of my PhD committee, Dr. Zhibo Zhang, Dr. Todd Pittman, Dr. Kirk Knobelspiesse, who have provided helpful insights throughout this process.

My coursework at UMBC provided me with many skills that I have used repeatedly in this work and I greatly appreciate the dedication and patience of all the members of the Physics faculty. I'm also thankful for insightful physics related discussions I have had with many of my fellow graduate students, particularly Dr. Jane Sprig, Dr. John Sullivan, Dr. Dan Jones and Tom Fenfert. The discussions I've had with Dr. Brian Kirby have been especially rewarding, and I'm extremely grateful for the strong friendship we have shared throughout graduate school.

I would like to thank my parents for doing everything in their power to raise me in an environment where I could thrive. They have always helped me to make wise choices, including the decision to go the graduate school, and I am forever grateful for this encouragement. Without their help this dissertation would not have been possible.

Finally, I want to thank my wife, Lauren Samuelson, for her compassion and patient support throughout my graduate school career. She has consistently been a source of motivation, especially when it was needed the most, and I would have surely given up long ago if not for her encouragement.

# Contents

**Abstract**

**Acknowledgments** **ii**

**1 Introduction** **1**

1.1 Aerosol Background 1

1.1.1 Overview of Aerosols 1

1.1.2 Microphysical and Optical Properties 3

1.2 Aerosol Impacts 7

1.2.1 Climate 7

1.2.2 Air Quality and Health 9

1.3 Measurements of Aerosol Scattering Properties 10

1.3.1 Passive Remote Sensing 10

1.3.2 Integrating Nephelometers 13

1.3.3 Optical Particle Counters 15

1.3.4	Polar Nephelometers	16
1.4	Organization of Dissertation	19
<b>2</b>	<b>Imaging Nephelometer Theory and Application</b>	<b>21</b>
2.1	Imaging Polar Nephelometer Implementations	21
2.1.1	Polarized Imaging Nephelometer	21
2.1.2	Open Imaging Nephelometer	25
2.1.3	Imaging Nephelometer Datasets	28
2.2	Basic Theory of Scattering Matrix Element Recovery	33
2.3	Instrument Calibration	36
2.4	Detailed Mathematical Model	40
2.4.1	Fundamental Assumptions and Equations	40
2.4.2	Calculation of Calibration Constants	45
2.4.3	Simplifying Assumptions	48
2.4.4	Finding Scattering Matrix Elements	50
2.4.5	Integrating Nephelometer $\xi$ Correction	53
2.4.6	Final Rayleigh Subtracted Aerosol Products	55
2.5	Estimating Errors	57
2.5.1	Systematic Calibration Errors	57
2.5.2	Time-dependent Errors	68
2.5.3	Future Approaches to Instrumental Error	72

<b>3 Retrievals of Aerosol Optical and Microphysical Properties from I-Neph Measurements</b>	<b>74</b>
3.1 Introduction	74
3.2 Inversion Methodology	77
3.2.1 Artificial Aerosol Generation	77
3.2.2 Ambient Measurements	79
3.2.3 Implementation of GRASP Retrieval	81
3.3 Retrieval Results and Discussion	84
3.3.1 Measured Data and Retrieval Fit	84
3.3.2 Refractive Index Retrievals	91
3.3.3 Size Distribution Retrievals	99
<b>4 Airborne in situ characterization of aerosols over the contiguous United States</b>	<b>105</b>
4.1 Introduction	105
4.2 Methodology	109
4.2.1 Instrumentation	109
4.2.2 Averaging of PI-Neph Measurements	111
4.3 Aerosol Classification Scheme	112
4.4 Measurement of Phase Matrix Elements	118
4.5 PCA Analysis	122
4.5.1 PCA Loadings and Scores	125

4.5.2	Identifying Types by Mahalanobis Distance	128
4.5.3	Identifying Types with a Dividing Plane	133
4.6	GRASP Retrievals	139
4.6.1	Retrieved Size Distributions	143
4.6.2	Retrieved Real Refractive Indices and Spherical Fractions	147
<b>5</b>	<b>Conclusions</b>	<b>152</b>
5.1	Overview of I-Neph Data Reduction and Error	153
5.2	Concluding Remarks on Retrievals of I-Neph Data	154
5.3	Summary of Geophysical Analysis	155
5.4	Topics of Future Study	157

# CHAPTER 1

## Introduction

### 1.1 Aerosol Background

#### 1.1.1 Overview of Aerosols

An aerosol is a suspension of solid or liquid particles that have negligible terminal fall speeds. In the atmosphere these particles can range in size from just a few molecules to bigger than the width of a human hair and are ubiquitous in almost all settings. In every natural environment on Earth there are millions of these particles in every cubic meter of air. Aerosols are produced either by direct emission or they can form as a result of gas phase reactions and photochemical processes [Hallquist et al., 2009], generally as secondary organic aerosol (SOA).

Approximately 90% of the aerosol mass in Earth's atmosphere comes from natural sources. Sea salt is the most abundant source of natural aerosol followed

by mineral dust [Tegen et al., 1997], which is emitted primarily from the desert regions. The constituents of both sea salt and dust aerosols tend to be relatively large, with particles with diameters larger than a  $1\mu\text{m}$  composing the majority of the mass [O'Dowd et al., 1997; Maring et al., 2003]. Biomass burning emissions, primarily from wildfire smoke, make up the next largest fraction of naturally emitted particles. Volcanos are also responsible for a notable portion of the total atmospheric aerosol, both from primary emissions of volcanic ash as well as particles that form as a result of gaseous sulfur dioxide emissions. Biogenic emissions can produce significant particle populations, especially in heavily vegetated regions. The bulk of biogenic particles are SOA resulting from the emissions of organic compounds like Isoprene [Carlton et al., 2009], although direct emissions of pollen, fungal spores and bacteria, often referred to as bioaerosols, can also contribute to particle populations [Ziemba et al., 2016].

The remaining 10% of atmospheric aerosol result primarily from anthropogenic sources. Fossil fuel combustion produces compounds, especially sulfur dioxide, which can react with water and other gasses to produce significant quantities of sulfate aerosols [Charlson et al., 1991]. In addition to natural causes, the quantity of biomass burning can be increased by human activity and deforestation can lead to land cover changes that alter mineral dust emissions. While anthropogenic particles are less abundant globally than their natural counterparts, they can dominate particle populations near and downwind of urban and industrial centers. In practice, it is also

common for aerosols to be mixtures of many different particles, resulting from a wide array of emission sources. For example, urban emissions and biological volatile organic compounds frequently interact to produce particles species that are not found when these ingredients are present in isolation [Ayres et al., 2015].

As global aerosol concentrations do not significantly increase over long periods of time, aerosol mass must be removed from the atmosphere at the same rate at which it is injected [Wallace and Hobbs, 2006]. Scavenging of particles by precipitation is the largest aerosol sink and is responsible for the majority of particles removed from the air [Radke et al., 1980]. Dry deposition, the gravitational settling of larger particles, is responsible for the removal of the bulk of the remaining particle mass [Petroff et al., 2008].

### **1.1.2 Microphysical and Optical Properties**

The geometric diameters of aerosol particles can range from a nanometer to as large as 100  $\mu\text{m}$ . It is common for a typical polydisperse, ambient aerosol to contain significant concentrations of particles whose sizes differ by two or three orders of magnitude. The shape of the particles may also vary significantly [Martins et al., 1998], although they are frequently assumed to be spheres or spheroids [Dubovik et al., 2006].

The aerodynamic diameter of a particle is an important concept in many aerosol applications. This quantity is defined as the diameter of a spherical water droplet with a settling velocity equivalent to the particle in question [Hinds, 1999].

This definition capitalizes on the fact that larger particles tend to be more strongly impacted by the surrounding air as they have a larger mass to surface area ratio than smaller particles. A departure from spherical shape and deviations from the density of water are the two factors that cause the aerodynamic diameter to diverge from geometric diameter [Hinds, 1999].

The chemical composition of an aerosol varies considerably, depending on its source and the environmental conditions since it experiences after being emitted. Aerosol constituents often include sulfates, nitrates, mineral dust, carbon and a wide range of organic compounds. While the chemical makeup is strongly related to the aerosol's source, most aerosols are heterogenous mixtures of many different constituents. These mixtures can occur inside a single particle (internal mixing) or an aerosol can be composed of many different particle types (external mixing). The mixing state of the aerosol does not significantly affect the properties of the light scattered by the particles [Malm and Kreidenweis, 1997; Pilinis et al., 1995], but it can influence the particles' ability to absorb radiation [Chylek and Wong, 1995; Martins et al., 1998; Jacobson, 2001]. The refractive index of the particles, which is determined by the aerosol's chemical composition, is frequently assumed to be a single value, even in the case of heterogenous mixtures.

In the case of most ambient aerosols, the particle size distribution (PSD), morphology and complex refractive index completely determine the optical properties of the aerosol in question. The most basic of these properties include scattering and

absorption. The extinction coefficient—the sum of the scattering and absorption coefficients—is often integrated over the entire atmospheric column to obtain aerosol optical depth (AOD). This quantity corresponds to the e-folding length of the decrease in power of a light beam passing through the aerosol. The single-scattering albedo (SSA), which is equal to ratio of scattering and extinction, is another frequently cited quantity.

The angular dependence of the light scattered by an aerosol is represented by the phase function  $F_{11}(\Omega)$  [Thomas and Stamnes, 2002]. If polarization is of interest, the incoming and scattered radiation can be represented by two Stokes vectors representing the polarization state of the light [Mishchenko et al., 2002]. The phase function is the first element of a 4x4 matrix known as the scattering matrix that relates the incident Stokes vector to the scattered Stokes vector at a given scattering angle. If an aerosol contains many randomly oriented particles (i.e. their orientation distribution is uniform) symmetry relations can be used to reduce the scattering matrix to ten independent elements [Mishchenko et al., 2002]

$$\mathbf{F} = \begin{pmatrix} F_{11} & F_{12} & F_{13} & F_{14} \\ F_{12} & F_{22} & F_{23} & F_{24} \\ -F_{13} & -F_{23} & F_{33} & F_{34} \\ F_{14} & F_{24} & -F_{34} & F_{44} \end{pmatrix}. \quad (1.1)$$

This matrix can be further reduced to only six independent elements if each

particle has an equal number of mirror symmetric particles or if each particle has at least one plane of symmetry. These assumptions guarantee that an aerosol is macroscopically isotropic and mirror-symmetric and therefore has a scattering matrix of the form

$$\mathbf{F} = \begin{pmatrix} F_{11} & F_{12} & 0 & 0 \\ F_{12} & F_{22} & 0 & 0 \\ 0 & 0 & F_{33} & F_{34} \\ 0 & 0 & -F_{34} & F_{44} \end{pmatrix}. \quad (1.2)$$

The assumptions producing  $\mathbf{F}$  are valid for most realistic atmospheric aerosols and will be assumed throughout the rest of this work. It is also common to express scattering matrix elements in terms of the ratios  $F_{ij}/F_{11}$ . In this work the second element of the scattering matrix will generally be expressed as  $-F_{12}/F_{11}$ , a quantity frequently referred to as degree of linear polarization (DOLP). Intuitively, the magnitude of this quantity represents the fraction of the scattered light that is linearly polarized if the particles are illuminated by an unpolarized source and the scattering matrix takes the form of Equation 1.2. A positive DOLP value indicates that the predominant polarization state of the scattered light is perpendicular to the scattering plane, while a negative value indicates a polarization state that is predominantly parallel to the scattering plane.

## 1.2 Aerosol Impacts

Aerosols, clouds, and their interaction play a key role in the climate of our planet and the health of its inhabitants. Atmospheric particulates can directly affect Earth's energy balance through the scattering and absorption of light [Bellouin et al., 2005], as well as serve as cloud condensation nuclei (CCN), leading to changes in cloud properties and precipitation patterns [Rosenfeld et al., 2008]. The most recent Intergovernmental Panel on Climate Change (IPCC) assessment identifies both aerosols' direct and indirect effects as the two largest uncertainties of all anthropogenic radiative forcing components [Stocker, 2014]. In addition to the effects on climate, the inhalation of atmospheric aerosols can have a significant negative impact human health [Pope et al., 2002]. Despite the importance of these particles, accurate in situ measurement of their optical and microphysical properties has remained a significant challenge. A review of current measurement techniques will be provided in Section 1.3.

### 1.2.1 Climate

Aerosols interact with incoming solar radiation directly through scattering and absorption [McCormick and Ludwig, 1967; Coakley Jr et al., 1983], as well as indirectly by serving as cloud condensation nuclei [Twomey, 1977; Albrecht, 1989]. Moreover, the absorption of radiation by an aerosol can alter the temperature profile of the atmosphere causing changes in cloud formation, a process known as the semi-direct

effect [Hansen et al., 1997; Ackerman et al., 2000]. These mechanisms can produce meaningful perturbations in the the top-of-atmosphere (TOA) and surface radiation fluxes. The resulting direct and indirect changes in irradiance resulting from human activity—a quantity known as the aerosol climate forcing—are estimated to be quite large but contain significant uncertainties. The most recent report published by the Intergovernmental Panel on Climate Change states that the net TOA aerosol climate forcing may have a cooling effect of  $-0.82 \text{ Wm}^{-2}$ , which is comparable in magnitude to the positive forcing of carbon dioxide ( $+1.68 \text{ Wm}^{-2}$ ) [Stocker, 2014]. Despite their potential significance, the uncertainties on both direct and indirect aerosol forcings remain close to as large as the effects themselves, making them the single largest source of uncertainty among all anthropogenic radiative forcing components [Stocker, 2014].

Remote sensing and in situ measurements as well as modeling simulations can all help to improve our understanding of aerosol radiative effects. Advances in measurement techniques have the potential to better constrain the global distribution of aerosol AOD as well as their properties (SSA and  $F_{ij}$ ), both of which have significant temporal and spatial variability. As the availability of space-based remote sensing data increases it becomes possible to shift from model-based estimates of aerosol climate forcing to techniques that rely primarily on measurements, falling back on model simulations only when observational datasets are not available [Yu et al., 2006]. Measurements from ground-based remote sensing and in situ measurements from field

campaigns then become crucial both to constrain the assumptions required by the satellite instruments as well as evaluate the results of the models [Yu et al., 2006]. For example, overly general or incorrect aerosol assumptions may drive the differences found between leading space-based AOD retrievals [Mishchenko et al., 2009].

### 1.2.2 Air Quality and Health

The inhalation of aerosols is known to increase the prevalence of a range of health problems. Numerous studies have linked exposure to airborne particulate matter (PM) to premature death in people with heart or lung disease, nonfatal heart attacks, decreased lung function as well as increased respiratory symptoms such as asthma, coughing and difficulty breathing [Atkinson et al., 2010; Meister et al., 2012; Correia et al., 2013]. Moreover, it is estimated that 5% of all lung cancer deaths are attributable to PM exposure [Fang et al., 2013]. These negative health impacts are thought to be responsible for over two million premature deaths every year [Shah et al., 2013]. The depth at which a particle penetrates the respiratory system is strongly dependent on the aerodynamic diameter of the aerosol. Particles with aerodynamic diameters greater than  $10\mu\text{m}$  are generally deposited in the nasal passages or pharynx, while particles with aerodynamic diameters smaller than  $1\mu\text{m}$  can reach the bronchioli and alveoli of the lungs [Löndahl et al., 2006]. The US Environmental Protection Agency (EPA) regulates aerosols primarily based on two metrics: 1) the mass concentration of ground level coarse particulate matter with aerodynamic

diameters less than  $10\mu\text{m}$  ( $\text{PM}_{10}$ ) and 2) the mass concentration of fine particulate matter with aerodynamic diameters less than  $2.5\mu\text{m}$  ( $\text{PM}_{2.5}$ ) [Esworthy, 2013].

Historically, measurements of  $\text{PM}_{2.5}$  and  $\text{PM}_{10}$  have been provided by ground monitoring networks but the application of space-based remote sensing to air quality studies has advanced significantly in recent years [Hoff and Christopher, 2009]. As satellite measurements are typically representative of the entire atmospheric column, the derivation of ground level PM requires assumptions about the vertical distribution of aerosols. Inaccuracies in these assumptions, along with challenges associated with the conversion of an optical measurement into aerosol mass, drive the bulk of the error in space-based retrievals of air quality [Liu et al., 2005]. LIDAR extinction profiles can be used to constrain the vertical dependence [Chu et al., 2015] of the aerosol, but global coverage is not practical with this approach. Advanced techniques, like the use of a global chemical transport model (CTM) to determine  $\text{PM}_{2.5}/\text{AOD}$  ratios [Van Donkelaar et al., 2010], have also be used to address these challenges but significant assumptions regarding aerosol behavior are still required.

## 1.3 Measurements of Aerosol Scattering Properties

### 1.3.1 Passive Remote Sensing

A wide range of methods exist to remotely measure the solar radiation scattered by aerosols, with one of the most accurate approaches being ground-based remote sensing by sun photometers and sky radiometers [Remer et al., 1997]. This approach,

specifically in the form a global array of sun photometers known as the Aerosol Robotic Network (AERONET), has been used extensively to characterize aerosols and validate space-based observations. These instruments are capable of high accuracy measurements of AOD ( $\pm 0.01$ ) and, under the right conditions, can retrieve aerosol size, complex refractive index and fraction of spherical particles [Holben et al., 1998; Dubovik et al., 2000]. While this method is remarkably accurate, it is not feasible to make high resolution measurements across the globe using this technique alone. Climate, air quality and ocean color studies frequently require aerosol information on a global scale, with spatial resolutions on the order of a few km and time resolutions on the order of days or less. In order to meet these data requirements, the community must turn to space-based observations and model simulations.

A wide range of instrumentation, with sensitivities ranging from thermal infrared [Pierangelo et al., 2004] to ultraviolet [Torres et al., 2007] wavelengths, have been used to study aerosols from space. As a result of their near daily global coverage and high-quality dataset the two Moderate Resolution Imaging Spectroradiometers (MODIS) have become an indispensable space-borne tool for the aerosol community. The paper introducing the instruments' first operational aerosol retrieval algorithm [Remer et al., 2005] has almost 2000 citations, with data uses ranging from IPCC reports [Stocker, 2014] to chemical transport models [Zhang et al., 2008]. MODIS is succeeded by the Visible Infrared Imaging Radiometer Suite (VIIRS), which was launched in 2011 [Lee et al., 2006]. As the MODIS instruments are nearing the end

of their expected life, high quality aerosol retrievals from VIIRS will be essential to continue the climate data record [Levy et al., 2015].

MODIS and VIIRS both measure TOA radiance over a range of visible and infrared wavelengths at a single view angle for each pixel on earth. This single view angle produces significantly less information content than multi-angle instruments like AERONET. This challenge, along with the need to correct for surface contributions, means that inversions designed to retrieve aerosol properties from MODIS and VIIRS data have to make significant assumptions about the aerosol in question. Other instrumentation, like the Multi-angle Imaging SpectroRadiometer (MISR), attempt to reduce the number of assumption required by measuring radiances from several angles simultaneously, usually at the expense of spatial coverage [Diner et al., 1998]. However, accurate recovery of aerosol properties with few assumptions is difficult from space, even given multi-angular data. It is this fact that has steered the Earth science community toward sensors that both measure at multiple angles *and* have sensitivity to the polarization of the incoming radiation [Mishchenko et al., 2004].

The first space-based aerosol sensor, capable of measuring polarization, was the French Polarization and Directionality of the Earth's Reflectances (POLDER) instrument [Deuzé et al., 2001]. Several versions of the POLDER instrument have been carried aboard multiple satellites since 1996, with the last instrument ending data collection in 2013. The National Aeronautic and Space Administration (NASA) developed the Advanced Polarimetric Sensor [Mishchenko et al., 2007], based on the

concept of the successful, aircraft based Research Scanning Polarimeter (RSP) [Cairns et al., 1999], but the instrument was lost during a launch failure in 2011. The Hyper-Angular Rainbow Polarimeter (HARP) is a CubeSat, which has been funded by NASA and developed at the University of Maryland, Baltimore County (UMBC), that is scheduled to begin acquiring data in early 2018. Another NASA satellite, the Multi-Angle Imager for Aerosols (MAIA), will have polarimetric capabilities and is scheduled for launch in the early 2020's [Liu and Diner, 2017]. Additionally, the Multi-viewing Multi-channel Multi-polarization Imaging Mission (3MI), led by the European Organization for the Exploitation of Meteorological Satellites (EUMETSAT), is scheduled to begin collecting data at some point between 2020 and 2040 [Marbach et al., 2013]. In addition to these space-based sensors, a variety of instrumentation has been developed to measure polarized radiance from an aircraft [Cairns et al., 1999; Diner et al., 2013].

### 1.3.2 Integrating Nephelometers

The goal of the integrating nephelometer is to produce a signal that is nearly proportional to the light scattering coefficient  $\beta_{sca}$  of the sampled medium over a pre-determined spectral range. The device was originally developed to aid in visibility estimates, especially for military applications [Charlson et al., 1969], but has come to be used frequently in climate [Bates et al., 2006] and air quality related research [Cabada, 2004]. The attenuation of visible radiation in the atmosphere is frequently

dominated by scattering, making accurate scattering coefficient measurements crucial to accurate radiative transfer simulations in model simulations. The scattering coefficient is also directly proportional to the particle number concentration of the sampled aerosol, making it a reasonable proxy for air quality. The spectral dependence of the scattering coefficient can also often provide information about the size of the sampled particles [Ångström, 1929].

Typical integrating nephelometer configurations have a detector and a light source placed at right angles to each other. Ideally, the detector field of view is sufficiently limited such that only scattered light contributes to the signal. This is typically achieved by collimating either the detector field of view or the light emitted from the source, with the former being implemented more frequently [Heintzenberg and Charlson, 1996]. In the setup employing a collimated detector field of view a shutter is frequently employed at the light source that can be used to block the light being scattered toward the detector at less than  $90^\circ$ . This allows for measurements of both the total scattering coefficient as well as the back scattering fraction.

The scattering coefficient is equal to the integral over all solid angles of the angular intensity function  $F_{11}(\Omega)$ . If we assume a macroscopically isotropic and mirror-symmetric medium the phase function has azimuthal symmetry  $F_{11}(\Omega) = F_{11}(\theta)$  and the scattering coefficient can be described by

$$\beta_{sca} = \frac{1}{2} \int_0^\pi F_{11}(\theta) \sin(\theta) d\theta \quad (1.3)$$

where  $F_{11}$  has units of  $Mm^{-1}sr^{-1}$  and  $\beta_{sca}$  has units of  $Mm^{-1}$  [Thomas and Stamnes, 2002]. Integrating nephelometers lack detailed post measurement information about the angular dependence of the scattered light so the weighting in the above integral must be built into the instruments response [Anderson and Ogren, 1998]. In the case of a detector with a well-collimated field of view the geometry combined with an isotropic (Lambertian) light source produces the desired sinusoidal weighting [Anderson et al., 1996]. Small angular inhomogeneities in the light source as well as practical limits on the angular range of integration (truncation) can lead to errors that are typically on the order of 10%. In the case of large particles, with diameters greater than  $1\mu\text{m}$ , and highly absorbing aerosols these errors can exceed 50% [Anderson et al., 1996; Bond et al., 2009].

### 1.3.3 Optical Particle Counters

The primary product of optical particle counters (OPCs) is aerosol size distribution but this result is derived from a single particle light scattering measurement. Optical techniques of particle sizing capitalize on the approximately monotonic increase in the amount of light scattered by a single particle as a function particle size [Baumgardner et al., 1992]. In most designs, a trigger laser is used to detect the presence of a particle in the sample volume at which point a second focused laser pulse is used to illuminate the particle. The resulting scattered light is then collected over some angular range, often around  $4^\circ$  to  $13^\circ$  [Wendisch et al., 1996; Pinnick et al., 2000] or roughly  $30^\circ$  to

150°[Cai et al., 2008] in so called wide angle OPCs. OPCs can have sensitivity to particles from 50nm to as large as 50 $\mu$ m depending on design and collector gain settings.

If the refractive index and morphology of the particle is assumed the size of the particle can be estimated from the strength of the detected signal [Baumgardner et al., 1992]. When the measured particles are assumed to be homogeneous spheres with a refractive index equal to water this size measurement is often referred to as the “optically equivalent diameter”. Recently, instrumentation has been developed that collects scattering light from two angular regions separately [Baumgardner et al., 2001], often incorporating polarization sensitivity as well [Glen and Brooks, 2013]. The added information available in these measurements permits a reduction in the number of assumptions required regarding morphology or refractive index but they are generally limited to larger particles, typically diameters over around 500nm [Baumgardner et al., 2014]. Retrievals of particle properties from polarized, multi-angular in situ scattering measurements will be examined further in Chapter 3.

#### **1.3.4 Polar Nephelometers**

Polar nephelometers make measurements of one or more of the 16 elements of the scattering matrix at multiple scattering angles. This measurement is generally achieved by placing a detector at the various angular locations relative to the direction of a well collimated light source illuminating a small sample volume. A laser is used to illumi-

nate the aerosol in almost all polar nephelometer applications and it can be shown that the scattering profiles produced by a Gaussian beam are almost indistinguishable from those produced by a plane wave, as long as the beam waist is significantly larger than the particle diameter [Colak et al., 1979]. Typically polar nephelometer measurements are taken on ensembles of particles but several polar nephelometers have been designed to study the scattering patterns of single particles [Aptowicz et al., 2013; Kaye et al., 1992; Bacon and Swanson, 2000; Pluchino, 1987]. The angular extent of the measurement varies with different instruments but rarely extends below  $5^\circ$  or above  $175^\circ$  in zenith scattering angle. Angular resolutions range from less than a degree [Volten et al., 2001] to around five degrees [Chamberlain-Ward and Sharp, 2011].

A wide range of techniques are implemented in polar nephelometer measurements, each providing different advantages and drawbacks. The common goniometer-type polar nephelometer [Muñoz et al., 2011; Schnaiter and Wurm, 2002; Volten et al., 2001; Zhao, 1999; Sassen and Liou, 1979; Hunt and Huffman, 1973; Holland and Draper, 1967] makes use of a single detector that can be rotated about the sample volume relative to the incident light source. This approach has the advantage of permitting measurements with very high angular resolution, as the detector can be stepped by any desired amount, but a stable sample is required for a relatively long period while the detector is moved across all required angles. Multi-detector designs [Dick et al., 2007; Gayet et al., 1997; West and Doose, 1997; Leong and Jones, 1995;

Pluchino, 1987] make use of many detectors, allowing for a near instances measurement at the expense of angular resolution. Other instruments make use of large, reflective optics that partially surround the sample volume and focus the scattered light onto an imaging sensor [Aptowicz et al., 2013; Castagner and Bigio, 2007; Kaller, 2004; Kaye et al., 1992]. The only commercially available polar nephelometer combines a narrow viewing angle with wide angled light source. In this instrument, the angles covered by the light source are varied and differences in the resulting sensor counts can be used to infer the angular scattering over a relatively narrow range [Chamberlain-Ward and Sharp, 2011].

A new polar nephelometer concept called the Imaging Nephelometer (I-Neph) has been advanced significantly in the past decade. The Imaging Nephelometer uses a wide field of view charge coupled device (CCD) camera and refractive lens to image the light scattered by aerosols across the path of a high-powered continuous wave laser. This setup permits the construction of an instrument that is compact and stable enough to be flown on a variety of airborne platforms, while still allowing for measurements of scattering matrix elements over an angular resolution and range that is comparable to the best laboratory techniques [Muñoz et al., 2011]. While the early use and development of Imagining Nephelometers was primary limited to the Laboratory for Aerosols, Clouds and Optics (LACO) group at UMBC [Dolgos and Martins, 2014], other research groups have recently begun implementing the concept [Bian et al., 2017]. This measurement technique, its implementation and the analysis

of the corresponding data products will be the primary subject this dissertation.

Prior to the introduction of the I-Neph instrumentation the use of polar nephelometers has been primarily limited to ground measurements, despite explicit calls for a high quality airborne polar nephelometer for validation of space-based imagery [Mishchenko et al., 2007]. The first instrument to measure the angular dependence of light scattering in situ from aboard an aircraft [Grams et al., 1975] was last active in the 1970's. Until the introduction of Imaging Nephelometers in late 2011, this was the only airborne polar nephelometer constructed specifically to measure atmospheric aerosols. A second polar nephelometer, introduced by Gayet et al. [1997], has been flown extensively [Gayet et al., 1998; Auriol et al., 2001; Baran et al., 2005] but was originally designed to measure cirrus ice crystals. This instrument was adapted to measure aerosol particles produced by volcanic degassing plumes, but the resulting measurements were limited to particles large than  $1\mu\text{m}$  [Shcherbakov et al., 2016]. To the author's knowledge, no other measurements of scattering matrix elements have been made from aboard an aircraft.

## 1.4 Organization of Dissertation

The details of Imaging Nephelometer design, the corresponding theory and a description of the first two instruments to implement the technique is presented in Chapter 2. This chapter begins with a detailed description of the instrumentation as well as a summary of the various experiments for which they have collected data.

It then presents a high level theoretical model of these instruments, including the calibration procedure, data processing methodology, and error estimation. Chapter 3 explores the prospect of retrieving aerosol refractive index as well as microphysical properties from I-Neph measurements. This chapter concludes with a comparison of the retrieved parameters with measurements that have been reported elsewhere in the literature or measured by other instrumentation in parallel to the PI-Neph. In Chapter 4 datasets from two large field experiments are explored in detail. An aerosol classification scheme, making use of parameters that are independent of aerosol optical properties, is developed to identify the different aerosol types measured during the two deployments. Principal component analysis (PCA) is then used to reduce the dimensionality of the multi-angle I-Neph scattering data and the results are examined as a function aerosol type. The retrieval method of Chapter 3 is then applied to the I-Neph measurements and the results are summarized according the optically independent classification scheme. Chapter 5 provides a summary of the results of this work as well as suggestions for future studies.

## CHAPTER 2

# Imaging Nephelometer Theory and Application

### 2.1 Imaging Polar Nephelometer Implementations

#### 2.1.1 Polarized Imaging Nephelometer

The first field instrument to realize the Imaging Nephelometer concept was the Polarized Imaging Nephelometer (PI-Neph). The PI-Neph uses a wide field of view imaging system to measure the angular dependence of light scattered by aerosols and the surrounding atmospheric gases. The sample is illuminated by a high-powered continuous wave laser that is folded at the end of the sample chamber, very close to the CCD camera. This folding of the beam allows the forward and backward scattering angles to be captured in volumes that are physically adjacent to each other, reducing

the overall length of the instrument. While this design permits a physical footprint small enough to fit inside the limited space of an aircraft cabin it also introduces the need for separate calibrations of both the forward and backward scattering angles. In a typical measurement, the light scattered by the sample is imaged twice by a CCD camera, once for each of two roughly orthogonal linear polarization states of the laser. Originally the PI-Neph utilized only one laser operating at 532nm, but in 2013 two additional lasers were incorporated into the instrument, adding measurements at 473nm and 671nm.

A detailed schematic of the PI-Neph design is shown in Figure 2.1. The aerosol sample inside the PI-Neph is illuminated sequentially by a three-wavelength laser system (in the post 2013 configuration) operating at 473nm, 532nm and 671nm. The three beams are aligned by a system of dichroics and mirrors before having their polarization state precisely oriented by a Glan-Taylor linear polarizer. A liquid crystal variable retarder (LCVR) and Fresnel Rhomb are then used to actively rotate the polarization state of laser light. After exiting the rhomb the beam is guided, by two mirrors, through a window into a 10 liter, sealed chamber containing the aerosol sample. The laser light traverses the length of the chamber before a corner cube retroreflector redirects the beam back into a beam trap adjacent to the entry window. The light scattered by the aerosol and surrounding gas is then imaged twice by the CCD camera, once for each of two roughly orthogonal linear polarization states of the laser.

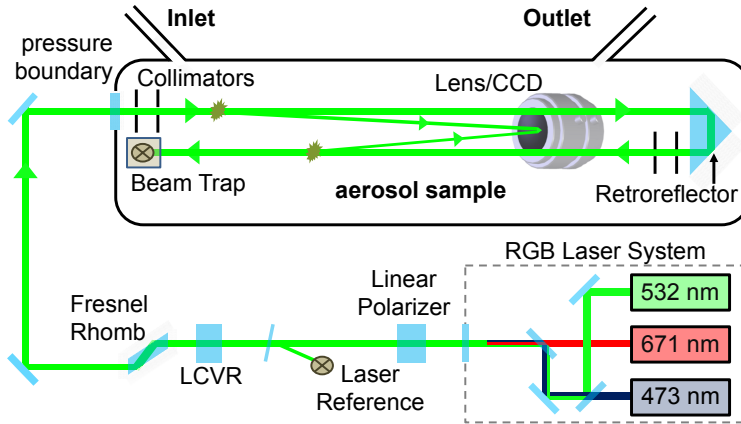


Figure 2.1: The PI-Neph instrument concept. Figure adapted from Dolgos and Martins [2014].

If the scattering medium is assumed to be macroscopically isotropic and symmetric the scattering matrix elements  $F_{13}$  and  $F_{14}$  do not contribute to the total scattered signal and the resulting pair of image intensities allows for direct measurements of  $F_{11}(\theta)$  as well as  $F_{12}(\theta)$ , with  $\theta$  representing the zenith scattering angle (azimuthal symmetry is implied by the assumption of a macroscopically isotropic and symmetric medium). The incorporation of calibration data derived from molecular scatterers ( $CO_2$  and  $N_2$ ) that are well characterized [Anderson et al., 1996; Young, 1980] allows for an angular dependent calibration that produces direct measurements of absolute phase function in known units (ex.  $Mm^{-1}sr^{-1}$ ), free from truncation error. Assumptions regarding the relative scattering contribution of the extreme angles can then be used to estimate total integrated scattering ( $\beta_{sca}$ ) from the truncated measurements of absolute phase function. The calibration and data reduction process is described in detail in Sections 2.2 through 2.4 of this dissertation.

The angular resolution of the measurement is limited by the resolution of the CCD camera, as well as the size of the camera’s aperture. The resulting raw resolution varies as a function of scattering angle ( $0.1^\circ < \Delta\theta < 1^\circ$ ) but the final results are always binned to one degree. The angular range of the instrument is primarily limited by stray light emanating from the points where the laser beam enters and exits the sample chamber. Stray light can vary significantly with instrument alignment, but an angular range of  $3^\circ$  to  $177^\circ$  in zenith scattering angle is frequently achieved. The raw sampling rate of the instrument varies with configuration, but generally ranges from a few seconds to just under a minute. The final products are then reported at standard temperature and pressure, with the Rayleigh scattering contribution from the surrounding gases subtracted. Additionally, when phase functions are normalized in this work they are represented by  $\tilde{F}_{11}$  and are scaled such that  $\tilde{F}_{11}(30^\circ) = 1$ .

PI-Neph measurements have been validated by a variety of methods since the instrument’s completion in the summer of 2011. Measurements of monodisperse polystyrene latex (PSL) spheres have yielded results that are in excellent agreement with Mie theory, while scattering coefficient measurements made in parallel with commercially available integrating nephelometers have agreed to within 5%. A detailed summary of the PI-Neph’s physical design and validation can be found in Dolgos and Martins [2014].

### 2.1.2 Open Imaging Nephelometer

The inlet, tubing and sample chamber that is present in almost all airborne aerosol instrumentation can induce size and relative humidity dependent biases in the measured aerosol properties. Non-idealities and turbulence at the inlet have been shown to result in significant losses of coarse mode particles [Pena et al., 1977; McNaughton et al., 2007]. Temperature gradients prevent measurements from being made under ambient humidity conditions and drying and rehumidifying particles can often produce changes in particle shape and structure. These factors emphasize the strong need for measurements of undisturbed aerosols if the community is going to confidently validate remote sensing retrievals and further enhance our understanding of Earth's climate forcing. The Open path polar Imaging Nephelometer (OI-Neph) is an exceptional tool for the measurement of large aerosol and hygroscopic particles that are particularly susceptible to the biases induced by contained sampling apparatuses.

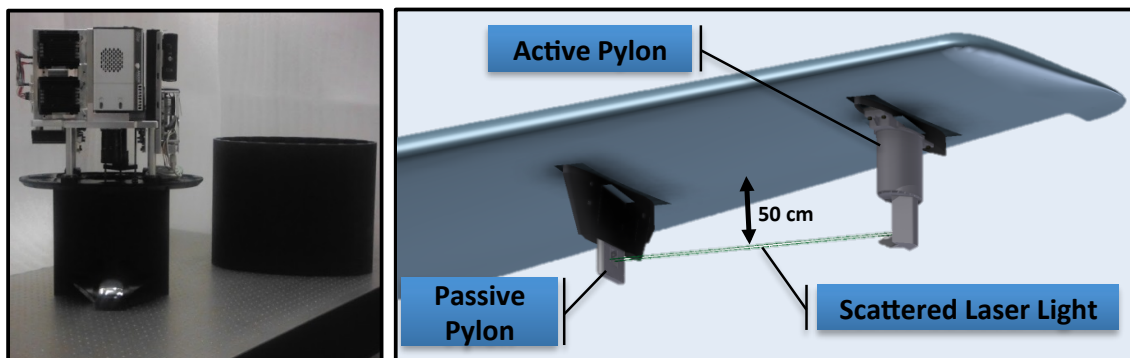


Figure 2.2: The mechanical assembly of the OI-Neph's active pylon (left) and a 3D markup of the entire system mounted to the wing of NASA's P3 aircraft (right).

The OI-Neph capitalizes on the simplicity of the Imaging Nephelometer design and removes the enclosure required by almost all in-situ instruments, providing significant physical distance between the sample and instrument body. This allows for airborne measurements of aerosols and cloud particles in their native state without significant distortion of the ambient sample. The OI-Neph consists of a laser beam passing between two pylons, under the wing, one “passive” housing a reflecting mirror and the other “active” containing the bulk of the electronics and optics (see Figure 2.2). These pylons have been designed to safely mount on the wing of NASA’s P3 aircraft, with adaptation to other aircraft only requiring the fabrication of a new intermediary plate.

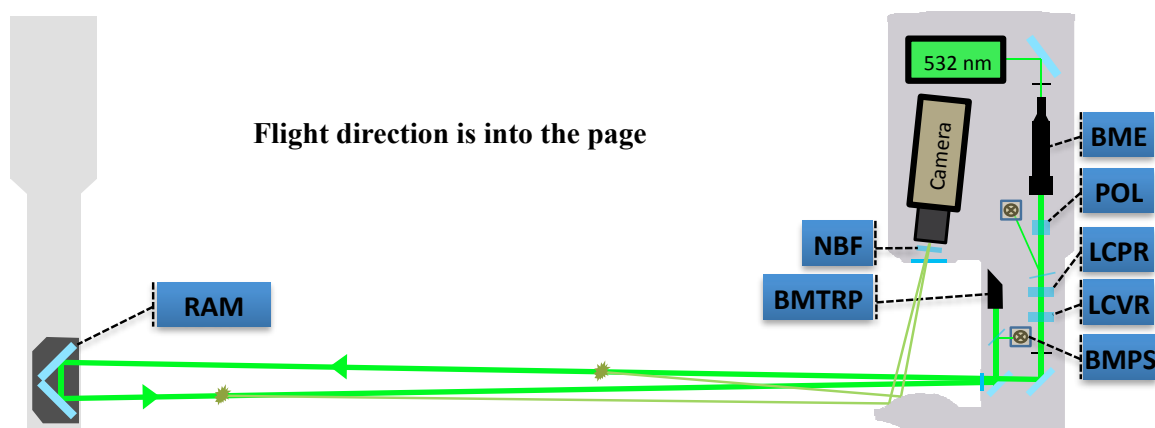


Figure 2.3: The optical layout of the OI-Neph instrument.

The optical layout of the OI-Neph is portrayed in Figure 2.3. The aerosol sample is illuminated by a pulsed laser operating at 532 nm. A beam expander (BME) is used to enlarge the sample area and enhance statistics in aerosols with very low particle concentrations. The expanded beam is passed through a Glan-Taylor

Calcite Polarizer (POL) to precisely align the polarization orientation and then two liquid crystals (LCVR and LCPR) allow for active variation of the polarization state of the beam. The laser is fold by a right-angled mirror system (RAM) located on the passive pylon and then the bulk of the laser energy is deposited into a beam trap (BMTRP), with the remaining portion being directed onto a beam position sensor (BMPS) used to track the alignment of the system. A synchronized camera located within the active pylon is then used to measure the intensity of the light scattered by particles between the two pylons. A custom built cylindrical mirror at the base of the active pylon is incorporated into the imaging optics and allows for consistency in system's polarization state as well as ensures that the stable, relatively dark wing is always the backdrop of the image. A narrow band filter (NBF), tuned to laser's wavelength, further mitigates the solar background.

The OI-Neph's optical design allows for measurements of the entire first row of the scattering matrix with an angular range comparable to the PI-Neph. Measured values of zero for the elements  $F_{13}$  and  $F_{14}$  will indicate a breakdown in the common assumption of azimuthal symmetry in scattering, which is known to be invalid for many cirrus clouds [Borovoi and Grishin, 2003]. Simple, relatively inexpensive upgrades to the detection system will permit measurement of all 16 scattering matrix elements.

The physical structure of the instrument has been carefully designed to maximize the robustness of the measurement. The faces of the instrument body have been

angled away from the sample volume. This has been shown to significantly reduce the biases caused by shattering of ice crystals [Korolev et al., 2011]. The internal portion of the active pylon is pressurized and thermally stabilized to provide measurement consistency under a diverse range of flight conditions. The position of the laser beam is stabilized against wing movement with a real-time beam steering system, capable of responding on sub-millisecond timescales.

### **2.1.3 Imaging Nephelometer Datasets**

#### **Flight Data**

Imaging Nephelometers have taken part in five airborne deployments over North America resulting in over 500 flight hours of data. The first field experiment the PI-Neph took part in was the Development and Evaluation of satellite ValidatiOn Tools by Experimenters (DEVOTE) campaign in the fall of 2011, followed by the Deep Convection Clouds and Chemistry (DC3) in May and June of 2012. In the winter of 2013 the PI-Neph was flown aboard the P-3 aircraft as part of the California deployment of the Deriving Information on Surface Conditions from Column and Vertically Resolved Observations Relevant to Air Quality (DISCOVER-AQ) experiment. The following summer a second copy of the PI-Neph (PI-Neph2) was built and deployed to the Studies of Emissions and Atmospheric Composition, Clouds and Climate Coupling by Regional Surveys (SEAC<sup>4</sup>RS) field campaign.

The OI-Neph underwent its first science flights during the last DISCOVER-AQ

deployment in Colorado during the summer of 2014. The P-3 aircraft sampled a variety of aerosols as well as performed dozens of spirals over six independent AERONET sites, as well as numerous ground stations over the course of this campaign. In addition to the OI-Neph measurements, PI-Neph2 was based at a ground site west of Denver while the original PI-Neph made measurements aboard the P-3. A preliminary calibration has been applied to the OI-Neph data from this experiment and examples of the resulting data products are shown in Figure 2.4 but PI-Neph data from the DC3 and SEAC<sup>4</sup>RS experiments will be the focus of the bulk of the analysis in the work.

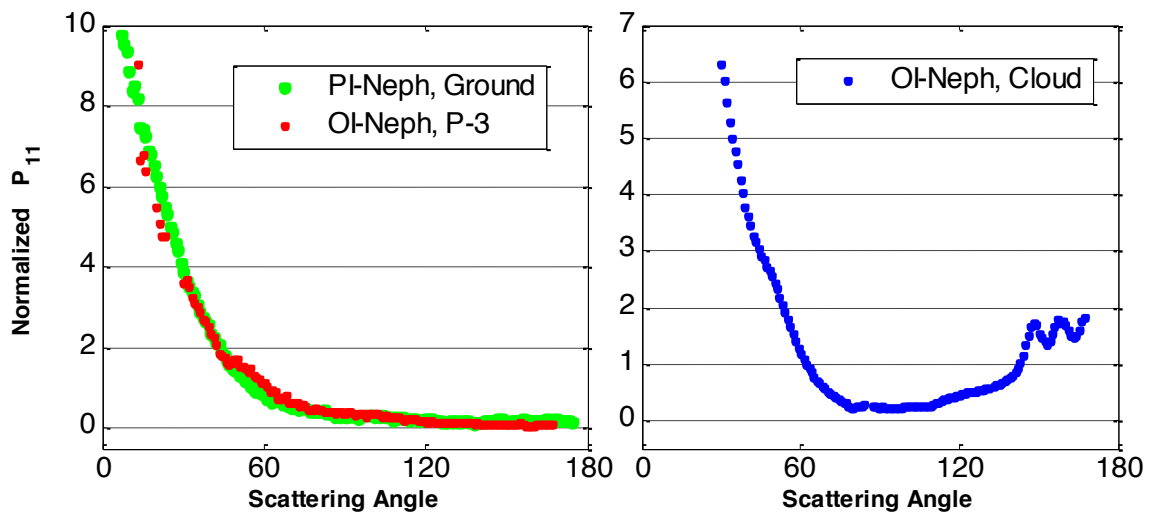


Figure 2.4: An intercomparison between the preliminary airborne OI-Neph product and corresponding ground based PI-Neph data (left) and the first liquid water cloud measurements made by the OI-Neph (right) are shown above. The angular range of the OI-Neph data products will significantly expand as the data reduction process is refined.

The DC3 field campaign took place over the central United States in May and June of 2012. The experiment was designed to shed new light on storm dynamics

and the effect of convective systems on the chemical composition of the troposphere [Barth et al., 2015]. Over the course of the experiment three aircraft flew dozens of flights with a combined payload of over sixty different instruments, providing remote sensing and in situ measurements of a wide range of trace gases, aerosols properties and meteorological parameters. The majority of flights focused on one of three study regions: northeastern Colorado (CO), northern Alabama (AL) and a region comprising northern Texas and southern Oklahoma (TX/OK) [Barth et al., 2015]. The NASA DC-8 aircraft was typically used to sample storm inflow, while the National Center for Atmospheric Research (NCAR) Gulfstream V (GV) and the German Deutsches Zentrum für Luft- und Raumfahrt (DLR) Falcon sampled the outflow regions. While the DC-8 did occasionally sample convective system outflow, PI-Neph data corresponding to these periods were infrequent and highly variable.

In August of 2013 the associated SEAC<sup>4</sup>RS campaign began its two-month long deployment, with flights covering much of the contiguous United States (CONUS). The campaign targeted a variety of atmospheric phenomena including the role of convection in the distribution of aerosols and gases within the troposphere, the climatic and meteorological effects of biomass burning and anthropogenic emissions and the calibration and validation of satellite data. The aircraft supporting the airborne portion of the experiment included the NASA ER-2, the NASA DC-8, and SPEC Inc. Learjet. These three platforms flew a total of 57 different flights and had a combined instrument payload very similar to DC3. A detailed description of the

SEAC<sup>4</sup>RS scientific goals, aircraft and instrumentation, as well as the corresponding implementation can be found in Toon et al. [2016].

The PI-Neph sampled from the DC-8 aircraft in both DC3 and SEAC<sup>4</sup>RS. In these experiments, ambient air was provided to the PI-Neph through the NASA Langley Aerosol Research Group Experiment's (LARGE) shrouded diffuser inlet [McNaughton et al., 2007], which sampled isokinetically. A flow of 20 liters per minute was maintained through the PI-Neph's 10-liter sample chamber, leading to an aerosol exchange time on the order of 30 seconds.

On the DC-8 the PI-Neph's sample was conditioned with a temperature controlled drier that heated the incoming ambient air to a temperature of 35°C and, in almost all cases, kept the relative humidity of the sample below 40%. When heating the sample aerosol, it is possible evaporate volatile compounds and significantly perturb the aerosol properties [Shingler et al., 2016], but this effect is not believed to have played a consequential role on PI-Neph measurements made during DC3 and SEAC<sup>4</sup>RS. To better understand the biases produced by the evaporation of volatile compounds PI-Neph total scattering measurements were compared with scattering data from an integrating nephelometer (model 3563, TSI Inc., St. Paul, MN, USA) using a nafion drier that did not require sample heating. A strong correlation was observed between the two instruments ( $R^2 > 0.995$ ) and no decrease in PI-Neph scattering, relative to integrating nephelometer scattering, was observed during periods corresponding to large temperature gradients between the PI-Neph's sample

chamber and the ambient air. It should be noted that the PI-Neph and integrating nephelometer sampled from the same inlet so the results of this comparison do not preclude effects from other heating mechanism like ram heating (adiabatic heating associated with decelerating flow) and heat exchange with the aircraft cabin inside the sample tubing [Wendisch et al., 2004; Baumgardner et al., 2011].

### **Laboratory Data**

The bulk of the laboratory measurements made by Imaging Nephelometers took place during Statistical Evaluation of Aerosol Retrieval (STEAR) experiment at the NASA Langley Research Center. STEAR strives to better understand the limitations of the AERONET aerosol retrieval algorithms by mimicking atmospheric extinction and radiance measurements in a laboratory context. The Cavity Attenuated Phase Shift (CAPS) instrument provided the extinction measurement while the PI-Neph provided angular scattering measurements that were analogous to AERONET radiances. To better mimic AERONET radiance measurements, the PI-Neph data is subsampled to correspond to AERONET almucantar scans with solar zenith angles ranging from 50 to 77 degrees. The aerosols sampled during this experiment include a wide array of artificially suspended dusts, salts, organics and volcanic ash samples.

Extensive PI-Neph sampling has also taken place inside the LACO laboratory at UMBC. The scattering patterns of several salts have been measured at a variety of relative humidities and the results of this experiment will be discussed further in

Chapter 3. In addition to the salt data, measurements were made on Volcanic Ash as well as ambient urban pollution and transported smoke that were collected by an inlet attached to the exterior of the building.

## 2.2 Basic Theory of Scattering Matrix Element Recovery

Imaging nephelometers generate a series of images in which the pixel counts in a given region of the image is determined by the scattering intensity at the corresponding scattering angle. Specifically, the Stokes vector incident on the camera is equal to,

$$I(\theta) \cdot \vec{S}^{out}(\Omega) = \frac{I_{in}\Delta V(\Omega)}{4\pi R(\Omega)^2} \mathbf{F}(\Omega) \cdot \vec{S}^{in} \quad (2.1)$$

where  $\Delta V(\Omega)$  is the scattering volume corresponding to a given angle  $\Omega$ ,  $R(\Omega)$  is the distance from the camera to that scattering volume,  $\vec{S}^{in}$  is the normalized Stokes vector of the incoming laser light in the scattering plane coordinate system and  $I_{in}$  is the input laser intensity which is assumed to be constant in both images. The narrow width of the laser beam means that the variation in zenith scattering angle across a single pixel wide cross section perpendicular to the beam is much less than a degree. This fact, along with the assumption of a macroscopically isotropic and symmetric medium (which implies azimuthally independent angular scattering), means that the integral of the counts in a line perpendicular to the beam is proportional to the total scattered signal  $I(\theta)$  (see Figure 2.5).

All currently existing imaging nephelometers use a detection system that is

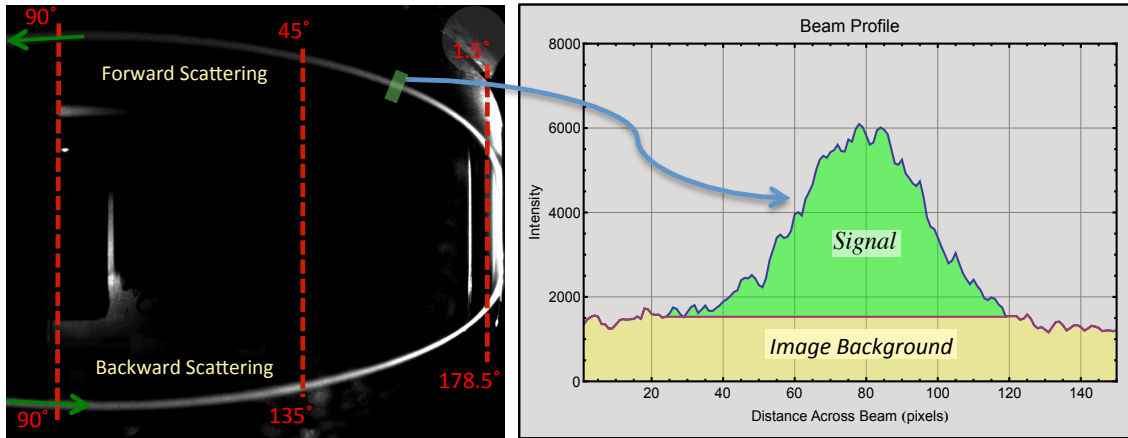


Figure 2.5: An image taken by the CCD of an imaging nephelometer (left) and an example of a perpendicular beam profile showing the signal and background (right). The area of the region labeled signal is proportional to the scattering intensity at the scattering angle corresponding to the green box on the left panel.

assumed to be insensitive to polarization so only  $I(\theta)$  can be measured. This constraint, along with the assumption of a macroscopically isotropic and mirror-symmetric medium, means that only the first two  $F_{11}$  and  $F_{12}$  elements of the scattering matrix influence the image counts. If two images are taken, with the proper two different input Stokes vectors  $\vec{S}_1^{in}$  and  $\vec{S}_2^{in}$ , these two elements can both be recovered from the image profiles.

It can be shown that the two input Stokes vectors provide the most sensitivity to the first two scattering elements when they take the forms,

$$\vec{S}_1^{in} = \begin{pmatrix} 1 \\ -1 \\ 0 \\ 0 \end{pmatrix} \quad \text{and} \quad \vec{S}_2^{in} = \begin{pmatrix} 1 \\ 1 \\ 0 \\ 0 \end{pmatrix}. \quad (2.2)$$

Intuitively, these two inputs correspond to 100% linearly polarized light that is parallel and perpendicular to the scattering plane, respectively. According to equation Equation 2.1 these inputs should produce images with the intensities given by

$$I_1(\theta) = \frac{I_{in}\Delta V(\theta)}{4\pi R(\theta)^2}(F_{11}(\theta) - F_{12}(\theta)) \quad (2.3)$$

and

$$I_2(\theta) = \frac{I_{in}\Delta V(\theta)}{4\pi R(\theta)^2}(F_{11}(\theta) + F_{12}(\theta)). \quad (2.4)$$

The leading factor of Equations 2.3 and 2.4 is independent of the sampled aerosol and can be combined into a single calibration constant:

$$m(\theta) = \frac{I_{in}\Delta V(\theta)}{4\pi R(\theta)^2}. \quad (2.5)$$

Equations 2.3 and 2.4 then yield the following equations:

$$F_{11}(\theta) = \frac{I_1(\theta) + I_2(\theta)}{2m(\theta)} \quad (2.6)$$

$$F_{12}(\theta) = \frac{I_2(\theta) - I_1(\theta)}{2m(\theta)}. \quad (2.7)$$

Therefore, in the ideal case the sum of the dark subtracted image counts is proportional to  $F_{11}$  and the difference of the image counts is proportional to  $F_{12}$ .

In addition to measurements of absolute and polarized phase functions ( $F_{11}$

and  $F_{12}$ ) derived scattering coefficients and asymmetry parameters are frequently reported with the PI-Neph data. These products are obtained by integrating the  $F_{11}$  data from  $0^\circ$  to  $180^\circ$ , with nearest neighbor extrapolation used to estimate the values extending beyond the measured angles. The scattering coefficient is calculated with Equation 1.3 and the asymmetry parameter is computed with the equation

$$g = 2\pi \int_0^\pi F_{11}(\theta) \cos(\theta) d\theta. \quad (2.8)$$

### 2.3 Instrument Calibration

The characterization of an Imaging Nephelometer requires mapping of the angular and polarization state of the system as well as quantifying the imager's radiometric sensitivity relative to the input laser beam's power. The angular calibration is the most intensive part of this characterization procedure and is performed in several stages. The first of these stages maps each CCD pixel to a given two-dimensional viewing angle. This mapping is achieved by imaging two large, flat regularly spaced grids of squares that are orthogonal to the camera's optical axis and separated by a fixed distance  $d$ . The imaged squares can then be counted to obtain the horizontal  $l$  and vertical  $h$  distances between the center of the grid (as defined by the camera's optical axis) and a given pixel. The horizontal view angle  $\alpha$  and vertical view angle

$\delta$  can then be calculated by the formulas,

$$\alpha = \tan^{-1}\left(\frac{l_2 - l_1}{d}\right) \quad (2.9)$$

$$\delta = \tan^{-1}\left(\frac{h_2 - h_1}{(l_2 - l_1)^2 + d^2}\right) \quad (2.10)$$

where the subscripts 1 and 2 indicate the first and second grids respectively.

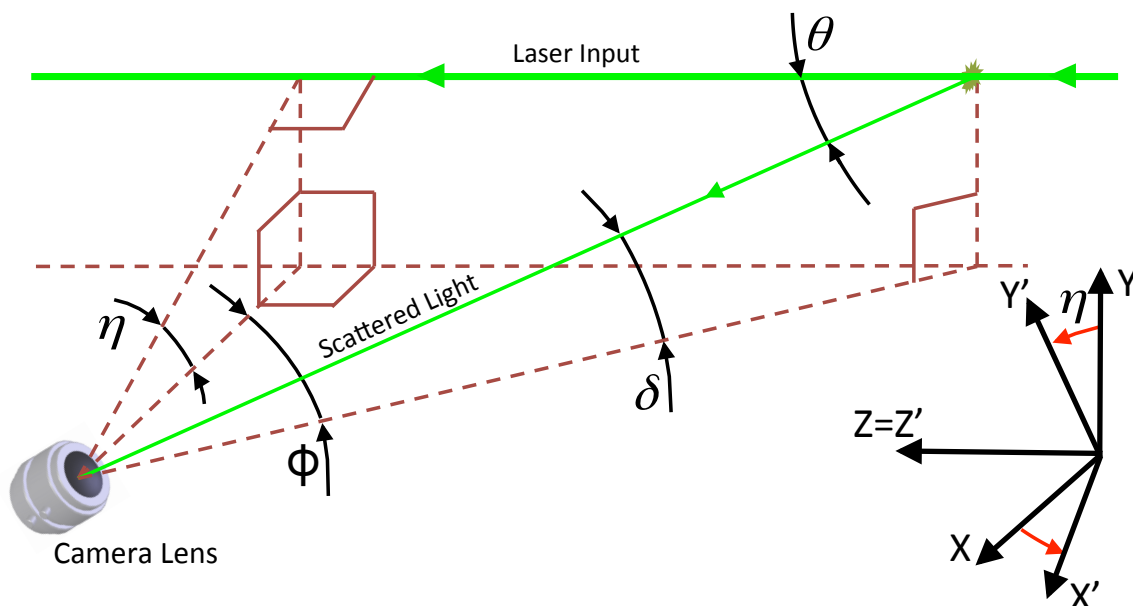


Figure 2.6: The input laser, scattered light and camera lens geometry of the forward beam of an Imaging Nephelometer. The un-primed axes denote the calibration coordinate system while the primed axes show the scattering coordinate system in which the y-axis is orthogonal to the scattering plane.

The grid based calibration procedure requires that  $\alpha$  be measured with the camera removed from the system so the horizontal view angle of the camera relative to the inside of the instrument must be further constrained by a triangulation procedure. This process finds the angle  $\phi$  (see Figure 2.6) at the low and high scattering angles

from measurements of the legs of the right triangle made up by the viewing direction and sides of the instrument body.  $\phi$  is then determined at all scattering angles by stitching  $\alpha$  to the values of  $\phi$  found at the extreme angles during triangulation. The triangulation process is only applied to the  $\alpha$  angle because there is significantly less uncertainty in the camera's mounting position along the  $\delta$  direction.

The three-dimensional zenith scattering angle  $\theta$  and the orientation of the scattering plane (relative to the instrument body)  $\eta$  can then be computed from  $\phi$  and  $\delta$  by the equations,

$$\theta = \cos^{-1}(\sin \phi \cos \delta) \quad (2.11)$$

$$\eta = \tan^{-1}(\tan \delta \cos \phi). \quad (2.12)$$

The camera's entrance pupil moves slightly for different view angles so  $\eta$  is not constant and can be expressed as a function of  $\theta$ .

The exact polarization state of the laser is established using a Thorlabs, PAX series polarimeter mounted to the body of the instrument.  $\eta$  then represents the coordinate system rotation, about the laser propagation direction, required to transform the polarimeter Stokes vector measurement to the coordinate system defined by the scattering plane. The input Stokes vector in the scattering plane is then given by

$$\overrightarrow{S^{in}(\theta)} = \mathbf{L}(\eta(\theta)) \cdot \overrightarrow{S^{pol}} \quad (2.13)$$

where  $\overrightarrow{S^{pol}}$  represents the Stokes vector measured by the Thorlabs polarimeter and  $\mathbf{L}$

is the rotation transformation matrix

$$\mathbf{L}(\eta) = \begin{pmatrix} 1 & 0 & 0 & 0 \\ 0 & \cos(2\eta) & \sin(2\eta) & 0 \\ 0 & -\sin(2\eta) & \cos(2\eta) & 0 \\ 0 & 0 & 0 & 1 \end{pmatrix}. \quad (2.14)$$

Note that since  $\eta$  is dependent on the camera's view angle,  $\overrightarrow{S^{in}}$  takes on a  $\theta$  dependence (this dependence was omitted from Section 2.2 for simplicity). As  $\overrightarrow{S^{in}(\theta)}$  changes with scattering angle, no single liquid crystal retardance setting can produce the optimal polarization states (described by Equation 2.2) across the entire length of the laser beam. The final laser polarization states are chosen to minimize the sum of the differences between the true and ideal Stokes vectors over the entire length of the beam.

The radiometric calibration has traditionally been performed using gases with known scattering coefficients and angular scattering functions. The gases used are generally pure air, carbon dioxide and occasionally helium. The large range in scattering coefficients found in these gases permits a linear fit of the theoretical signal to the number of CCD counts detected. The y-intercept of this fit provides an estimate of the signal obtained in the case of zero scattering. Any non-zero values found in this intercept are generally the product of laser stray light and are subtracted from the images during the data processing procedure (see Section 2.4 for details).

## 2.4 Detailed Mathematical Model

The following section provides a very detailed mathematical model of the PI-Neph including many sources of well-known error. The casual reader may skip this section and the following Section 2.5 with no loss of continuity.

### 2.4.1 Fundamental Assumptions and Equations

Section 2.2 provided a simple, intuitive model of the Imaging Nephelometer measurement under ideal conditions. In practice, these conditions are rarely achieved and several corrections must be applied, significantly complicating the recovery of  $F_{11}$  and  $F_{12}$ . The complications present in all current Imaging Nephelometer implementations include:

- Laser stray light incident on the instrument body can bias the image counts, typically over angular ranges of several degrees.
- As a results of this laser beam folding, as well as the scattering plane rotation described by  $\eta(\theta)$ , the ideal polarization states of Equation 2.2 cannot be achieved at all angles.
- The beam folding can produce a calibration drift that is only present in the backward beam’s signal. This artifact results from contamination of the folding mirror as well as small shifts in the corresponding collimating optics and is frequently referred to as the backward beam “cut factor”.

- In early I-Neph implementations, the output power of the laser source varied significantly and small changes in instrument alignment were found to significantly influence the reference detector's ability to accurately sample the laser. These power variations were found to occur on relatively short time scales, with significant changes occurring within the span of the two images that compose a single measurement.
- The aerosol is always suspended in air and this scattering contribution must be subtracted to obtain the aerosol only signal.
- The final products are reported at standard temperature and pressure (STP) but the measurements themselves are made at a variety of temperatures and pressures.

In this subsection, a mathematical model of the instrument that takes these complications into account is developed. This is the model that is implemented in the Matlab based data reduction software INephMatlab ([https://bitbucket.org/umbc\\_ineph/ineph\\_matlab/](https://bitbucket.org/umbc_ineph/ineph_matlab/)).

The input normalized Stokes vector will take the form

$$\vec{S}_{n,k}^{in}(\theta) = \begin{pmatrix} 1 \\ q_{n,k}^{in}(\theta) \\ u_{n,k}^{in}(\theta) \\ v_{n,k}^{in} \end{pmatrix} \quad (2.15)$$

were the first subscript  $n$  represents the number of the image in the pair (1 or 2) and the second subscript  $k$  represents the forward (f) or backward (b) beams. In this model,  $\overrightarrow{S_{n,k}^{in}}$  is a function of theta because the input vectors are assumed to have already been transformed to the scattering plane coordinate system. There is no  $\theta$  dependence in  $v_{n,k}^{in}$  because the rotation matrix  $\mathbf{L}$  does not alter the value of this component.

We start by combining Equation 2.5 and Equation 2.1 as well as adding  $n, k$  and time dependences to the relevant variables to obtain

$$I_{n,k}(\theta, t) \cdot \overrightarrow{S_{n,k}^{out}}(\theta, t) = m_{n,k}(\theta) \cdot \mathbf{X}(\theta, t) \cdot \overrightarrow{S_{n,k}^{in}}(\theta) \quad (2.16)$$

where the matrix  $\mathbf{X}$  is the sum of the aerosol scattering matrix at ambient temperature and pressure  $\mathbf{F}_{amb}$  and the Rayleigh scattering matrix  $\mathbf{R}_{air}$  of the surrounding gases. Note that at this stage the elements of  $\mathbf{X}$  represent the scattering at the measurement temperature and pressure. The  $n$  and  $k$  subscripts are omitted from  $\mathbf{X}$  as its elements are assumed to be constant across both beams during the acquisition of both images. We then add a calibration offset  $r_{n,k}(\theta)$  as well as another product  $\Gamma_n(t)$  corresponding to some change in the output power of the laser. Additionally, we will add a variable  $\chi(t)$  representing the cut factor that only effects the scattering signal from the backward beam.  $\chi$  is expected to vary relatively slowly so we assume that there is no change in its value over the course of an adjacent pair of images (i.e.  $\chi_1 = \chi_2 = \chi$ ) but we do allow it to vary as a function of  $t$  (i.e from one complete

measurement to the next). The resulting equations for the measured signal in the forward and backward scattering angles are

$$I_{n,f}(\theta, t) \cdot \overrightarrow{S_{n,f}^{out,t}}(\theta) = \Gamma_n(t) (m_{n,f}(\theta) \cdot \mathbf{X}(\theta, t) \cdot \overrightarrow{S_{n,f}^{in}}(\theta) + r_{n,f}(\theta)) \quad (2.17)$$

and

$$I_{n,b}(\theta, t) \cdot \overrightarrow{S_{n,b}^{out,t}}(\theta) = \Gamma_n(t) \chi(t) (m_{n,b}(\theta) \cdot \mathbf{X}(\theta, t) \cdot \overrightarrow{S_{n,b}^{in}}(\theta) + r_{n,b}(\theta)). \quad (2.18)$$

Equations 2.17 and 2.18 can then be broken down into 16 separate equations: two for each pair of pictures ( $n = 1, 2$ ), each with four Stokes components and each of those with two beams ( $k = f, b$ ). We assume that the lens and CCD are insensitive to polarization and that our measurement is directly proportional to total radiance (i.e. the detector's response is linear) so the number of relevant relationships is reduced to four equations (two forward and two backward):

$$I_{n,f}(\theta, t) = \Gamma_n(t) \left( m_{n,f}(\theta) (X_{11}(\theta, t) + q_{n,f}(\theta) X_{12}(\theta, t)) + r_{n,f}(\theta) \right) \quad (2.19)$$

and

$$I_{n,b}(\theta, t) = \Gamma_n(t) \chi(t) \left( m_{n,b}(\theta) (X_{11}(\theta, t) + q_{n,b}(\theta) X_{12}(\theta, t)) + r_{n,b}(\theta) \right). \quad (2.20)$$

This model assumes that the intensity measured by the camera's CCD  $I_{n,f}$  is

an unbiased measure of the total radiance incident on the camera lens. In practice, the actual readout of the camera will contain some small bias produced by components of the imaging system that are sensitive to polarization. Attempts to characterize the polarization sensitivity of the PI-Neph's camera have put upper bounds on the absolute values of the 2<sup>nd</sup>, 3<sup>rd</sup> and 4<sup>th</sup> elements of the first row of the Muller matrix at around 0.02. While this result suggests that these values may be quite low, polarization effects could still bias the recovered scattering matrix elements by up to a few percent, especially at the upper ends of these bounds. Regardless, these effects are not modeled here because the camera's Muller matrix elements must be measured with a technique that has error significantly less than the values of the elements themselves before any meaningful correction can be applied. Additionally, a perfect correction for polarization artifacts cannot be achieved, even given a perfectly characterized Muller matrix, without complete a priori knowledge of all scattering matrix elements, including the elements we are trying to measure. Therefore, a key design characteristic of future Imaging Nephelometers should be to include an imaging system with minimal sensitivity to polarization. This design goal was incorporated into the OI-Neph's optical system, which contains several features chosen to minimize the influence of polarization artifacts, including a special polarization insensitive coating applied to the cylindrical mirror at the foot of the pylon as well as a narrow field of view in the refractive portion of the lens.

### 2.4.2 Calculation of Calibration Constants

The results of the angular calibration procedure and the polarimeter measurements can be combined with Equation 2.13 to obtain  $q_{n,k}(\theta)$ . The process for determining the calibration “slopes” and “offsets” ( $m_{n,b}$  and  $r_{n,b}$ ) is less straight forward due to laser power variations during gas calibration measurements of pure air and CO<sub>2</sub>. In order to use the two calibration gases to determine the instrument’s linear response ( $m_{n,b}$ ) and a stray light driven offset ( $r_{n,b}$ ) the laser power variations represented by  $\Gamma$  and  $\chi$  must first be well characterized.

The value of  $\Gamma_n$  simply needs to capture the  $\theta$  independent, time-dependent *change* in laser power so its initial value is arbitrary (the values of  $m_{n,b}$  and  $r_{n,b}$  will just scale accordingly). We will therefore define  $\Gamma_n(t_{air}) = 1$ , where  $t_{air}$  represents the measurement period corresponding to pure air. Similarly, we will define the cut factor such that  $\chi(t_{air}) = 1$  as well as assume that  $\chi(t_{CO_2}) = 1$ , where  $t_{CO_2}$  represents the measurement period corresponding to CO<sub>2</sub>. The last assumption is expected to be relatively conservative as 1) the instrument is generally stationary between the air and CO<sub>2</sub> calibrations so changes to the alignment of the collimating optics are minimal and 2) the pure gases used in the calibration do not result in any deposits on the beam folding mirrors. The only remaining two unknowns, given the above assumptions, are the changes in laser power between the air and CO<sub>2</sub> calibrations  $\Gamma_n(t_{CO_2})$  for the first and second images in the measurement pair.

We next define an error free simulated Rayleigh scattering signal that is known

for each calibration gas

$$Z_{n,b}^{gas}(\theta) = R_{11}^{gas}(\theta) + q_{n,f}(\theta)R_{12}^{gas} \quad (2.21)$$

where gas can be air or CO<sub>2</sub>. The Rayleigh scattering matrix elements of this equation have the form

$$R_{11}^{gas}(\theta) = \beta_{sca}^{gas} \left( \frac{3}{4} \omega_{gas} (1 + \cos(\theta))^2 + (1 - \omega_{gas}) \right) \quad (2.22)$$

and

$$R_{12}^{gas}(\theta) = -\frac{3}{4} \beta_{sca}^{gas} \omega_{gas} \sin(\theta)^2 \quad (2.23)$$

where

$$\omega_{gas} = \frac{1 - d_{gas}}{1 + d_{gas}/2}. \quad (2.24)$$

The variable  $d_{gas}$  represents the depolarization correction of the gas in question and  $\beta_{sca}^{gas}$  represents the corresponding scattering coefficient [Hansen and Travis, 1974]. Note that the scattering coefficient is a function of the gases' temperature and pressure and therefore must be adjusted to match the conditions of the calibration.

The assumption  $\chi(t_{gas}) = 1$  can then be combined with Equations 2.19, 2.20 and 2.21 to obtain the equation

$$\frac{I_{n,k}(\theta, t_{gas})}{\Gamma_n(t_{gas})} = m_{n,k}(\theta) \cdot Z_{n,k}^{gas}(\theta) + r_{n,k}(\theta). \quad (2.25)$$

To estimate the value of  $\Gamma_n(t_{CO_2})$  we will use the fact that the stray light is only expected to meaningfully contribute at a minority of scattering angles. We will define a subset of angles  $\theta_{n,k}^{clean}$  where the contribution from the stray light background is negligible. We can estimate the members of  $\theta_{n,k}^{clean}$  by initially assuming  $\Gamma_n(t_{CO_2})$  is unity and then finding preliminary solutions for  $m_{n,b}$  and  $r_{n,b}$  using measurements from both gases and Equation 2.25. The lowest 50% of the resulting  $r_{n,b}(\theta)$  values, after a low frequency filter has been applied to remove long term biases produced by laser power drift, should correspond to relatively stray light free regions of the image and will define the members of  $\theta_{n,k}^{clean}$ . We will then assume, for the purposes of estimating  $\Gamma_n(t_{CO_2})$ , that there is no stray light in these “clean” regions (i.e.  $r_{n,k}(\theta_{n,k}^{clean}) = 0$ ). This removes an unknown in the case of both images ( $n = 1, 2$ ) at the angles composing  $\theta_{n,k}^{clean}$  and will allow us to find the  $\theta$  independent variable  $\Gamma_n(t_{CO_2})$ .

The assumptions  $\Gamma_n(t_{air}) = 1$  and  $r_{n,k}(\theta_{n,k}^{clean}) = 0$  can then be incorporated into Equation 2.25 and equation of for the pure air calibration

$$I_{n,k}(\theta_{n,k}^{clean}, t_{air}) = m_{n,k}(\theta_{n,k}^{clean}) \cdot Z_{n,k}^{air}(\theta_{n,k}^{clean}) \quad (2.26)$$

as well as the CO<sub>2</sub> calibration

$$\frac{I_{n,k}(\theta_{n,k}^{clean}, t_{CO_2})}{\Gamma_n(t_{CO_2})} = m_{n,k}(\theta_{n,k}^{clean}) \cdot Z_{n,k}^{CO_2}(\theta_{n,k}^{clean}). \quad (2.27)$$

Dividing Equation 2.26 by Equation 2.27 and rearranging produces an equation for

the unknown  $\Gamma_n(t_{CO_2})$  in terms of known quantities

$$\Gamma_n(t_{CO_2}) = \frac{I_{n,k}(\theta_{n,k}^{clean}, t_{CO_2}) \cdot Z_{n,k}^{air}(\theta_{n,k}^{clean})}{I_{n,k}(\theta_{n,k}^{clean}, t_{air}) \cdot Z_{n,k}^{CO_2}(\theta_{n,k}^{clean})}. \quad (2.28)$$

As there are many valid values of  $\theta_{n,k}^{clean}$  in practice (50% of the number of measurement angles) the value  $\Gamma_n(t_{CO_2})$  is generally calculated many times, with the final value being determined by a signal weighted average of the individual values.

After  $\Gamma_n(t_{CO_2})$  is known Equation 2.25 can be used to solve for  $m_{n,k}(\theta)$  and  $r_{n,k}(\theta)$ . The value of  $Z_{2,k}^{gas}(\theta)$  (with  $q_2 \approx 1$ ) is very low except when  $\theta$  is very close to  $0^\circ$  and  $180^\circ$ . In order to avoid sensitivity issues resulting from this weak signal the measured values of  $m_{2,k}(\theta)$  are often replaced according to the formula  $m_{2,k}(\theta) = C_k m_{1,k}(\theta)$ . The values of  $C_k$  are determined using the original measured values of  $m_{2,k}(\theta)$  at the low ( $k = f$ ) or high ( $k = b$ ) scattering angles, where the Rayleigh scattering signal is strong in both polarizations. This scaling constant  $C_k$  is required because the optics prior to the sample volume have some polarization dependence in their transmission. In the PI-Neph  $C_k$  generally differs from unity by about 25%.

### 2.4.3 Simplifying Assumptions

Measurements of  $I_{n,k}(\theta, t)$  are available for all  $n$  and  $k$  in the region where the forward and backward beams have overlapping scattering angles ( $\theta \approx 90^\circ$ ) so the calculation of  $\theta$  independent quantities can make use of all four equation simultaneously. Unfortunately, once all calibration parameters have been calculated, the four equations

representing the aerosol measurement (Equations 2.19 and 2.20) still contain five unknowns ( $\Gamma_1$ ,  $\Gamma_2$ ,  $\chi$ ,  $X_{11}$  and  $X_{12}$ ) and therefore still lack sufficient information to calculate all parameters. Two methods for dealing with this issue are presented in this section, one incorporating an additional piece of information from a separate integrating nephelometer and the other sacrificing accuracy in the derived  $\beta_sca$  in exchange for a more accurate recovery of the phase function shape.

These two methods are more easily understood when  $\Gamma_n(t)$  is written as two new variables  $\xi(t) = \Gamma_1(t)$  and  $G(t) = \Gamma_2(t)/\xi(t)$ . Intuitively,  $\xi(t)$  represents the change in laser power in the first image at time  $t$  relative to the laser power during the first image of the pure air Rayleigh calibration.  $G(t)$  is then the change in the ratio of laser powers between the first and second images in the pure air calibration and the corresponding ratio in the measurement at time  $t$ . The deviations of  $\xi$  and  $G$  from unity are generally less than 30% but can occasionally differ from one by a factor of two, especially in the PI-Neph's 473nm channel. If we replace  $\Gamma$  in Equations 2.19 and 2.20 with these new variables we obtain four new equations:

$$I_{1,f}(\theta, t) = \xi(t) \cdot m_{1,f}(\theta) (X_{11}(\theta, t) + q_{1,f}(\theta) X_{12}(\theta, t)) + \xi(t) \cdot r_{1,f}(\theta) \quad (2.29)$$

$$I_{1,b}(\theta, t) = \chi(t) \left( \xi(t) \cdot m_{1,b}(\theta) (X_{11}(\theta, t) + q_{1,b}(\theta) X_{12}(\theta, t)) + \xi(t) \cdot r_{1,b}(\theta) \right) \quad (2.30)$$

$$I_{2,f}(\theta, t) = G(t) \left( \xi(t) \cdot m_{2,f}(\theta) (X_{11}(\theta, t) + q_{2,f}(\theta) X_{12}(\theta, t)) + \xi(t) \cdot r_{2,f}(\theta) \right) \quad (2.31)$$

$$I_{2,b}(\theta, t) = G(t) \cdot \chi(t) \left( \xi(t) \cdot m_{2,b}(\theta) (X_{11}(\theta, t) + q_{2,b}(\theta) X_{12}(\theta, t)) + \xi(t) \cdot r_{2,b}(\theta) \right). \quad (2.32)$$

We will next remove all explicit references to  $\xi$  in the above equations. The substitution of in a new variable  $X'_{i,j}(\theta, t) = \xi(t) \cdot X_{i,j}(\theta, t)$  achieves this goal in among the first of the two terms in each of these equations. As the deviation of  $\xi$  from unity is generally less than 30% and  $r_{n,k}(\theta)$  rarely exceeds  $3 Mm^{-1}sr^{-1}$  the approximation  $\xi \cdot r_{n,k}(\theta) \approx r_{n,k}(\theta)$  should produce less than a single  $Mm^{-1}sr^{-1}$  of error. Applying this assumption and substitution leads to following four equations that can be used to calculate  $G$ ,  $\chi$ ,  $X'_{11}$  and  $X'_{12}$ :

$$I_{1,f}(\theta, t) = m_{1,f}(\theta)(X'_{11}(\theta, t) + q_{1,f}(\theta)X'_{12}(\theta, t)) + r_{1,f}(\theta) \quad (2.33)$$

$$I_{1,b}(\theta, t) = \chi(t) \left( m_{1,b}(\theta)(X'_{11}(\theta, t) + q_{1,b}(\theta)X'_{12}(\theta, t)) + r_{1,b}(\theta) \right) \quad (2.34)$$

$$I_{2,f}(\theta, t) = G(t) \left( m_{2,f}(\theta)(X'_{11}(\theta, t) + q_{2,f}(\theta)X'_{12}(\theta, t)) + r_{2,f}(\theta) \right) \quad (2.35)$$

$$I_{2,b}(\theta, t) = G(t) \cdot \chi(t) \left( m_{2,b}(\theta)(X'_{11}(\theta, t) + q_{2,b}(\theta)X'_{12}(\theta, t)) + r_{2,b}(\theta) \right). \quad (2.36)$$

#### 2.4.4 Finding Scattering Matrix Elements

Explicit analytic solutions for all of the unknowns in Equations 2.33-2.36 are not obvious. The variable  $\chi$  can relatively easily be isolated in the form shown in Equation 2.37 at which point its value can be determined numerically. It is then relatively easy to derive Equation 2.38, which gives  $G(t)$  as a function of only  $\chi(t)$  and knowns. In both equations, the dependent variables have been dropped for brevity. Note we will frequently recover multiple values of  $G(t)$  and  $\chi(t)$  as there are generally several

overlapping angles for which  $I_{n,k}(\theta, t)$  is available for all  $n$  and  $k$ . As we did with  $\Gamma(t_{CO_2})$  in the Rayleigh calibration, we apply an averaging procedure where the values at each angle are weighted by the total measured signal  $I_{n,k}$  at that angle.

$$I_{2,b} = \frac{\chi I_{2,f} (\chi m_{1,b} m_{2,b} (q_{1,b} - q_{2,b}) (r_{1,f} - I_{1,f}) + m_{1,f} (m_{2,b} (q_{1,f} - q_{2,b}) (I_{1,b} - \chi r_{1,b}) + \chi m_{1,b} r_{2,b} (q_{1,f} - q_{1,b})))}{\chi m_{1,b} m_{2,f} (q_{1,b} - q_{2,f}) (r_{1,f} - I_{1,f}) + m_{1,f} (m_{2,f} (q_{1,f} - q_{2,f}) (I_{1,b} - \chi r_{1,b}) + \chi m_{1,b} r_{2,f} (q_{1,f} - q_{1,b}))} \quad (2.37)$$

$$G = \frac{\chi m_{1,b} I_{2,f} m_{1,f} (q_{1,f} - q_{1,b})}{\chi m_{1,b} m_{2,f} (q_{1,b} - q_{2,f}) (r_{1,f} - I_{1,f}) + m_{1,f} (m_{2,f} (q_{1,f} - q_{2,f}) (I_{1,b} - \chi r_{1,b}) + \chi m_{1,b} r_{2,f} (q_{1,f} - q_{1,b}))} \quad (2.38)$$

Once the values of  $G$  and  $\chi$  are obtained we can proceed to calculate the product of  $\xi$  and the ambient total scattering matrix elements for both the forward and backward beams  $X_{ij}^{fwd(back)}$ . Equations 2.33 and 2.35 can be used to derive expressions for  $X_{11}^{fwd}$  and  $X_{12}^{fwd}$  that are free from the  $I_{n,b}$  measurements that do not cover the bulk of the forward scattering angles:

$$X_{11}^{fwd} = -\frac{I_{1,f} m_{2,f} q_{2,f} + m_{1,f} q_{1,f} r_{2,f} - m_{2,f} q_{2,f} r_{1,f} - (I_{2,f} m_{1,f} q_{1,f})/G}{m_{1,f} m_{2,f} q_{1,f} - m_{1,f} m_{2,f} q_{2,f}} \quad (2.39)$$

$$X_{12}^{fwd} = \frac{I_{1,f} m_{2,f} + m_{1,f} r_{2,f} - m_{2,f} r_{1,f} - (I_{2,f} m_{1,f})/G}{m_{1,f} m_{2,f} q_{1,f} - m_{1,f} m_{2,f} q_{2,f}}. \quad (2.40)$$

Correspondingly, Equations 2.34 and 2.36 can be used to derive expressions for the backward signal that are free from the  $I_{n,f}$  measurements:

$$X_{11}^{back} = \frac{(I_{2,b} m_{1,b} q_{1,b})/G - I_{1,b} m_{2,b} q_{2,b} - \chi m_{1,b} q_{1,b} r_{2,b} + \chi m_{2,b} q_{2,b} r_{1,b}}{\chi m_{1,b} m_{2,b} q_{1,b} - \chi m_{1,b} m_{2,b} q_{2,b}} \quad (2.41)$$

$$X_{12}^{back} = \frac{(-I_{2,b} m_{1,b})/G + I_{1,b} m_{2,b} + \chi m_{1,b} r_{2,b} - \chi m_{2,b} r_{1,b}}{\chi m_{1,b} m_{2,b} q_{1,b} - \chi m_{1,b} m_{2,b} q_{2,b}}. \quad (2.42)$$

$X_{ij}^{fwd}$  and  $X_{ij}^{back}$  can then be stitched together to obtain values of  $X'_{ij}$  that cover the entire range of sampled scattering angles. An average is used at the overlapping regions, where values of both  $X_{ij}^{fwd}$  and  $X_{ij}^{back}$  exist.

#### 2.4.5 Integrating Nephelometer $\xi$ Correction

The Imaging Nephelometer data products as well as typical integrating nephelometer products are reported at standard temperature and pressure. The conversion of

scattering matrix elements can be accomplished with the equation

$$Xstp'_{ij}(\theta, t) = X'_{ij}(\theta, t) \frac{T(t)}{T_{STP}} \frac{P_{STP}}{P(t)} \quad (2.43)$$

where  $T(t)$  and  $P(t)$  are the respective measurement temperature and pressures,  $T_{STP}$  is 273.15°C and  $P_{STP}$  is equal to 101.3 kPa.

If integrating nephelometer measurements are made in parallel to the Imaging Nephelometer they can be used to determine the I-Neph laser's power output over the course of a measurement (i.e. the value of  $\xi$ ). This correction is best accomplished using the raw integrating nephelometer measurement, before corrections for truncation and non-idealities in the weighting function, that is given by

$$\zeta_{sca}(t) = \frac{1}{2} \int_0^\pi F_{11}(\theta, t) \cdot w(\theta) d\theta \quad (2.44)$$

where  $w(\theta)$  is the weighting function of the nephelometer in question. A comprehensive parameterization of the weighting functions of two common integrating nephelometers can be found in Müller et al. [2011]. Note that the truncation of the extreme angles, often 0°-7° and 170°-180°, is included in the weighting function  $w(\theta)$ . In principle, truncation corrected (ex. Anderson and Ogren [1998]) integrating nephelometer measurements of the scattering coefficient  $\beta_{sca}$  could also be used but differences in the truncation correction between the integrating and imaging nephelometers would introduce additional errors.

The integrating nephelometer measurement  $\zeta_{sca}$  only represents the aerosol signal but  $Xstp'_{ij}$  contains both the aerosol and Rayleigh components of the signal. If we integrate the aerosol and Rayleigh components of  $Xstp'_{ij}$  separately over theta

with the  $w(\theta)$  kernel we obtain

$$\int_0^\pi Xstp'_{11}(\theta, t) \cdot w(\theta) d\theta = \xi(t) \int_0^\pi F_{11}(\theta, t) \cdot w(\theta) d\theta + \xi(t) \int_0^\pi R_{11}(\theta) \cdot w(\theta) d\theta. \quad (2.45)$$

We can then see from Equation 2.44 that the first term on the right-hand side of Equation 2.45 is the product  $2\xi \cdot \zeta_{sca}$ . Substituting in  $\zeta_{sca}$  and then rearranging gives us an explicit formula for  $\xi$  in terms of known quantities

$$\xi(t) = \frac{\int_0^\pi Xstp'_{11}(\theta, t) \cdot w(\theta) d\theta}{2\zeta_{sca}(t) + \int_0^\pi R_{11}(\theta) \cdot w(\theta) d\theta}. \quad (2.46)$$

The  $\xi$  corrected, STP adjusted scattering matrix elements are then given by  $Xstp_{ij} = Xstp'_{ij}/\xi$ .

If integrating nephelometer data is not available, or the stability of the integrating nephelometer is believed to be inferior to the imaging nephelometer, this correction can simply be skipped. In this case  $\xi$  will be assumed to equal unity and  $Xstp_{ij} = Xstp'_{ij}$ .

#### 2.4.6 Final Rayleigh Subtracted Aerosol Products

The primary (level 1) products produced by Imaging Nephelometers are aerosol only (Rayleigh signal subtracted)  $F_{ij}(\theta, t)$ ,  $\beta_{sca}(t)$  and the asymmetry parameter  $g(t)$  at STP. Once  $Xstp_{ij}$  is obtained the final scattering matrix elements can be obtained by simply subtracting the Rayleigh contribution

$$F_{ij}(\theta, t) = Xstp_{ij}(\theta, t) - R_{ij}(\theta). \quad (2.47)$$

The scattering coefficient and asymmetry parameter are both produced from integrals of  $F_{11}$  over all scattering angles ( $0^\circ$  to  $180^\circ$ ). An assumption about the shape of  $F_{11}$  must be made at the extreme angles as Imaging Nephelometer's only sample a subset of these angles ranging from  $\theta_{min}$  to  $\theta_{max}$ . Historically the nearest neighbor approximation has been used to estimate the values at the extreme angles. Under this assumption the scattering coefficient can be calculated by

$$\beta_{sca}(t) = \frac{1}{2} \int_0^\pi F_{11}^{all}(\theta, t) \cdot \sin(\theta) d\theta \quad (2.48)$$

where

$$F_{11}^{all}(\theta, t) = \begin{cases} F_{11}(\theta_{min}) & \text{if } 0 \leq \theta < \theta_{min} \\ F_{11}(\theta) & \text{if } \theta_{min} \leq \theta \leq \theta_{max} \\ F_{11}(\theta_{max}) & \text{if } \theta_{max} < \theta \leq \pi \end{cases} .$$

Similarly, the asymmetry parameter is given by the integral

$$g(t) = \frac{1}{2\beta_{sca}(t)} \int_0^\pi F_{11}^{all}(\theta, t) \cdot \cos(\theta) d\theta. \quad (2.49)$$

The nearest neighbor assumption has the potential for significant improvement and may introduce significant error in these products, especially in cases where a strong forward scattering peak is present. It is important to note though that the truncation error only affects the integrated products and does not play a role in the final  $F_{ij}$  values, regardless of the truncation correction employed.

## 2.5 Estimating Errors

### 2.5.1 Systematic Calibration Errors

This section will examine errors in aerosol and Rayleigh scattering matrix elements ( $X_{11}$  and  $X_{12}$ ) that have no time dependence over the course of a given angular calibration. The overwhelming majority of this time-independent error is produced by uncertainty in the value of the scattering plane Stokes  $q$ . Uncertainties in total scattering and depolarization corrections for the calibration gases can also contribute to systematic instrumental error but a separate sensitivity analysis (not shown here) concluded that these contributions were very small compared to errors resulting from uncertainty in  $q$ . Therefore, only errors in  $q$  are considered here in order to obtain relatively simple, intuitive error formulas, that can be easily be applied to all data, even after the initial processing is complete.

In addition to errors directly effecting the independent variable it is important to account for the uncertainty in  $\theta$ . One option is to estimate the resulting errors in  $F_{ij}$  from the partial derivative with respect to  $\theta$  and then add the result to the other  $F_{ij}$  errors in quadrature. If the situation permits, a better approach is to simply express the  $\theta$  uncertainty explicitly as an error in the independent variable. The angle calibration procedure described in Section 2.3 can determine the value  $\theta$  to an accuracy of about  $1^\circ$ . If measurements of PSL spheres are available, the angle calibration can be further constrained, generally to better than  $0.5^\circ$ . Because of the wide range of approaches for dealing with  $\theta$  error, as well as our goal of keeping this error model simple, errors in  $\theta$  will be ignored for the rest of this section. It should be noted though that the errors in  $\theta$  are correlated with other errors, including  $\eta$  (and in turn the scattering plane Stokes  $q$ ) and the calibration slopes and offsets (the

simulated Rayleigh is a function of  $\theta$ ).

We will now derived equations for the errors in  $X_{11}$ ,  $X_{12}$  and  $-X_{12}/X_{11}$  resulting from uncertainties in  $q_{n,k}$ . Both the calibration and measurement processes will be modeled simultaneously so that correlations in the errors produced by each step are considered. It can be shown that the correlations in the errors of these two steps results in a significant decrease in the total systematic error as the errors in  $m_{n,k}$ , resulting from uncertainties  $q_{n,k}$ , can partially cancel the portion of the measurement uncertainty that is driven by  $q_{n,k}$ . To derive error equations that are only functions of scattering matrix elements and  $\sigma_q$ , the error in  $q$ , several simplifications will be made to the measurement model of Section 2.4. The assumptions made in this section are:

1. The input polarizations are assumed to parallel and perpendicular to the scattering plane and have some normally distributed error  $\sigma_q$ . The assumption of “ideal” polarization states is only made during the steps immediately prior to the final error equations and could therefore be dropped relatively easily but the resulting equations would contain the variables  $q_{n,k}$ , whose values are often not available when the error is calculated.
2. The errors of in the Stokes vectors of the two polarization states are uncorrelated but have the same magnitude on average. The assumption of uncorrelated polarization errors is not always true as the values of  $q_{1,k}$  and  $q_{2,k}$  are determined from the same value of  $\eta$ , which contains its own error.
3. There is no depolarization correction for the simulated Rayleigh scattering signal and in turn this parameter has no uncertainty. Error in the depolarization corrections does have the ability to slightly bias the calibration slope but this is a very small affect when we calibrate using the  $n = 1$  polarization state (see Section 2.4.2).

4. There is no uncertainty in the Rayleigh scattering coefficients taken from the literature.
5. The absolute values of the 2<sup>nd</sup>, 3<sup>rd</sup> and 4<sup>th</sup> elements of the first row of the Muller matrix are all zero. Measurements suggest that these values may be quite low but at the upper ends of the bounds they could still meaningfully effect the recovered scattering matrix elements. Future characterization of these elements, using techniques with better accuracy, will provide useful information as to the significance of this effect.
6. Only the calibration slope  $m_{n,k}$  will be considered in our mathematical model and we will assume  $m_{1,k} = m_{2,k} = m_k$ . The error in the calibration offsets will be ignored here as it will be accounted for in the time-dependent error term and its correlations with the errors caused by uncertainty in  $q$  are expected to be very small.
7. We will ignore all laser power corrections (i.e.  $\xi = \Gamma = \chi = 1$ ). Again, the direct result of these errors is taken into account in the time-dependent error and the resulting errors are not expected to correlate strongly with errors from  $q$ .
8. There is no error in the dependent variable  $\theta$ .

The model of our instrument, given the above assumptions, is identical for the forward and backward beams so we will drop the subscript  $k$  from this point on. While the math is in general valid for both beams, it important that the first  $n = 1$  polarization state corresponds to the “strong polarization” used to find the shape of Rayleigh calibration slope. It is common for the forward and backward scattering planes to be separated by almost exactly  $90^\circ$ , in which case the  $n$  subscripts in this

subsection will reverse between the two beams (i.e. the image corresponding to  $n = 1$  for the forward beam will be  $n = 2$  for the backward beam). Additionally, the explicit  $\theta$  dependence, common to all variables in this section, will be dropped. The explicit  $t$  dependence will also be omitted from the scattering matrix elements for compactness. Therefore, the mathematical model of the instrument, used to estimate the error in  $q$ , under assumptions 5-7 is represented as

$$I_1(t) = m(X_{11} + q_1 X_{12}) \quad (2.50)$$

$$I_2(t) = m(X_{11} + q_2 X_{12}) \quad (2.51)$$

Equations 2.21 and 2.25 can then be used to eliminate explicit references to  $m$  and the resulting equations can be solved for the first two scattering matrix elements

$$X_{12} = \left( \frac{R_{11} + q_1 R_{12}}{I_1(t_{gas})} \right) \frac{I_1(t) - I_2(t)}{q_1 - q_2} \quad (2.52)$$

$$X_{11} = \frac{1}{2} \left( \left( \frac{R_{11} + q_1 R_{12}}{I_1(t_{gas})} \right) (I_1(t) + I_2(t)) - (q_1 + q_2) X_{12} \right). \quad (2.53)$$

### **Errors in $X_{12}$ from $q_n$**

To find the errors in the scattering matrix elements produced by uncertainties in  $q_n$  we must first find the corresponding partial derivatives. We will begin with  $X_{12}$  as it is contained within the definition of Equation 2.53 and the result can be reused in the next sub-section. We start by differentiating Equation 2.52 with respect to  $q_1$  which

yields

$$\frac{\partial X_{12}}{\partial q_1} = -\frac{(I_1(t) - I_2(t))(q_2 R_{12} + R_{11})}{I_1(t_{gas})(q_1 - q_2)^2}. \quad (2.54)$$

After substituting Equation 2.52 back into the result and performing some algebra the right-hand side (RHS) becomes:

$$\frac{\partial X_{12}}{\partial q_1} = -\frac{X_{12}(q_2 R_{12} + R_{11})}{(q_1 - q_2)(q_1 R_{12} + R_{11})} \quad (2.55)$$

If we use the definitions of  $R_{ij}$  from Equations 2.22 and 2.23 and apply assumptions 1 and 3 and we can simplify the above result to

$$\frac{\partial X_{12}}{\partial q_1} = \frac{X_{12}(-\sin^2(\theta) + \cos^2(\theta) + 1)}{2(\sin^2(\theta) + \cos^2(\theta) + 1)} \quad (2.56)$$

which, given the use the Pythagorean formula for sines and cosines ( $\sin^2(\theta) + \cos^2(\theta) = 1$ ), can be further simplified to

$$\frac{\partial X_{12}}{\partial q_1} = \frac{1}{2}X_{12}(1 - \sin^2(\theta)). \quad (2.57)$$

Next, we determine the derivative of  $X_{12}$  with respect to  $q_2$ :

$$\frac{\partial X_{12}}{\partial q_2} = \frac{(I_1(t) - I_2(t))(q_1 R_{12} + R_{11})}{I_1(t_{gas})(q_1 - q_2)^2}. \quad (2.58)$$

Again substituting Equation 2.52 back into the result and rearranging gives

$$\frac{\partial X_{12}}{\partial q_2} = \frac{X_{12}}{q_1 - q_2}. \quad (2.59)$$

If assumption 1 is made the above equation reduces to

$$\frac{\partial X_{12}}{\partial q_2} = \frac{X_{12}}{2}. \quad (2.60)$$

Assumption 2 dictates that the total systematic error in  $X_{12}$  is then equal to the individual  $q_1$  and  $q_2$  errors summed in quadrature:

$$\sigma_{X_{12}}^2 = \frac{\partial X_{12}}{\partial q_1}^2 \sigma_q^2 + \frac{\partial X_{12}}{\partial q_2}^2 \sigma_q^2. \quad (2.61)$$

We can substitute in Equations 2.57 and 2.60, group like terms and make a second use of the Pythagorean formula for sines and cosines to obtain a final expression for the  $X_{12}$  error

$$\sigma_{X_{12}}^2 = \frac{\sigma_q^2 X_{12}^2}{4} (1 + \cos^4(\theta)) \quad (2.62)$$

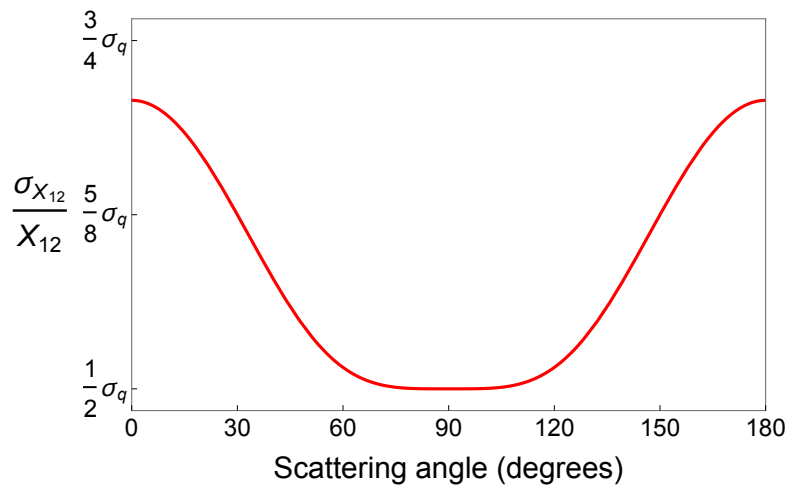


Figure 2.7: The theoretical relative uncertainty in  $X_{12}$  resulting from uncertainty in  $q_1$  and  $q_2$  as a function of scattering angle  $\theta$  in units of  $\sigma_q$ . The error in the scattering plane  $q$  is generally on the order of 0.05, which would produce an expected relative error in  $X_{12}$  of 2.5% to 3.5%, depending on the value of  $\theta$ .

### Errors in $X_{11}$ from $q_n$

The first step to finding the  $X_{11}$  errors is to differentiate Equation 2.53 with respect to  $q_1$  and  $q_2$ .  $X_{12}$  is contained within this equation and is a function of  $q_2$ . The product rule for differentiation will allow us to make use of the quantities  $\frac{\partial X_{12}}{\partial q_n}$  which have already been established. We begin by differentiating with respect to  $q_1$  to obtain

$$\frac{\partial X_{11}}{\partial q_1} = \frac{1}{2} \left( \frac{(I_1(t) + I_2(t)) R_{12}}{I_1(t_{gas})} - X_{12} - (q_1 + q_2) \frac{\partial X_{12}}{\partial q_1} \right). \quad (2.63)$$

We multiply the top and bottom of the first term on the RHS by  $R_{11} + q_1 R_{12}$  to obtain

$$\frac{(R_{11} + q_1 R_{12})(I_1(t) + I_2(t))}{2I_1(t_{gas})} \frac{R_{12}}{R_{11} + q_1 R_{12}} - \frac{X_{12}}{2} - \frac{(q_1 + q_2)}{2} \frac{\partial X_{12}}{\partial q_1} \quad (2.64)$$

where the first factor of the first term is equal to  $X_{11}$  given assumption 1. We then apply assumption 1 to the other instances of  $q_n$  and substitute in the definitions of  $R_{ij}$  under assumption 3 to obtain

$$\frac{\partial X_{11}}{\partial q_1} = -\frac{X_{11} \sin^2(\theta)}{\sin^2(\theta) + \cos^2(\theta) + 1} - \frac{X_{12}}{2} \quad (2.65)$$

which the Pythagorean formula for sines and cosines allows us to simplify to:

$$\frac{\partial X_{11}}{\partial q_1} = \frac{1}{2} (X_{12} - X_{11} \sin^2(\theta)). \quad (2.66)$$

There is no  $q_2$  dependence in the first term of Equation 2.53 so when we

differentiate with respect to  $q_2$  we simply obtain

$$\frac{\partial X_{11}}{\partial q_2} = -\frac{1}{2} \left( X_{12} + (q_1 + q_2) \frac{\partial X_{12}}{\partial q_1} \right). \quad (2.67)$$

The second term of this equation falls out when we apply assumption 1 and we are only left with

$$\frac{\partial X_{11}}{\partial q_2} = -\frac{1}{2} X_{12}. \quad (2.68)$$

If we sum the  $q_1$  and  $q_2$  errors terms, derived from Equations 2.66 and 2.68, in quadrature we obtain

$$\sigma_{X_{11}}^2 = \left( \frac{1}{2} (X_{12} - X_{11} \sin^2(\theta)) \right)^2 \sigma_q^2 + \left( \frac{1}{2} X_{12} \right)^2 \sigma_q^2. \quad (2.69)$$

If we expand the above equation and combine like terms we obtain a final equation for the  $X_{11}$  systematic error

$$\sigma_{X_{11}}^2 = \frac{1}{2} \sigma_q^2 \left( \frac{1}{2} X_{11}^2 \sin^4(\theta) + X_{11} X_{12} \sin^2(\theta) + X_{12}^2 \right). \quad (2.70)$$

### **Errors in $-X_{12}/X_{11}$ from $q_n$**

The ratio  $-F_{12}/F_{11}$  is often intuitively more interesting than  $F_{12}$  alone and is therefore provided more frequently. In Imaging Nephelometers there are some sources of error that can affect  $F_{11}$  and  $F_{12}$  in roughly equal proportion and partially ratio out in  $-F_{12}/F_{11}$ . It is therefore informative to examine the  $-F_{12}/F_{11}$  error as a whole, rather than assume separate, uncorrelated error functions for  $F_{11}$  and  $F_{12}$ . The rest of this section will be dedicated to examining the errors resulting from  $q_n$  on  $-X_{12}/X_{11}$ .

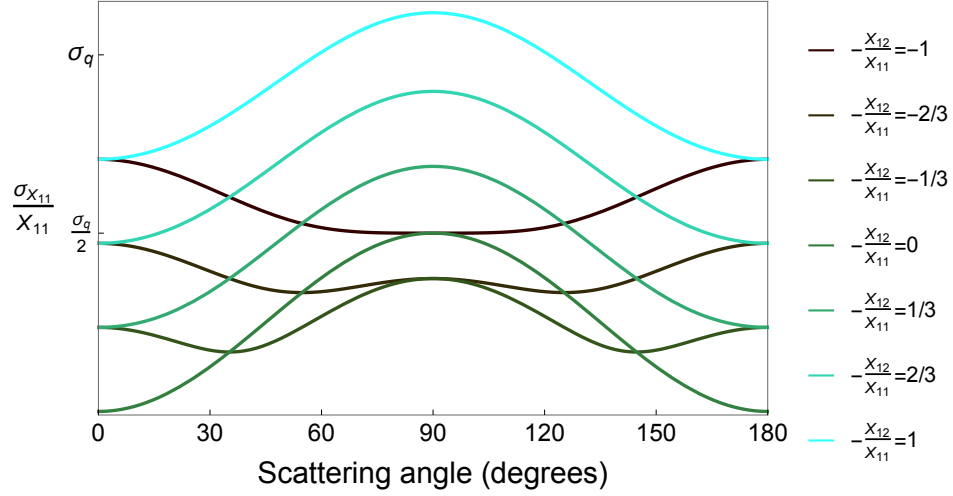


Figure 2.8: The theoretical relative uncertainty in  $X_{11}$  resulting from uncertainty in  $q_1$  and  $q_2$  as a function of scattering angle  $\theta$  in units of  $\sigma_q$ . Uncertainties are shown for several different values of  $-X_{12}/X_{11}$ , ranging from negative one to positive one.

Dividing Equation 2.52 by Equation 2.53 and simplifying produces the equation

$$DOLP = -\frac{X_{12}}{X_{11}} = -\frac{I_1(t) - I_2(t)}{I_2(t)q_1 - I_1(t)q_2}. \quad (2.71)$$

It is interesting to note that this equation is independent of any gas calibration measurements (i.e.  $I_n(t_{gas})$ ). This implies that under assumption 6 and 7 the values of  $-F_{12}/F_{11}$  can be determined without performing a gas calibration.

In order to calculate the error in  $DOLP$  from  $q_n$  we must again calculate the two corresponding partial derivatives. Differentiating with respect to  $q_1$  produces the equation

$$\frac{\partial \left( \frac{X_{12}}{X_{11}} \right)}{\partial q_1} = \frac{(I_2(t) - I_1(t)) I_2(t)}{(I_2(t)q_1 - I_1(t)q_2)^2}. \quad (2.72)$$

We see from the definition of  $DOLP$  in Equation 2.71 that this can be rewritten as

$$\frac{\partial \left( \frac{X_{12}}{X_{11}} \right)}{\partial q_1} = -\frac{X_{12}}{X_{11}} \frac{I_2(t)}{I_2(t)q_1 - I_1(t)q_2}. \quad (2.73)$$

Next we apply assumption 1 regarding the orientation of the input Stokes vectors to obtain

$$\frac{\partial \left( \frac{X_{12}}{X_{11}} \right)}{\partial q_1} = \frac{X_{12}}{X_{11}} \frac{I_2(t)}{I_1(t) + I_2(t)} \quad (2.74)$$

which can be written as

$$\frac{\partial \left( \frac{X_{12}}{X_{11}} \right)}{\partial q_1} = \frac{X_{12}}{X_{11}} \left( \frac{I_2(t) - I_1(t)}{2(I_1(t) + I_2(t))} + \frac{1}{2} \right). \quad (2.75)$$

We can now substitute the definition of DOLP into the RHS of the above equation a second time to obtain a final expression for the derivative

$$\frac{\partial \left( \frac{X_{12}}{X_{11}} \right)}{\partial q_1} = \frac{1}{2} \frac{X_{12}}{X_{11}} \left( 1 - \frac{X_{12}}{X_{11}} \right). \quad (2.76)$$

Differentiating  $X_{12}/X_{11}$  with respect to  $q_2$  produces the equation

$$\frac{\partial \left( \frac{X_{12}}{X_{11}} \right)}{\partial q_2} = \frac{(I_1(t) - I_2(t)) I_1(t)}{(I_2(t)q_1 - I_1(t)q_2)^2} \quad (2.77)$$

Again, if we substitute in  $X_{12}/X_{11}$  from Equation 2.71 we obtain

$$\frac{\partial \left( \frac{X_{12}}{X_{11}} \right)}{\partial q_2} = \frac{X_{12}}{X_{11}} \frac{I_1(t)}{I_2(t)q_1 - I_1(t)q_2} \quad (2.78)$$

which, using a method similar to the one used in the  $q_1$  case, can be reduced to

$$\frac{\partial \left( \frac{X_{12}}{X_{11}} \right)}{\partial q_2} = -\frac{1}{2} \frac{X_{12}}{X_{11}} \left( \frac{X_{12}}{X_{11}} + 1 \right). \quad (2.79)$$

To obtain the final expression of the error in DOLP we sum the two  $q_n$  error terms in quadrature

$$\sigma_{DOLP}^2 = \left( \frac{1}{2} \frac{X_{12}}{X_{11}} \left( 1 - \frac{X_{12}}{X_{11}} \right) \right)^2 \sigma_q^2 + \left( -\frac{1}{2} \frac{X_{12}}{X_{11}} \left( \frac{X_{12}}{X_{11}} + 1 \right) \right)^2 \sigma_q^2. \quad (2.80)$$

After expanding and combining like terms we obtain a final equation for the  $X_{12}/X_{11}$  error

$$\sigma_{DOLP}^2 = \frac{1}{2} \left( \frac{X_{12}}{X_{11}} \right)^2 \left( \left( \frac{X_{12}}{X_{11}} \right)^2 + 1 \right) \sigma_q^2. \quad (2.81)$$

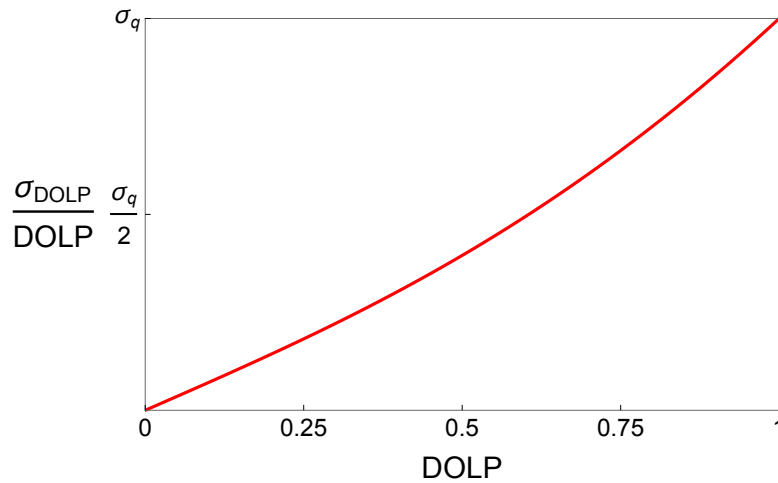


Figure 2.9: The theoretical relative uncertainty in  $-X_{12}/X_{11}$  (*DOLP*) resulting from uncertainty in  $q_1$  and  $q_2$  as a function of  $-X_{12}/X_{11}$  in units of  $\sigma_q$ . Errors in  $-X_{12}/X_{11}$  can be seen to increase monotonically with the value of  $-X_{12}/X_{11}$  up to a peak value of  $\sigma_q$ .

There is no  $q$  dependence on the Rayleigh subtraction or temperature and pressure correction so the error resulting from uncertainty in  $q$  will be the same in both  $X_{ij}$  and  $F_{ij}$ . There are other errors that will be introduced during the Rayleigh subtraction, beyond those explicitly dismissed by assumptions 3 and 4, like errors resulting from uncertainty in  $\theta$ . Additionally, errors can be introduced by uncertainties in the temperature and pressure measurements used to convert from the measure-

ment conditions to STP (see Equation 2.43). These errors are both relatively straightforward to calculate and can simply be added to the  $q$  and time-dependent errors quadrature. The uncertainty estimates discussed and shown throughout the rest of this work include these  $\theta$ , temperature and pressure errors.

### 2.5.2 Time-dependent Errors

In addition to the errors that are fixed for a given calibration, Imaging Nephelometers contain sources of error whose magnitude can change from one image pair to the next. A list of the most significant sources of this type of error include:

- Errors resulting from insufficient particle statistics – Local variations in particle number density can create artificial features in the corresponding radiance measurements. This effect is most pronounced when large particles (with large scattering cross sections) are prevalent enough to frequently enter the sample volume but still compose a relatively small fraction of the total size distribution.
- Detection non-idealities – This category includes photon counting noise and slight deviations in dark current produced primarily by small changes in CCD temperature. Note that the CCD is stabilized with a thermoelectric cooler so once the instrument has stabilized (about 30 minutes from startup time) deviations in dark current are very small.
- Variations in the stray light offset  $r_{n,k}$  – These variations are caused by changes in instrument alignment after the gas calibration and can vary significantly over the course of several images.
- Laser power corrections ( $\xi$ ,  $\chi$  and  $G$ ) – As these variables are dependent on a wide array of quantities (see Equations 2.37 and 2.38) virtually all other error

sources described here can affect their value. The contributing factors include errors that are independent of time (ex.  $q_{n,k}$ ) so strictly speaking there is also a systematic component of this error that is being neglected.

In principle, all of the above errors can be determined empirically (except for the systematic component of the laser power corrections) by examining a sufficiently long measurement time series of a stable aerosol sample. Unfortunately, correlations in these errors over time both complicates this approach and significantly increases the number of measurements required to properly characterize the error. Attempts have been made to explicitly quantify these errors from the base uncertainties that are well known (ex. polarimeter reading uncertainty, shot noise, error in angle calibration distance measurements, etc.) but historically the individual components of the data processing algorithm were always treated separately, only passing on one value for the error (as opposed to the entire covariance matrix) at each stage. The correlations that are lost in this approach are quite significant and it was decided that an empirical approach would yield the most realistic error estimates until a full error model of the system, that takes all these features into account simultaneously, can be created. The rest of this subsection provides an explanation of the empirical approach used to estimate the errors presented in this work.

We can model the error of a given measurement  $y_t = \mu_t + \epsilon_t$ , where  $y_t$  represents the measured value ( $F_{11}(t)$  or  $F_{12}(t)$ ),  $\mu_t$  is the true value and  $\epsilon_t$  is the error of a given measurement (pair of images), all at time  $t$ .

It can be assumed that each member of  $\epsilon_t$  contains some autocorrelation that decreases with the time between observations such that

$$\epsilon_t = p\epsilon_{t-1} + a_t \tag{2.82}$$

where the  $a_t$  term represents time independent normally distributed errors. In an actual measurement, the  $\epsilon_t$  term is actually made of multiple error terms (one for each time-dependent source of error), each of which would have a unique value of  $p$  in the above model. In order to simplify the math, as well as estimate the correlation of the errors with a reasonably small number of measurements, we will assume that there is a single value of  $p$  that represent the behavior of all errors summed together relatively effectively. Under this model we can estimate the autocorrelation coefficient  $p$  using the methods presented by Prais and Winsten [1954]

$$p \approx \frac{\sum_{t=2}^T \hat{r}_t \hat{r}_{t-1}}{\sum_{t=2}^T \hat{r}_t^2} \quad (2.83)$$

where  $T$  is the total number of measurement of the same aerosol,  $\hat{y}$  is the mean of all measurements of that aerosol and  $\hat{r}_t = y_t - \hat{y}$ . While many methods exist for estimating autocorrelation coefficients, the Prais-Winsten technique is used here due to its low bias in situations with relatively small sample sizes [Bence, 1995]. It is rarely possible to keep the aerosol properties constant inside an Imaging Nephelometer's sample volume for longer than ten minutes, so averaging is almost always limited to around 50 samples or less.

We now want to find a correction factor  $k$  such that the expected value of  $k \cdot s$  is the standard deviation of  $\bar{y}$  under the error assumptions above and  $s$  is given by the usual formula for the standard error of the mean

$$s^2 = \frac{\sum_{t=1}^T \hat{r}_t^2}{T(T-1)}. \quad (2.84)$$

Note that if all  $T$  samples are taken during a period when the aerosol scattering properties are stable  $\mu_t$  is a constant and the standard deviation of  $\bar{y}$  represents the uncertainty stemming from  $\epsilon_t$ . If the value of  $p$  is known exactly, the correction factor is given by

$$k = \sqrt{\frac{1 + 2b/T}{1 - 2b + 2b/T}} \quad (2.85)$$

where

$$b = \frac{(T - 1)p - Tp^2 + p^{T+1}}{(1 - p)^2} \quad (2.86)$$

[Stewart-Oaten et al., 1986; Bence, 1995]. The value of  $k$  can then be estimated using the approximated autocorrelation coefficient of Equation 2.83.

It is often significantly more difficult to maintain a constant aerosol loading than it is to keep the intensive properties of the aerosol constant. For this reason, the normalized phase function ( $\tilde{F}_{11}$ ) and DOLP ( $-F_{12}/F_{11}$ ) are generally used in to compute  $p$ , as these products are insensitive to total particle concentration. The downside of this approach is that the resulting autocorrelation coefficient does not include the correlations in the error of  $\xi$ , as errors in laser power have almost no effect on the normalized scattering matrix elements. In the PI-Neph the autocorrelation coefficients in  $\tilde{F}_{11}$  and  $-F_{12}/F_{11}$  are generally fairly small, typically ranging from 0.1 to 0.3 ( $1 < k < 1.3$ ), depending on wavelength, aerosol concentration, and particle properties.

Once the value of this correction parameter has been estimated the standard error of the mean of the corresponding aerosol measurements can be calculated by multiplying the result of Equation 2.84 by  $k$ . As this resulting time-dependent error term will vary with  $F_{11}$  and  $F_{12}$  it has to be recalculated for each aerosol sample, but the relative magnitude of the time-dependent error, for a typical ambient aerosol,

is generally around several percent in both  $F_{11}$  and  $F_{12}$ . The fact that this error is empirically determined for each aerosol independently can make error estimation difficult in situations where many measurements are not available for a fixed set of intensive properties. Other approaches, that do not share this limitation, are discussed in Section 2.5.3.

The total time varying error, and the autocorrelation coefficient, will vary as a function of angle so each of these values must be calculated independently at each scattering angle. Once this time-dependent error is found at all angles it can be added in quadrature to the errors discussed in Section 2.5.1 to obtain estimates of the total error.

### 2.5.3 Future Approaches to Instrumental Error

The best approach to Imaging Nephelometer error estimation would be to combine all the equations of Section 2.4 and 2.3 together and take partial derivatives with respect to all of the most basic calibration parameters. The uncertainties of all of these base parameters should be fairly straight forward to estimate, and in many cases the values are provided by the instrument manufacturer (ex. Thorlabs Polarimeter). These uncertainties can then be multiplied by the corresponding partial derivatives and then all error terms can be summed in quadrature to obtain a formula for the total systematic *and* time-dependent error. As all errors in the base calibration parameters should be almost entirely uncorrelated this result should produce the most realistic error model possible. While the formulas involved can be quite long, the use of a symbolic computation program like Mathematica should make the process very tractable.

In addition to deriving an explicit analytic equation for the instrumental er-

ror the uncertainties could be estimated using a Monte Carlo simulation. A limited version of this approach is used by Dolgos and Martins [2014] to estimate the errors associated with measurements of PSL spheres. Additionally, Espinosa et al. [2017] used a similar approach to estimate the errors of aerosol parameters retrieved from PI-Neph data. In both cases the error sources modeled by the Monte Carlo simulation included only a minority of all possible error sources but future, more detailed simulations, should in principle be able to simulate all meaningful sources of error.

## CHAPTER 3

# Retrievals of Aerosol Optical and Microphysical Properties from I-Neph Measurements

This chapter is an adaptation of original work published in *Atmospheric Measurement Techniques* **10**, 811-824 (2017).

### 3.1 Introduction

Optical particle sizers are among the most precise particle sizing instruments available, but all OPC designs still require significant assumptions about the aerosol being sampled. These assumptions, generally regarding real refractive index, absorption and particle morphology can lead to significant biases in the resulting particle size distributions and generally constitute the bulk of the measurement error [Pinnick

et al., 2000]. Additionally, in situ measurements of many of these characteristics, like aerosol refractive index or particle sphericity for example, are still virtually nonexistent, especially at altitudes far from the surface.

A less common approach to characterizing particles is through polar nephelometer measurements of light scattering from an ensemble of particles over a large number of angular regions. This approach provides a large amount of information about the sample, reducing the total number of assumptions required and the resulting biases in the retrieved products. Unfortunately, deploying field instruments with these capabilities can be quite challenging, and airborne measurements of common aerosols using this technique have previously been unavailable. Additionally, the inversion of multi-angular data, is significantly more complex than the inversion of light scattering intensity over a single angular range.

In spite of the complexities associated with multi-angle measurements and the corresponding inversions, there have been several successful attempts over the past four decades to retrieve particle properties from polar nephelometer data. The first published inversion of this kind was made by Eiden in 1966, who used multi-wavelength polarization data to retrieve the complex refractive index of an ambient aerosol, as well as match one of three predefined aerosol PSD models [Eiden, 1966]. Jones et al. [1994] used intensity measurements to size monodisperse PSL spheres, as well as determine their complex index of refraction. Intensity and polarization measurements of ambient aerosols made by the Tohoku University single wavelength polar nephelometer in Sendai, Japan have been inverted to obtain complex refractive index and number concentrations in six log spaced size bins [Tanaka et al., 1983; Zhao, 1999]. There have also been attempts to retrieve only the refractive index, while constraining the model's size distribution with a traditional particle sizer [Barkey et al., 2007, 2010]. The converse approach was reported by Lienert et al. [2003], who took

polarized measurements of sea spray and determined PSD by assuming a refractive index value expected for sodium chloride particles at the ambient relative humidity. Most recently, Sviridenkov et al. [2014] obtained both complex refractive index and PSD from three wavelength intensity measurements made with a commercially available polar nephelometer. All of these retrieval efforts have assumed spherical particles, and all measurements were made in the visible spectrum, except in the case of Jones et al. [1994] who used measurements made in the near-infrared. The only polar nephelometer retrievals to incorporate a non-spherical component in the scattering model were performed by Dubovik et al. [2006], who fit laboratory measurements of desert dust.

In this chapter we apply a complex inversion algorithm, specifically the Generalized Retrieval of Aerosol and Surface Properties (GRASP), to airborne and laboratory measurements made with the Polarized Imaging Nephelometer (PI-Neph), a multi-wavelength, multi-angle light scattering instrument. The GRASP retrieval makes no assumptions about the number of modes in the size distribution or the complex refractive index, and it allows for both spherical and spheroidal scatterers. This represents a significant increase in complexity when compared to previous in situ scattering inversions. In addition to the generality of the retrieval, this work represents the first time that any aerosol retrieval algorithm has been applied to airborne polar nephelometer measurements. Furthermore, the ambient airborne measurements presented here were made in parallel to a large variety of independent instrumentation, allowing for very robust inter-comparisons of the retrieved products.

## 3.2 Inversion Methodology

Aerosol scattering matrix elements are measured in situ with a polar nephelometer and feed into a microphysical retrieval algorithm in order to obtain aerosol size distribution, complex refractive index ( $m$ ) and a percentage of spherical particles. These measurements include a combination of artificially suspended laboratory data as well as airborne data taken over the continental United States during the SEAC<sup>4</sup>RS field experiment in 2013. GRASP, a versatile open source software package (<http://www.grasp-open.com>) capable of performing inversions on a wide variety of atmospheric optical measurements, was used to obtain the retrieved microphysical parameters. A detailed description of the GRASP retrieval algorithm and its capabilities can be found in Dubovik et al. [2011, 2014].

### 3.2.1 Artificial Aerosol Generation

Ammonium sulfate ( $(NH_4)_2SO_4$ ), ammonium nitrate ( $NH_4NO_3$ ), and Sodium Chloride ( $NaCl$ ) were suspended and humidified in a laboratory setting. Figure 3.1 displays a schematic diagram of the particle generation and measurement setup. The salts were diluted with distilled water to a concentration of  $5\text{gl}^{-1}$  before being agitated with an ultrasonic vibrator and later suspended using a single jet atomizer (TSI, model 9302). The generated aerosol was diluted with filtered compressed air before being fed into a dryer and then a humidifier. In the first stage, generated particles are dried, without heating, to a relative humidity less than 30% using a Perma Pure Nafion dryer. The dry particles are later humidified to a  $RH > 80\%$  using two Perma Pure Nafion humidifiers (Nafion1 and Nafion2). The humidifier and dryer consist of a Nafion membrane tubing that transfers moisture to or from the surrounding medium.

The drier uses compressed air while the air passing through Nafion 1 is humidified by flowing water and then used to humidify the sample passing through Nafion 2. The separation of liquid water from the Nafion tube in contact with the aerosol sample allows for subtler control of the final relative humidity [Orozco et al., 2016]. Angular scattering measurements of the aerosol were then made by the PI-Neph before the sample was discharged from the system.

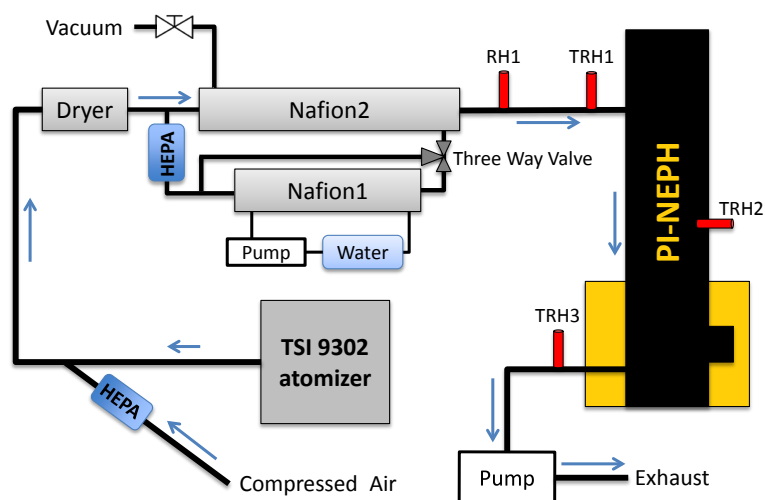


Figure 3.1: Laboratory aerosol generation instrumental setup used to suspend salts and PSL spheres. The temperature and relative humidity of the sample was closely monitored by the array of sensors shown in red.

The humidification system was set to relative humidity values above the deliquescence points of each salt solution, typically to an RH just over 80%. The humidity was continuously monitored throughout the measurement using RH sensors located at the PI-Neph’s inlet, measurement chamber, and outlet. The stability and reproducibility of the particle generation was independently validated by the proper observation of deliquescence of different salts using an integrating nephelometer (model 3563, TSI Inc., St. Paul, MN, USA).

This setup was also used to suspend 903nm diameter monodisperse PSL spheres

(Nanosphere 3900A, ThermoFisher Scientific, Fremont, CA, USA) and scattering measurements of these spheres were made by the PI-Neph at low relative humidities ( $\text{RH} < 20\%$ ). These measurements provide an opportunity to test the retrieval technique on an aerosol with a monodisperse size distribution and a refractive index that is very well characterized. The PSL generation and measurements also allowed for a small, sub-degree re-alignment of the PI-Neph scattering angle calibration in the case of the salt measurements. This correction was not applied to the data used in the PSL retrievals to avoid biasing the result.

### 3.2.2 Ambient Measurements

In addition to the laboratory measurements, inversions were performed on airborne data from the SEAC<sup>4</sup>RS experiment. Fifty separate sampling periods, occurring over the course of ten different flights, are highlighted in this chapter. The flights selected represent the ten days with the highest quality PI-Neph data, for which data is available for at least one of LARGE group's dedicated particle sizers. The intervals containing the highest aerosol scattering levels during these flights were identified and a robust averaging procedure [Beaton and Tukey, 1974] was applied to periods for which no detectable changes in the normalized angular scattering data was observed. The total scattering for these averages ranged from  $30\text{Mm}^{-1}$  to just over  $500\text{Mm}^{-1}$ , with a median value of  $90\text{Mm}^{-1}$ . The resulting dataset represents a wide range of aerosols, including urban pollution, organics, Saharan dust and over a dozen cases dominated by biomass burning (BB) emissions with transport ages ranging from hours to several days.

Additionally, three individual case studies were selected to provide detailed examples of PI-Neph measurements, the corresponding GRASP fit and the resulting

retrieved size distributions. Two of these cases come from periods where the scattering signal was dominated by forest fire emissions, and were chosen to emphasize the subtle distinctions in angular scattering patterns that can occur, even between two aerosols of similar type. The third case consists of boundary layer (BL) measurements made over a heavily forested region of south east Missouri. This case represents one of only a couple of periods in which a significant coarse mode was observed. The sampling locations of these three cases, as well as the flight paths for the ten selected flights, are shown in Figure 3.2.

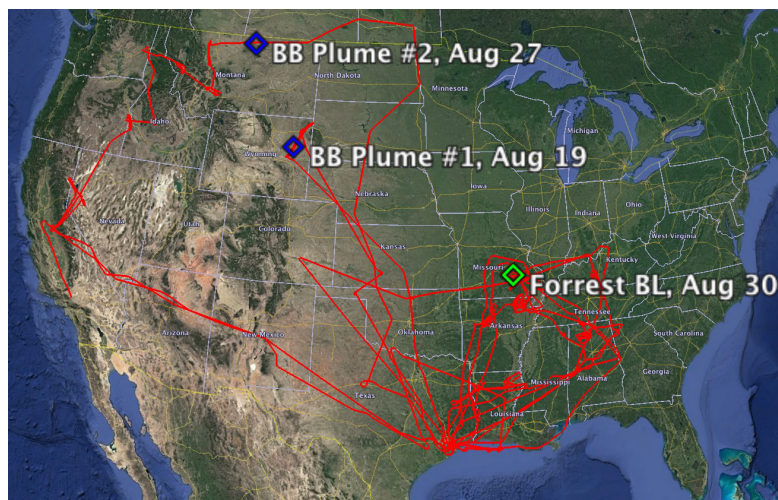


Figure 3.2: Flight paths of the ten SEAC<sup>4</sup>RS flights from which data is used in this chapter. Additionally, three specific case studies are called out with diamonds. The case studies include two biomass burning dominated aerosols (blue) as well as measurements made in the boundary layer of a forested region in south east Missouri (green).

In addition to PI-Neph scattering measurements, the LARGE group made comprehensive in situ measurements of aerosol properties in parallel to the PI-Neph during SEAC<sup>4</sup>RS. These measurements, containing data on particle number density, size distribution and optical properties, are a valuable resource for the inter-comparison of PI-Neph measurements and the corresponding retrieved microphysical properties. In this chapter PI-Neph retrieved size distributions will be compared extensively to

measurements made by two dedicated optical particle size spectrometers (LAS model 3340, TSI Inc., St. Paul, MN, USA and model UHSAS, Droplet Measurement Technologies, Boulder, CO, USA) as well as an aerodynamic particle sizer (APS model 3321, TSI Inc., St. Paul, MN, USA). The two optical particle spectrometers also measured at low relative humidities during SEAC<sup>4</sup>RS, but their sample was conditioned through a drier. This approach minimizes the evaporation of volatile compounds but can also lead to size dependent losses in the aerosol when the instrument requires relatively large flow rates, as is the case for the PI-Neph. The aerodynamic particle sizer measurements were made at ambient humidities, but the ambient RH was determined to be less than 40% in all cases shown here so differences in PSD resulting from hygroscopic growth are not expected.

### 3.2.3 Implementation of GRASP Retrieval

GRASP is a versatile software package capable of retrieving a wide range of atmospheric and surface properties from a variety of datasets. The GRASP algorithm and corresponding software builds on the successful heritage of the PARASOL [Dubovik et al., 2011], AERONET [Dubovik and King, 2000] and laboratory [Dubovik et al., 2006] retrievals. In this work the GRASP inversion algorithm is used to retrieve particle size distribution, real refractive index and fraction of spherical particles from PI-Neph measurement averages.

GRASP's base aerosol model contains very few assumptions in comparison with traditional in situ or remote sensing retrieval algorithms. It includes all necessary components required to simulate a diverse range of atmospheric observations, including remote sensing (both suborbital and space-based), optical in situ and laboratory measurements. The settings of the retrieved characteristics can be flexibly

adjusted to match the particular application. For example, aerosol size distribution can be represented as a superposition of several log-normal functions or as a binned continuous function with different size resolutions (it is defined in nodal points).

As an inversion concept GRASP implements Multi-Term Least Square fitting [Dubovik, 2004]. This approach allows for convenient combining of different types of observations and multiple a priori constraints in a single inversion. For example, following this concept the AERONET retrieval [Dubovik and King, 2000] retrieves many parameters simultaneously: aerosol size distribution, spectral complex refractive index and fraction of spherical particles. A priori constraints on all functions (size distribution and all spectral dependencies) are assumed smooth, while a priori estimates of values are also used for some parameters. Moreover, using the same strategy a statistically optimized multi-pixel retrieval concept was realized as an option in GRASP [Dubovik et al., 2011]. This concept uses additional a priori knowledge about time and space variability of the retrieved parameters in the inversion of coordinated observations (i.e. satellite observations in different pixels).

The flexibility built into the design of GRASP allows the user to select the assumptions that best match the information content of a particular dataset. Moreover, while all of the above features have never been used in one single application, they often provide important potential for evolution of each application, for example via implementing synergy retrievals using a combination of different observations. The GRASP algorithm has previously been successfully applied to both satellite and ground-based upward-looking sky radiance measurements [Dubovik et al., 2011, 2014; Xu et al., 2016], while this study represents the first application of GRASP to polar nephelometer data.

In this work GRASP size distributions were modeled with 16 logarithmically spaced size bins, generally ranging from 50nm to  $2.94\mu\text{m}$  in radius. The lower end

of this range corresponds to the sensitivity limit of ensemble type, light scattering measurements, given realistic particle size distributions. The upper bound was chosen to include the vast majority of coarse mode particles capable of passing through the LARGE inlet, which has a 50% passing efficiency at an aerodynamic radius of  $1.8\mu\text{m}$  [McNaughton et al., 2007]. This size range was reduced to radii between 425nm and 476nm in the case of the PSL spheres, in order to better capture the fine structure of their very narrow size distribution. In all retrievals the shape of the size distribution is only constrained by a smoothness parameter and no assumptions about the number of modes are made. Additionally, the 50nm size bin is forced to zero in all retrievals to limit PSD noise as the distribution approaches the sensitivity limit of the technique. While the aerosols discussed in this work can still have significant number concentrations in the 50nm range, it is shown in section 4.6.1 that these particles generally have a negligible contribution to the total amount visible light scattered by the aerosol.

The search space for the real part of the refractive index ( $n$ ) is semi-continuous between 1.33 and 1.68, while the imaginary part ( $k$ ) can range from 0 to  $10^{-1}$ . The refractive index is held constant with respect to size but, in the case of the multi-wavelength SEAC<sup>4</sup>RS data, it is allowed to vary as a function of wavelength. GRASP's aerosol model assumes a mixture of spheres and spheroids. The spheroid component utilizes a fixed axis ratio distribution that was derived from feldspar measurements made by Volten et al. [2001]. It can be shown that small deviations in the spheroid component's axis ratio distribution produces negligible changes in the angular dependence of the scattered light [Dubovik et al., 2006]. It is therefore believed that this fixed shape distribution is capable of accurately modeling a relatively wide range of non-spherical aerosols. The spheroid component was omitted from the PSL retrievals due the computational demands associated with generating the required

precomputed kernels for the finer size parameter grid spacing.

### 3.3 Retrieval Results and Discussion

#### 3.3.1 Measured Data and Retrieval Fit

In both the 50 selected SEAC<sup>4</sup>RS cases and in the laboratory measurements, the residuals between the GRASP fits and the PI-Neph measured values are generally within the PI-Neph instrumental error. Figure 3.3 shows the measured and fit  $F_{11}$  and  $-F_{12}/F_{11}$  for the ammonium sulfate case, and is typical of the bulk of the retrievals performed in this work. The residuals are also plotted to clearly emphasize the differences between the measurement and fit relative to the instrument's  $2\sigma$  error. In the case of the  $F_{11}$  data the distances between the fit and measured values are reported as:

$$RES_{F_{11}} = \text{Log}_{10}(F_{11}^{MEAS}) - \text{Log}_{10}(F_{11}^{FIT}) \quad (3.1)$$

with the PI-Neph error transformed accordingly. This transformation provides a measure of relative (as opposed to absolute) error, and provides a consistently sized metric across the two orders of magnitude covered by  $F_{11}$ . The separation in  $-F_{12}/F_{11}$  data is represented simply as the difference between the measured and fit values.

$$RES_{F_{12}/F_{11}} = \left(\frac{F_{12}}{F_{11}}\right)^{FIT} - \left(\frac{F_{12}}{F_{11}}\right)^{MEAS} \quad (3.2)$$

Figure 3.4 shows the normalized scattering matrix elements at 532nm for the three selected SEAC<sup>4</sup>RS case studies. A strong forward peak can be seen in the forest boundary layer measurements, which is in accordance with the significant coarse mode observed by the aerodynamic and optical particle sizers. The two biomass burning

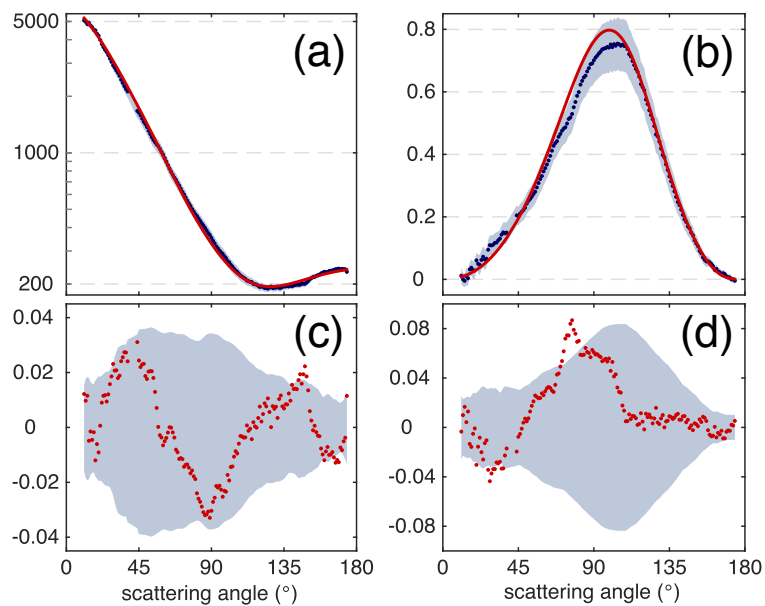


Figure 3.3: PI-Neph measurements at 532nm (points) with  $2\sigma$  instrumental error (gray fill) and the GRASP retrieval best fit (solid line) for ammonium sulfate measurements made in the laboratory. Panel (a) shows absolute  $F_{11}$  ( $Mm^{-1}/sr$ ) data plotted on a log scale, while panel (b) shows  $-F_{12}/F_{11}$  data on a linear scale. Panel (c) shows the  $F_{11}$  differences according to the log transformation described in equation 3.1, while the conventional residuals in  $-F_{12}/F_{11}$ , as given by equation 3.2, are plotted in (d).

cases display very similar  $F_{11}$  values, with the only significant difference being slightly enhanced forward and backward scattering in BB Plume #2. These subtle differences are likely driven by the slightly larger fraction of coarse mode particles present in the latter case. In contrast to  $F_{11}$ ,  $-F_{12}/F_{11}$  shows significant differences between the two biomass burning cases. The reduced magnitude of  $-F_{12}/F_{11}$  in BB Plume #1 is likely driven primarily by differences in real refractive index between the two samples. This hypothesis is supported by simulations with a Mie code [Mishchenko et al., 2002] which demonstrated that, in the relevant size regime, changes in refractive index on the order of 0.03 had little effect on  $F_{11}$  but could easily change the ratio of  $F_{12}$  to  $F_{11}$  by 20% or more. It is this effect, in combination with the small median size of the fine mode, that produces the highest degree of linear polarization of the three samples in the forested boundary layer case.

The spectral dependence of  $F_{11}$  and  $-F_{12}/F_{11}$  for the biomass burning case study sampled on August 19<sup>th</sup> (BB plume #1) is shown in Figure 3.5. The absolute phase function values are shown here to emphasize the additional information present in the spectral dependence of the scattering intensities. It should be noted that there is also significant spectral dependence in the shape of the scattering matrix elements, particularly in  $-F_{12}/F_{11}$ . These differences are driven primarily by changes in size parameter, but also result in some part from a non-zero spectral dependence of the complex refractive index. The same variables are plotted for the forested boundary layer case in Figure 3.6 to show the spectral dependence of the measured scattering matrix elements and the corresponding fits when a significant coarse mode is present. In this last case, low aerosol concentrations and greater than average straylight levels inside the instrument resulted in a gap in the 473nm  $F_{12}$  measurements between 80° and 142° in scattering angle.

In the case of the polydisperse samples, the oscillations occasionally present

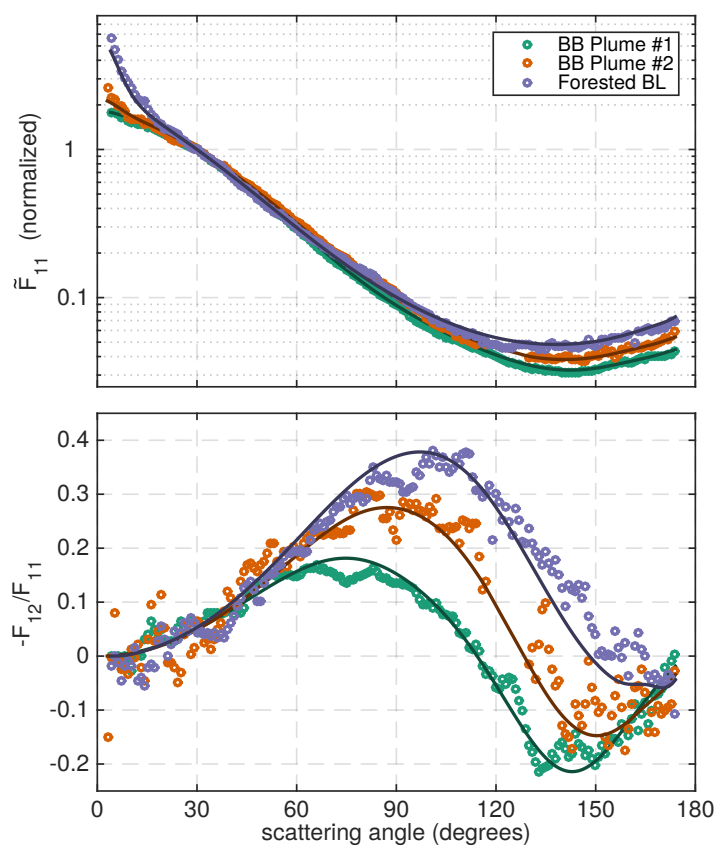


Figure 3.4: Normalized scattering matrix elements (circles) measured by the PI-Neph at 532nm and the corresponding GRASP fits (solid lines) for the three highlighted SEAC<sup>4</sup>RS aerosol samples.

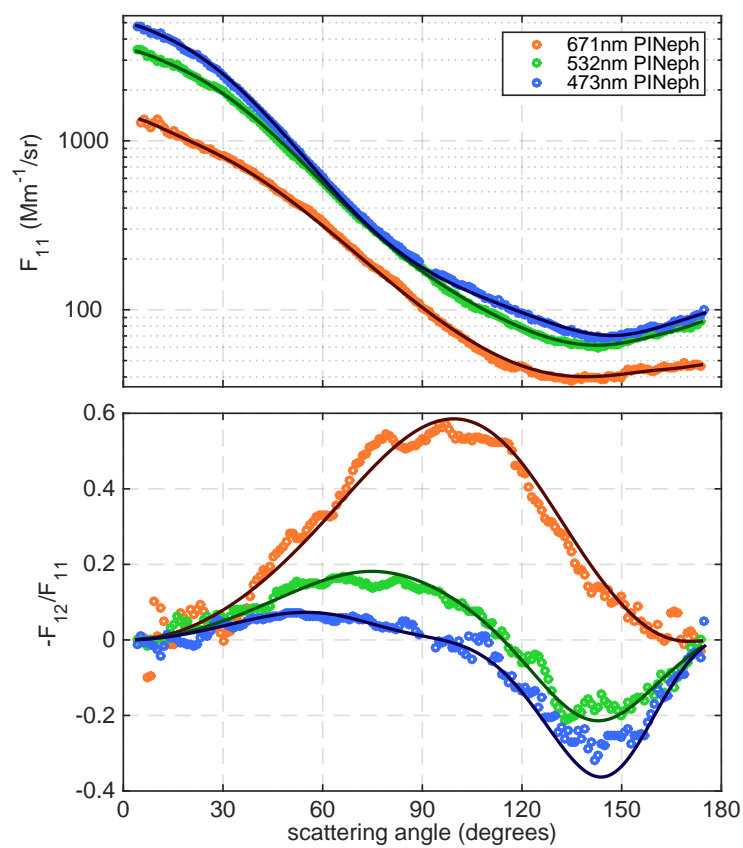


Figure 3.5: Scattering matrix elements at 473nm (blue), 532nm (green) and 671nm (red) measured in BB plume #1 on August 19<sup>th</sup> along with the corresponding GRASP fits (solid lines).

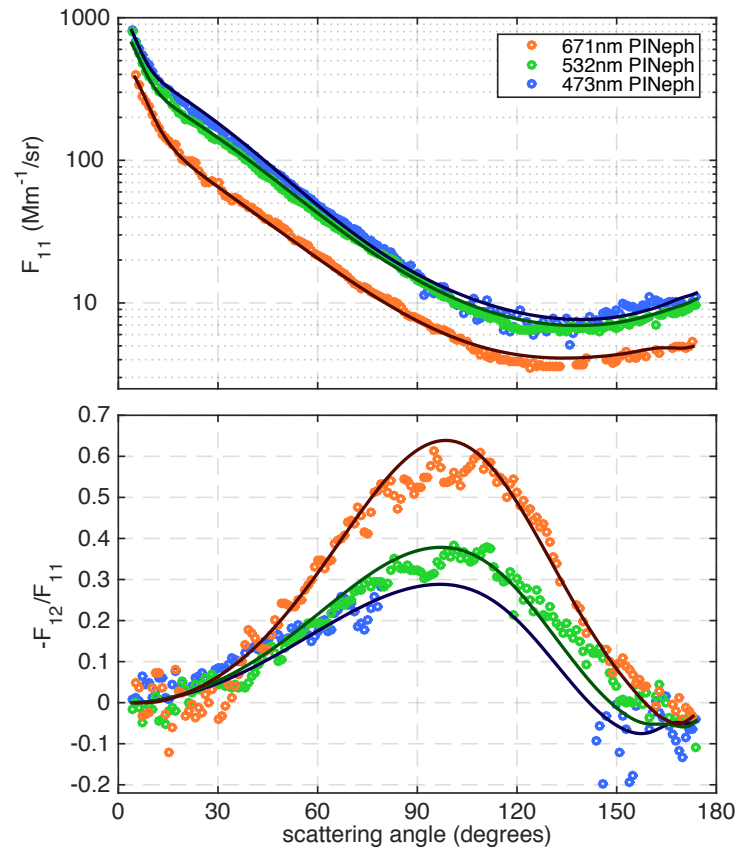


Figure 3.6: Scattering matrix elements at 473nm (blue), 532nm (green) and 671nm (red) measured over a forested region of southeast Missouri along with the corresponding GRASP fits (solid lines).

in the data over angular scales of roughly ten degrees are likely non-physical, and artifacts of insufficient sampling statistics in the coarse mode. The extended length of the imaging nephelometer sample volume makes it especially susceptible to sampling statistic artifacts that are produced by the largest particles. These particles make up a very small fraction of the total number concentration, while simultaneously accounting for a disproportionately large portion of the total scattered light. This is especially apparent in the measurements of  $-F_{12}/F_{11}$  as these values are closely related to the differences between sequential measurements at different polarizations. A large particle that is present at a given location in one image, but not present in the corresponding adjacent image will produce a significant artifact. The effect is also evident at low scattering angles, where larger particles tend to represent a larger portion of total scattering.

The monodisperse PSL measurements and corresponding GRASP fits (shown in Figure 3.7) agree well in the case of  $F_{11}$ . Overall there is also good agreement in the  $-F_{12}/F_{11}$  data, but some significant deviations do occur. The GRASP size distribution retrieval for this case had a full width, 67 percentile (FW67) of 17nm, which is more than twice the width specified by the manufacturer (FW67=8.2nm). However, a narrower size distribution corresponding to the manufacturer's specification was found to reproduce some features of the measurement significantly better than GRASP's original retrieval. This improvement was most apparent in the 473nm and 532nm  $-F_{12}/F_{11}$  data, particularly at scattering angles between  $20^\circ$  and  $60^\circ$  where Mie theory predicts  $-F_{12}/F_{11}$  to have high sensitivity to the distribution's width. Further studies indicated that GRASP was able to reproduce  $-F_{12}/F_{11}$  corresponding to this narrower PSD with high accuracy when noise free synthetic data was used as input. Additionally, running retrievals on the measured data using increasingly finer size resolution kernels did not improve the retrieval's ability to fit these features.

The deviations in the fit were thus determined to be the result of GRASP’s sensitivity to certain characteristics of the noise in the measured data, not insufficient size resolution in the fine resolution kernels used in the PSL case.

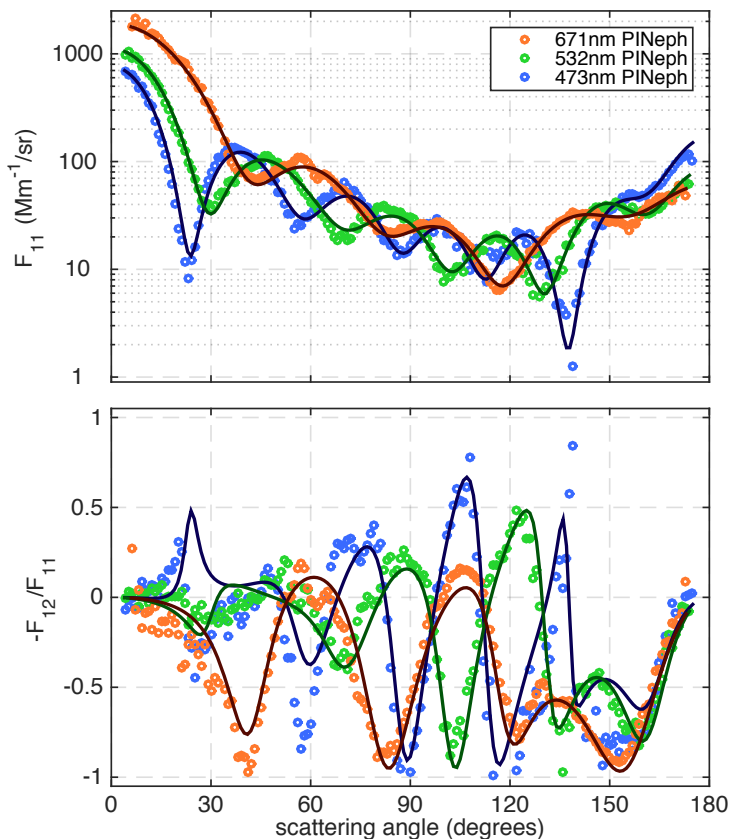


Figure 3.7: Scattering matrix elements at 473nm (blue), 532nm (green) and 671nm (red) for 903nm diameter PSL sample along with the corresponding GRASP fits (solid lines).

### 3.3.2 Refractive Index Retrievals

Crystalline particles do not take on water until reaching relative humidities above their deliquescence point, generally around 80% in the case of salts. A range of methods are available for calculating the size of a given salt droplet, after the transformation to an aqueous state has been made. We choose the parameterization proposed by Petters

and Kreidenweis [2007] for its simplicity and because the required  $\kappa$  parameters are well known for the salts in question. This method states that  $gf_{vol}$ , the volume growth factor of a particle, can be estimated as:

$$gf_{vol}(RH) = 1 + \kappa \frac{RH}{1 - RH} \quad (3.3)$$

where RH is the relative humidity of the air surrounding the droplet and  $\kappa$  is a constant that is determined by the composition of the particle in question.

The dry (crystalline) refractive indices of all three salts studied in this chapter are well known [Tang, 1996] and the resulting wet refractive index can be calculated from the volume mixing rule:

$$n_{wet}(RH) = \frac{(gf_{vol} - 1)n_{H_2O} + n_{dry}}{gf_{vol}} \quad (3.4)$$

where  $n_{H_2O}$  is the refractive index of water,  $n_{dry}$  is the refractive index of the dry salt and  $n_{wet}$  is the refractive index of the solution [Nessler et al., 2005]. Alternative methods for estimating the refractive index of hygroscopic particles exist, but their deviation from the volume mixing rule is less than 1% for solutions that are made up of more than 50% water [Erlick et al., 2011; Schuster et al., 2009].

The refractive indices predicted from equations 3.3 and 3.4 are compared with the corresponding GRASP retrievals in Table 3.1. The ranges of  $\kappa$  values given for sodium chloride and ammonium sulfate are taken from Table 3 of Koehler et al. [2006] and were derived from hygroscopic growth factors in the sub-saturated domain. The  $\kappa$  range used for ammonium nitrate are derived from measurements of CCN at super-saturations less than 1%, and originate from Svenningsson et al. [2006], with the spread representing an uncertainty of one standard deviation. Growth factor derived  $\kappa$  values were not available for ammonium nitrate but the difference between growth

factor and CCN derived  $\kappa$  values is generally small compared to the uncertainty in  $\kappa$  resulting from measurement errors [Petters and Kreidenweis, 2007]. The range in the final predicted wet refractive indices results from the bounds on the  $\kappa$  values, as well as a 2% uncertainty in the RH measurement made inside the PI-Neph.

Table 3.1: Predicted and retrieved real refractive indices, median radii in volume and spherical fractions for the three artificially generated aerosols. Also shown are the deliquescence relative humidities (DRH),  $\kappa$  values, and dry real refractive indices taken from the literature. All refractive indices are at 532nm.

Compound	DRH(%)	Measured RH(%)	$\kappa$	$r_{50}^{GRASP}$ (nm)	$Sphere$ (%)	$n_{dry}$	$n_{wet}^{GRASP}$	$n_{wet}^{\kappa\text{Köhler}}$
<i>NaCl</i>	80	$83.7 \pm 2$	0.91-1.33	144	100	1.544	1.395	1.353-1.372
$(NH_4)_2SO_4$	75	$82.6 \pm 2$	0.33-0.72	120	100	1.530	1.383	1.370-1.414
<i>NH<sub>4</sub>NO<sub>3</sub></i>	62	$83.5 \pm 2$	0.58-0.75	129	54	1.554	1.392	1.371-1.393

Table 3.2: Truncation corrected total scattering ( $\beta_{sca}$ ) from the integrating nephelometer as well as PI-Neph/GRASP retrieved real refractive index, sphere fraction and SSA for the three highlighted case studies. Additionally, the SSA derived from PSAP and integrating nephelometer measurements is shown for comparison. All spectrally dependent parameters are listed at 532nm.

Aerosol Case	Date	Time(UTC)	$\beta_{sca}$	$m_{GRASP}$	$Sphere_{GRASP}$	$SSA_{GRASP}$	$SSA_{PSAP}$
BB Plume #1	Aug 19 <sup>th</sup>	19:06-19:13	$489\text{Mm}^{-1}$	1.594	64.5%	0.976	0.964
BB Plume #2	Aug 27 <sup>th</sup>	21:42-21:48	$95.9\text{Mm}^{-1}$	1.565	91.0%	0.962	0.959
Forested BL	Aug 30 <sup>th</sup>	20:55-21:12	$41.9\text{Mm}^{-1}$	1.566	53.9%	0.908	0.930

The retrieved refractive index values are in good agreement with the range predicted by  $\kappa$ -Köhler theory and the existing literature. Sensitivity studies, performed on ensembles of synthetic data perturbed with modeled PI-Neph noise, suggest one standard deviation uncertainties in retrieved real refractive indices of around 0.02 for non-absorbing particles in the size range of these humidified salts. These studies also showed a general trend of increasing accuracy in the retrieved real part of the refractive index as the median radius of the particles increased. The converse was true for absorption, where more absorbing particles tended to produce more error in the real refractive index inversion. The agreement between the retrieved and predicted refractive index values is consistent with this error analysis.

The retrieved imaginary parts of the refractive index (not shown) of the ammonium nitrate and ammonium sulfate solutions were both found to be on the order of  $10^{-3}$ . These values are indicative of moderate absorption but are larger than more established values found in the existing literature, which suggests very little absorption ( $k < 10^{-7}$ ) for all three of the solutions measured [Fenn et al., 1985; Toon and Pollack, 1976; Hale and Querry, 1973]. An even higher imaginary part of the refractive index ( $k = 0.026$ ) was retrieved in the case of the sodium chloride sample. The magnitude of this value may be, at least in part, related to an unrealistically high retrieved real refractive index. This hypothesis is supported by the fact that constraining the retrieved real refractive index to the range predicted by the sample RH and  $\kappa$ -Köhler theory resulted in significantly lower retrieved values of sodium chloride absorption. A comparison was also made between the retrieved single-scattering albedo and the SSA derived from Particle Soot/Absorption Photometer (PSAP, Radiance Research, Seattle, WA, USA) and integrated scattering measurements (Integrating Nephelometer 3563, TSI Inc., St. Paul, MN, USA) in SEAC<sup>4</sup>RS. A statistically significant correlation between the two data sets was determined to exist, but the retrieved SSA

was also found to systemically overestimate the measured absorption. Notice that the retrieval was based only on scattering measurements (no absorption or extinction data was included) and therefore is expected to show limited sensitivity to these variables. A detailed analysis of the sensitivity of the GRASP/PI-Neph retrieval to absorption is beyond the scope of this work.

After passing their deliquescence point, crystalline salt particles should transform into saline droplets and become spherical in shape. The GRASP/PI-Neph inversion was able to accurately reproduce this spherical morphology in the sodium chloride and ammonium sulfate case, but a spherical fraction of only 54% was retrieved for the ammonium nitrate sample. This deviation from expectation is likely driven by a combination of random error in the PI-Neph measurement and the fact that the scattering of non-spherical particles tends to deviate less from that of spherical particles as particle size decreases. This notion is confirmed in the sensitivity studies previously described, where it was found that there was very little sensitivity to sphericity in the case of small particles ( $r < 200\text{nm}$ ).

Retrievals of the monodisperse PSL spheres produced real refractive index values that were within the range of existing measurements available in the literature at all three wavelengths [Bateman et al., 1959; Ma et al., 2003; Sultanova et al., 2003; Jones et al., 2013]. The spectral dependence of the retrieved values, as well as the three most recently reported Cauchy Equation parameterizations of PSL refractive index can be found in Figure 3.8. The retrieved imaginary part of the refractive index for these spheres was on the order of  $10^{-3}$  for all three wavelengths, slightly higher than the values of around  $4 \times 10^{-4}$  that have been reported by more sensitive techniques[Bateman et al., 1959; Ma et al., 2003].

Figure 3.9 shows the spectrally dependent distribution of the retrieved dry refractive indices for the 50 chosen SEAC<sup>4</sup>RS cases. The mean retrieved real part of the

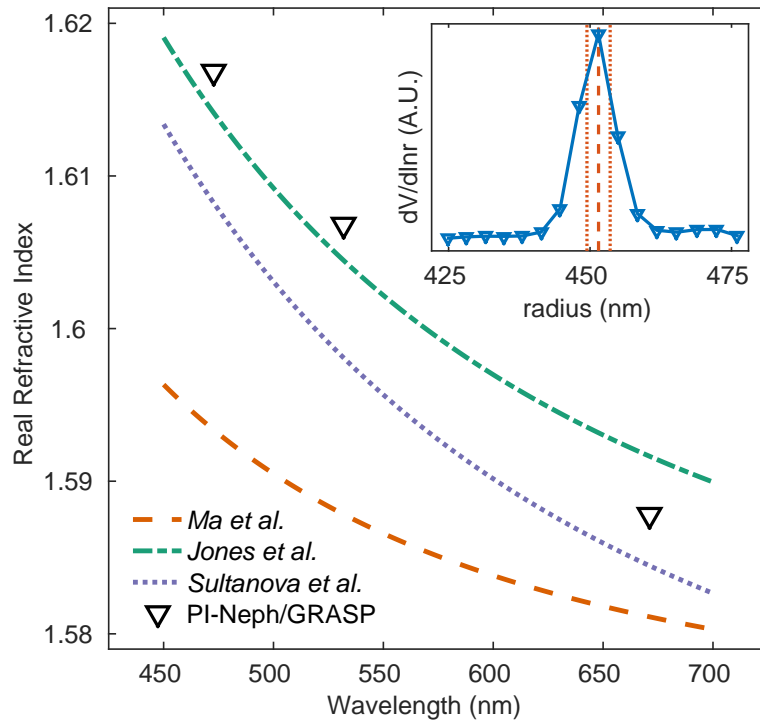


Figure 3.8: Retrieved real part of the refractive index for PSL spheres, alongside three previous, modern measurements of polystyrene refractive indices [Ma et al., 2003; Jones et al., 2013; Sultanova et al., 2003]. The subplot shows the retrieved size distribution (blue) along side the manufacturer's specified central radius (red dashes) and FW67 (red dots).

refractive index at 532nm for the 50 cases, composed primarily of biomass burning and urban-biogenic mixtures, was found to be 1.53. This figure is in line with the existing measurements made under similar conditions [Shingler et al., 2016], but unfortunately very few airborne, in situ measurements of refractive index are available. Remote sensing retrievals of biomass burning aerosol generally range from 1.47 to 1.55 [Dubovik et al., 2002; Li and Mao, 1990; Westphal and Toon, 1991; Yamasoe et al., 1998], while remote retrievals of urban pollution have generally yielded somewhat lower values, ranging from 1.39 to 1.46 [Dubovik et al., 2002; Redemann et al., 2000]. These lower values observed in the urban pollution remote sensing retrievals are likely driven in large part by particle hygroscopicity. The PI-Neph/GRASP retrievals of real refractive index are expected to be significantly higher in analogous cases as the PI-Neph measurements were made at very low relative humidities, where hygroscopic growth is virtually non-existent. In spite of these differences in measurement conditions, as well as in the sample regions in question, the values are remarkably similar, especially in the case of biomass burning emissions, which are expected to have limited hygroscopicity. Additionally, the spectral dependence is in line with expectation, and closely matches measurements of common natural aerosol constituents made by Hale and Querry [1973].

Table 3.2 shows details of the retrievals performed on the three cases studied. The retrieved real refractive index of the August 19<sup>th</sup> biomass burning plume is slightly higher than the values reported in the literature, and represents the upper end of the values retrieved in the 50 selected samples. The other two cases also returned higher than average values, although they were more in line with the other samples and typical values reported in the existing literature. The biomass burning particles were also found to be less absorbing than that of typical smoke, but the values produced by GRASP are in good agreement with direct SSA measurements

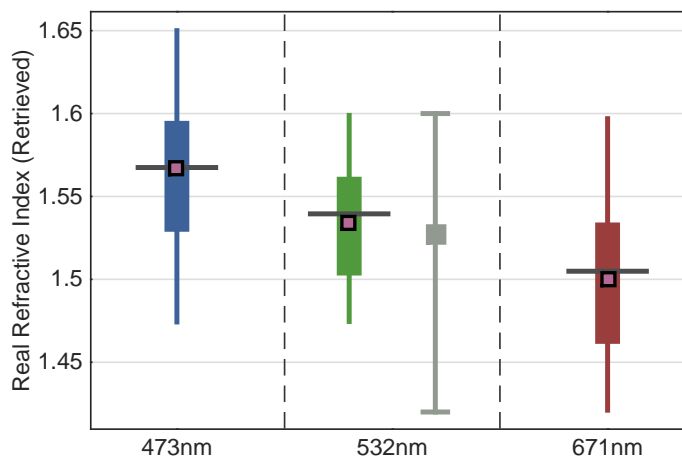


Figure 3.9: Retrieved refractive index at all three PI-Neph wavelengths for the 50 selected SEAC<sup>4</sup>RS samples. Box and whiskers plots show the data distribution by quartile while the connected black squares show the spectral dependence of the mean. The gray bounds at 532nm denote the minimum and maximum values measured by Shingler et al. [2016] in SEAC<sup>4</sup>RS while the grey square denotes the corresponding mean.

aboard the DC-8 derived from PSAP and integrating nephelometer measurements [SEAC4RS, 2013]. A significant percentage of particles were determined to be non-spherical in these cases, especially the August 19<sup>th</sup> biomass burning plume and August 30<sup>th</sup> forested boundary layer aerosols. The cases on August 19<sup>th</sup> and August 27<sup>th</sup> are dominated by small particles, and in turn there are large uncertainties in the sphericity product. The low sphericity percentage retrieved for the August 30<sup>th</sup> case is potentially realistic given the significance of the coarse mode, but additional independent measurements of sphericity are limited.

### 3.3.3 Size Distribution Retrievals

The size distribution retrieved for the PSL spheres is shown in the sub-panel of Figure 3.8 and agrees well with the manufacturer’s specifications. The median diameter

of the retrieved distribution was found to be 902.7nm which shows excellent agreement with the manufacturer’s NIST (National Institute of Standards and Technology) traceable specification of 903nm±12. It is the authors’ experience, based on PI-Neph measurement inversions on a range of PSL products from the same manufacturer, that the uncertainty listed often significantly overestimates the true uncertainty in the central diameter of the size distribution. As discussed in Section 3.3.1, the retrieval returned a distribution width that was approximately twice the value specified by the manufacturer but features in the  $-F_{12}/F_{11}$  measurement indicate that the true width is more likely inline with the manufacturer’s specification FW67 of 8.2nm. Similarly accurate results sizing PSL spheres with PI-Neph data are demonstrated in Dolgos and Martins [2014] through the use of a Mie theory lookup table.

The retrieved size distributions for all three SEAC<sup>4</sup>RS case studies are plotted alongside measurements made by dedicated particle sizers in Figure 3.10. The APS data was converted from aerodynamic to geometric size using an assumed density of 1.3gcm<sup>-3</sup> and a shape factor of unity. Uncertainties in these assumption can generate significant changes in the resulting geometric PSD, but the presence of APS data can still be used as an optically independent, qualitative confirmation regarding the presence of significant coarse mode. The UHSAS data is shown for two different calibration aerosols, PSL spheres and ammonium sulfate, which have real refractive indices of 1.61 [Jones et al., 2013] and 1.53 [Tang, 1996] respectively. The LAS data shown corresponds to calibration with PSL spheres.

In all three of these cases the peak of the fine mode generally occurs around a radius of 150nm. These values are typical of the majority of the 50 selected periods, all of which have fine mode median radii (in volume) between 100nm and 200nm. The PI-Neph/GRASP PSD retrievals fall between the two different UHSAS calibrations in each of the three cases, which again is typical of almost all 50 samples.

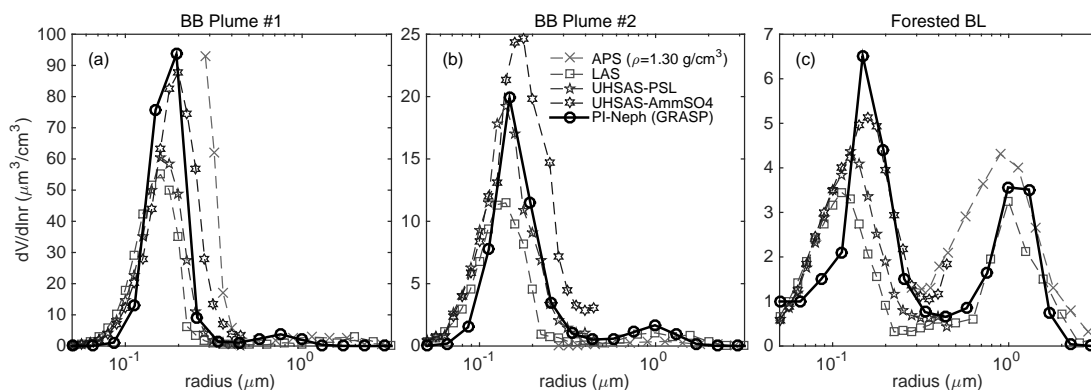


Figure 3.10: Direct comparisons of PI-Neph/GRASP retrieved size distributions with dedicated particle sizers that sampled in parallel to the PI-Neph. The three cases selected show measurements from the (a) August 19<sup>th</sup> and (b) August 27<sup>th</sup> biomass burning cases, as well as (c) boundary layer measurements made above a forested region of southeast Missouri on August 30<sup>th</sup>.

Among the 50 selected periods for which size distribution comparisons were made, only two cases had coarse modes with volume concentrations that made up a significant portion of the total particle volume. The first of these cases, a sample dominated by transported Saharan dust, had very low aerosol loading and the bulk of the scattering matrix data at scattering angles above  $40^\circ$  was below the PI-Neph's limit of detection. The second of these cases, the forested boundary layer measurements taken on August 30<sup>th</sup>, was therefore chosen as one of the three highlighted case studies. In both cases the size distributions agree remarkably well in the coarse mode, suggesting significant sensitivity to larger particles in the retrieved product. This sensitivity likely resulted primarily from the PI-Neph's ability to measure down to scattering angles as low as  $3^\circ$  during SEAC<sup>4</sup>RS. Lienert et al. [2003] was also able to show sensitivity to super-micron particles given a minimum scattering angle of around  $2^\circ$ . On the other hand, Sviridenkov et al. [2014] determined that single scattering measurements over a scattering angle range of  $10^\circ$  to  $90^\circ$ , were insufficient to provide significant information about the coarse mode. All of these conclusions are in

agreement with theoretical sensitivity studies indicating that measurements at very low scattering angles are required if the coarse mode is to be accurately recovered [Dubovik et al., 2000].

In order to simplify the comparison of the retrieved size distributions with those measured by the dedicated aerosol spectrometers, the fine mode of each PSD was parameterized according to three metrics: total volume concentration, median radius and the span of the distribution. When determining these metrics the values of the volume distributions corresponding to radii less than 50nm were first removed, as this lower bound corresponds to the bottom of the PI-Neph/GRASP retrieval range. The upper end of the remaining size distribution was then further truncated to include only fine mode particles. The division between the fine and coarse modes was defined as the minimum value of the LAS volume distribution, closest to  $r=300\text{nm}$ . A visual inspection of all cases confirmed that this metric was sufficient to reasonably isolate the fine mode when two modes were present. The volume concentration, median ( $r_{50}$ ) and span ( $(r_{90} - r_{10})/r_{50}$ ) were then calculated using these final truncated volume distributions. Linear interpolation was used when the 10<sup>th</sup>, 50<sup>th</sup> or 90<sup>th</sup> percentile values, as well as the bounds of the truncated distributions, fell between the midpoints of two size bins. Scatter plots showing the results of these parameterizations for the three OPC measurements vs the corresponding PI-Neph retrieval are shown in Figure 3.11.

The PI-Neph retrieved volume concentrations and median radii generally fall somewhere between the two different UHSAS calibrations, with the best agreement generally tending towards the ammonium sulfate calibration. This is consistent with the average retrieved refractive index for the 50 cases ( $n=1.53$ ) which is in very close agreement to the dry refractive index of ammonium sulfate found in the literature. The LAS consistently measured smaller and fewer particles than all the other siz-

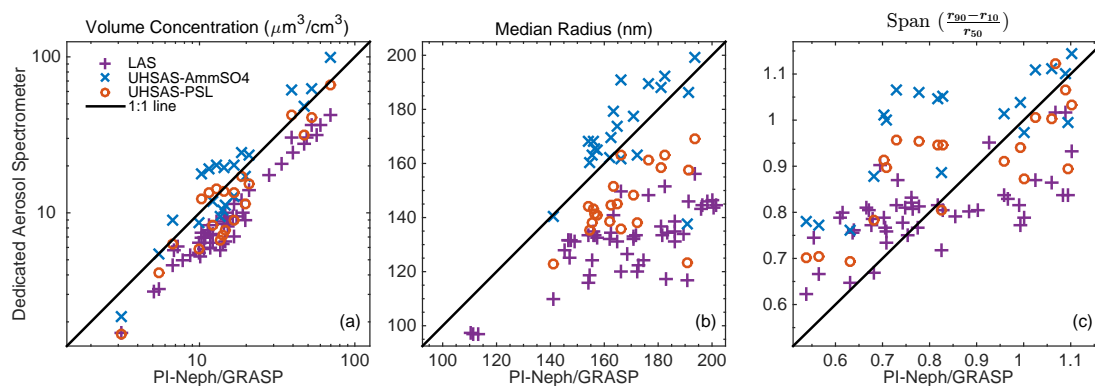


Figure 3.11: Scatter plot comparisons of retrieved size distributions with particle sizers sampling in parallel to the PI-Neph. In order from left to right the panels show total fine mode (a) volume concentration, (b) volume median radius and (c)  $span = \frac{r_{90}-r_{10}}{r_{50}}$ . The value retrieved from PI-Neph measurements is plotted on the horizontal axis while the value measured by the corresponding dedicated aerosol spectrometer is plotted along the vertical axis. The comparisons are made against LAS measurements (purple pluses), UHSAS ammonium-sulfate equivalent optical diameters (blue crosses) and UHSAS PSL equivalent optical diameters (red circles).

ing techniques, but still showed significant correlation with the PI-Neph/GRASP retrievals. There was weaker agreement regarding the width of the distribution among the four techniques. The retrieved spans generally best matched the corresponding PSL calibrated UHSAS values, but the values covered a larger range of spans than the values measured by the OPCs. The PI-Neph retrieved spans fell between 0.55 and 1.03 in 95% of the cases. In contrast, the LAS showed the least variability in span, with 95% of the values falling between 0.65 and 0.85. The differences in span between PI-Neph retrievals and the OPCs was likely driven in large part by their different sampling techniques (ensemble vs single particle measurements).

The large differences between UHSAS measurements under different calibrations, with disparate refractive indices, demonstrates the significance of the refractive index assumptions required. The results of this work, as well as others [Shingler et al., 2016], suggest that the real refractive indices of natural aerosol can frequently

reach values as low as 1.48 at 532nm. This is substantially lower than the refractive index of ammonium sulfate ( $n = 1.53$ ), which has the lowest value of the aerosols that are commonly used to calibrate optical particle sizers, and further emphasizes the significance of the basis resulting from uncertainty in refractive indices.

In order to further assess the retrieval variability, resulting from changes in refractive index and sphericity, the 50 SEAC<sup>4</sup>RS cases were inverted a second time with assumptions corresponding to PSL spheres. In this analysis the complex refractive index was forced match measurements of PSL and non-spherical particles were excluded from GRASP's aerosol model. This configuration produced significantly better agreement with the PSL calibrated UHSAS measurements in volume concentration, median radius and span, when compared to the unconstrained retrievals. This result further demonstrates that differences in fundamental assumptions about the optical and morphological properties of the particles are driving a significant portion of the differences between the retrieved and measured values. The ability of GRASP to retrieve (as opposed to assume) these optical and morphological parameters suggests that the corresponding retrieved size distribution may be more representative of the actual sample than the corresponding OPC measurements.

## CHAPTER 4

# Airborne in situ characterization of aerosols over the contiguous United States

This chapter is an adaptation of original work that is currently under review in the journal *Atmospheric Chemistry and Physics*.

### 4.1 Introduction

In comparison with instruments like AERONET, the viewing angles sampled by most space based remote sensors produces significantly less information content. This challenge, along with the need to correct for surface reflectance, means that inversions designed to retrieve aerosol properties from space must make significant assumptions about the aerosol in question. These assumptions frequently take the form of a set

of aerosol types (ex. desert dust, biomass burning, urban emissions, etc.) with pre-defined characteristics. These preassigned characteristics, termed 'aerosol models' include particle size distribution, complex refractive index and particle morphology. While current algorithms are adequate to retrieve AOD and a few other parameters, the results from a wide range studies have suggested that there may still be room for significant improvements in the aerosol models used in space-based remote sensing retrievals. For example, localized tests using modified, more locally appropriate aerosol models have shown significant improvements in comparisons with AERONET derived AOD as well as the ability to increase spatial resolution with little cost to retrieval accuracy [Bilal et al., 2013; Lee et al., 2012; Wong et al., 2011].

Models used to calculate aerosol forcing and to estimate climate change also rely on assumptions of aerosol properties. In fact, comparison of nine widely used aerosol forcing models found that the greatest diversity in model estimates of forcing were not in the representation of aerosol loading by the models, but in the forcing efficiency, the forcing per unit of loading [Schulz et al., 2006]. The forcing efficiency is affected by wide-ranging values of aerosol absorption and size distribution, as well as surface albedo found in the models [Schulz et al., 2006]. A revisit of this model comparison, now involving 16 models, published seven years later found no narrowing of model diversity in estimates of aerosol radiative effects and forcing, and significant diversity when analyzed individual aerosol components [Myhre et al., 2013]. Again, the reason was traced to significant range of values for factors such as forcing efficiency that stem from lack of constraints in basic aerosol intrinsic properties [Myhre et al., 2013].

The aerosol characteristics used in passive remote sensing algorithms and climate modeling mostly have been based on inversions of AERONET sky radiance measurements, producing values of total column ambient aerosol optical properties

[Dubovik et al., 2000]. Constructing aerosol models from these inversion data requires calculating statistics of the quantities for different groupings of the data corresponding to different aerosol types or classifications. Classifications can be identified using a priori knowledge of dominant aerosol types in different locations [Remer et al., 1997; Remer and Kaufman, 1998; Dubovik et al., 2002; Giles et al., 2012], or by using advanced statistical methods such as cluster analysis [Omar et al., 2005; Levy et al., 2007; Wu and Zeng, 2014], recently utilizing Mahalanobis distances [Russell et al., 2014; Hamill et al., 2016]. These techniques have also been applied to other high-quality aerosol remote sensing data sets such as High Spectral Resolution Lidar (HSRL) or Multiangle Imaging SpectroRadiometer (MISR) to classify aerosol into dominant types and to derive aerosol models for each type [Burton et al., 2012; Kahn and Gaitley, 2015]. The advantage of using remote sensing data sets to construct aerosol models for remote sensing or climate applications is to have a set of aerosol models producing a radiance at the top of the atmosphere consistent with the radiance a satellite would measure or that affects the planetary energy balance. The disadvantage of using such data sets to construct aerosol models is that detailed particle information is lost due to ambiguities concerning humidification and height of the particles, and such models cannot be easily linked to particle composition.

In-situ airborne measurements of aerosols commonly include data on particle concentration and size, integrated extinction, absorption and scattering as well as information regarding chemical composition. Another parameter frequently measured in situ from aboard an aircraft is the aerosol refractive index. Recent advances in measurement technology have improved the accuracy of these measurements significantly [Espinosa et al., 2017; Shingler et al., 2016], but their availability remains limited to a minority of field campaigns. One of the earliest airborne investigations of aerosol refractive index was performed over four decades ago by inverting angular

light scattering intensities obtained with a polar nephelometer [Grams et al., 1975]. As noted in Section 1.3.4, airborne polar nephelometer measurements have remained infrequent but Shcherbakov et al. [2016] combined these measurements with principal component analysis to explore the properties of coarse mode aerosols found in volcanic degassing plumes.

The work presented in this chapter constitutes the first comprehensive analysis of angular dependent light scattering measurements made in situ from aboard an aircraft on common atmospheric aerosols. The analysis focuses on measurements made during the SEAC<sup>4</sup>RS and DC3 field campaigns. The light scattering data include both phase function ( $F_{11}$ ) and polarized phase function ( $-F_{12}/F_{11}$ ) measurements made by the Polarized Imaging Nephelometer (PI-Neph) [Dolgos and Martins, 2014]. These measurements are separated into 2390 different averaging periods for which stable, high quality data were available. A classification strategy was then developed for the SEAC<sup>4</sup>RS data to identify the dominate aerosol type for each case, making use of trace gas measurements, aerodynamic size distributions and aerosol composition measurements. The data from the DC3 campaign, which has significantly different objectives from SEAC<sup>4</sup>RS, was classified according to the region where the convective system was observed. Principal component analysis was then applied to the PI-Neph data to confirm the validity of the classification scheme in a light scattering context. Finally, in Section 4.6, the GRASP algorithm is applied to the light scattering data to obtain average particle size distributions (PSD), real refractive indices and fraction of spherical particles for each air mass type.

## 4.2 Methodology

The dataset used in this chapter is built from measurements made aboard the DC-8 aircraft during the DC3 and SEAC<sup>4</sup>RS field campaigns, with a focus on measurements made by the PI-Neph airborne polar nephelometer. Time averages are performed on the raw PI-Neph data and the resulting cases are grouped into one of eight predefined aerosol categories according to a novel aerosol classification scheme. This classification scheme makes use of measurements that are independent of aerosol light scattering, including particle composition, aerodynamic size distribution and gas concentrations. This section concludes with a detailed discussion of the application of the GRASP inversion algorithm to PI-Neph data.

### 4.2.1 Instrumentation

PI-Neph measurements and the corresponding retrievals will serve as the primary data source for the analysis presented in this chapter. In DC3 the PI-Neph utilized only one laser operating at 532nm, but two additional lasers were incorporated into the instrument prior to SEAC<sup>4</sup>RS, adding measurements at 473nm and 671nm. The angular range of the instrument was typically 4° to 174° in SEAC<sup>4</sup>RS, and 5° to 170° in DC3. The raw sampling rate of the measurement was 45 seconds in SEAC<sup>4</sup>RS and 11 seconds in DC3 but all data shown in this chapter are averages composed of multiple raw measurements. The incorporation of the two additional measurement wavelengths gives rise to the longer PI-Neph sampling time in SEAC<sup>4</sup>RS.

In this study the Particle Analysis by Laser Mass Spectrometry (PALMS) instrument was used to aid in the identification of aerosols containing significant amounts of mineral dust. PALMS uses a strong ultra-violet laser pulse to ablate

particles, the ionized fragments of which are then passed through a time-of-flight mass spectrometer [Thomson et al., 2000]. The quantity of alumina and aluminosilicates is then used to identify mineral dust particles [Lee et al., 2002] and the fraction of these particles is reported over five-minute intervals. In this work, dust aerosols are also classified using information regarding aerodynamic particle size. An aerodynamic particle sizer (APS model 3321, TSI Inc., St. Paul, MN, USA), measuring particle time-of-flight inside an accelerating air flow, was used to obtain these measurements. APS measurements were made at ambient humidities during SEAC<sup>4</sup>RS and the results were reported in 14 log spaced bins with midpoint diameters ranging from 563nm to 6.31 $\mu$ m. Additionally, dry size distributions obtained by a Scanning Mobility Particle Sizer (SMPS, TSI Inc., St. Paul, MN, USA) are used to quantify the influence of small particles, below the size range of the GRASP retrieval.

Trace gas concentrations are used to identify air masses corresponding to urban, biogenic and biomass burning emissions. Carbon monoxide volume mixing ratios were obtained with the Differential Absorption Carbon Monoxide Monitor (DACOM; Fried et al. [2008]). Measurements of nitrogen dioxide (NO<sub>2</sub>) were made by the National Oceanic and Atmospheric Administration's (NOAA) NO<sub>y</sub>O<sub>3</sub> instrument using the UV-LED photolysis-chemiluminescence technique [Pollack et al., 2010; Ryerson et al., 2000]. The University of Innsbruck's High-Temperature Proton-Transfer-Reaction Mass Spectrometer (HT-PTR-MS; Mikoviny et al. [2010]) was used to quantify the mixing ratio of the remaining gas species, specifically acetonitrile (CH<sub>3</sub>CN), isoprene (C<sub>5</sub>H<sub>8</sub>) and monoterpenes (C<sub>10</sub>H<sub>16</sub>).

### 4.2.2 Averaging of PI-Neph Measurements

The PI-Neph made more than ten thousand raw measurements over 163 flight hours during the SEAC<sup>4</sup>RS campaign and almost forty thousand raw measurements over 116 hours during DC3. A significant fraction of these measurements occurred at very low aerosol concentrations, typically during high altitude transit legs of the flights, when noise can overwhelm the scattering signal. Additionally, examination of the measurement data showed that, while the aerosol concentrations often varied quite quickly, the values of  $\tilde{F}_{11}$  and  $-F_{12}/F_{11}$  were generally stable over much longer periods. These facts motivated the decision to perform averages on the raw PI-Neph data over periods corresponding to several measurements.

The averaging scheme was designed to both reduce random noise as well as eliminate periods of very low scattering where systematic (i.e. temporally correlated) sources of error are significant. Only raw PI-Neph measurements corresponding to high aerosol concentrations and relatively stable optical properties were included in the averaging scheme. Specifically, only measurement periods where the total scattering was consistently above  $10Mm^{-1}$  and the change in integrated scattering between two adjacent raw measurements was less than 15% were considered. If insufficient or unstable scattering led to the removal of a raw data point the relevant average was discarded and a new potential averaging window was started (i.e. all averages are composed of consecutive data points). An averaging period was concluded when at least three raw measurements were included and the sum integrated scattering values of each individual data point summed to greater than  $200Mm^{-1}$ . The averaging periods were derived from the 532nm SEAC<sup>4</sup>RS products to maximize consistency in the averaging procedure between the two campaigns.

The process described above resulted in 573 averages in SEAC<sup>4</sup>RS and 1817

averages from DC3. The mean average time in SEAC<sup>4</sup>RS was 152 seconds while the mean averaging time during DC3 was 67.6 seconds. 93% SEAC<sup>4</sup>RS and 67% of the DC3 averages were made on 5 raw data points or less. The smaller quantity of cases (and longer mean averaging times) in the case of SEAC<sup>4</sup>RS is primarily due to the reduced time resolution associated with the three-wavelength measurement.

### 4.3 Aerosol Classification Scheme

An aerosol classification scheme was developed to estimate the dominate source of each aerosol by focusing on the air mass associated with each PI-Neph average, using ancillary data that include measurements of gases, aerosol composition and physical properties as well as aircraft location. Aerosol optical properties were intentionally omitted from all classification metrics to ensure independence between the classification scheme and the scattering features measured by the PI-Neph. As convective systems have the potential to significantly influence aerosol properties [Jeong and Li, 2010; Eck et al., 2014; Corr et al., 2016] different classification schemes were applied to the DC3 dataset (near convective systems) and the SEAC<sup>4</sup>RS data set (generally far from convective systems). The SEAC<sup>4</sup>RS data was subdivided into five categories corresponding to dust, biogenic, urban, biomass burning (BB) emissions and unclassified samples. This classification utilized measurements of particle chemical composition from the PALMS instrument, the aerodynamic size distribution of particles generally associated with the coarse mode and a range of trace gases. The scheme developed to categorize the DC3 data was based on aircraft location relative to three storm domains outlined in the DC3 science objectives [Barth et al., 2015] as well as the presence of convective systems over the course of the corresponding flight. Both the DC3 and SEAC<sup>4</sup>RS classification schemes only allow one aerosol type to be

assigned to a given PI-Neph sample.

The SEAC<sup>4</sup>RS dust classification requires that the PALMS instrument identify at least 15% of the measured particles as mineral dust. It was found that the PALMS algorithm would often classify a significant fraction of particles as mineral dust, even when PSD measurements showed no significant coarse mode. In order to exclude these cases and align our dust classification with more traditional dust aerosol we imposed a set of requirements on the coarse mode of the aerodynamic size distributions. Specifically, the volume concentration measured by the APS (which is insensitive to particles below 500nm) must exceed  $2\mu\text{m}^3/\text{cm}^3$  and have an effective radius greater than 750nm. This constraint on the aerodynamic PSD removed several cases where no obvious source of dust could be identified.

If the dust category was not selected gas tracers and aircraft altitude were used to screen for the remaining three fine mode dominated types. Shingler et al. [2016] used a threshold of 250pptv acetonitrile—or 250pptb of carbon monoxide if acetonitrile data is unavailable—as an indicator of BB emissions. We have modified this metric to also include cases with acetonitrile values as low as 190 pptv but only if the sum of the volume mixing ratios of isoprene and monoterpenes is less than 40% that of acetonitrile. Since isoprene and monoterpenes are well correlated with biogenic emissions this condition permits the inclusion of cases with lower BB concentrations, while still avoiding false positives that can potentially be triggered by strong biogenic emissions of acetonitrile. Accordingly, isoprene and monoterpenes are used as gas tracers for the biogenic category, with a biogenic classification occurring when their combined concentrations exceed 2ppbv. When the previous three categories are not triggered, the aircraft is within or close to the mixing layer (altitude below 3km) and NO<sub>2</sub> concentrations are greater than 1ppbv the urban category is selected. A marine aerosol classification occurring whenever the aircraft was directly above large bodies of

water was also examined, but the scattering intensity during almost all corresponding periods was below the PI-Neph’s lower limit of detection. The few remaining marine cases, as well as all cases that failed to trigger any other classification, are identified as “unclassified”. A decision tree specifying the requirements for each SEAC<sup>4</sup>RS category is shown in Figure 4.1.

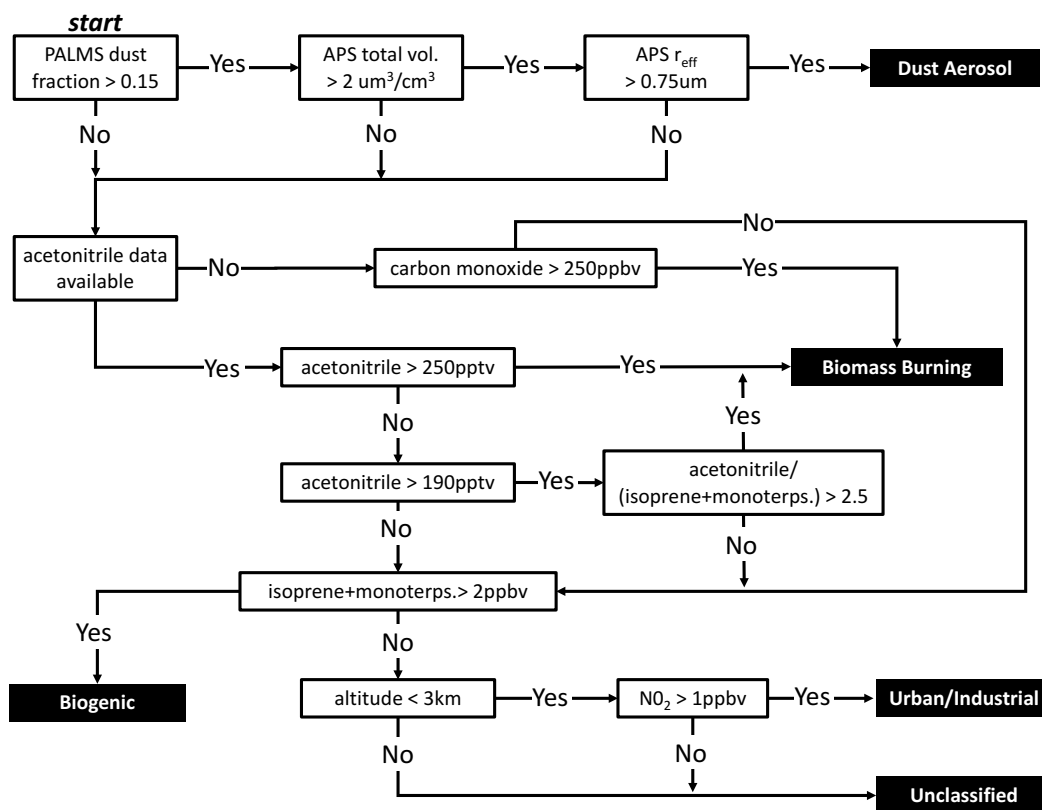


Figure 4.1: The decision tree used to classify aerosol types in SEAC<sup>4</sup>RS.

The DC3 campaign had significantly different objectives—namely the study of convective systems—and correspondingly the SEAC<sup>4</sup>RS classification algorithm does not map well to the DC3 dataset. This fact motivated the decision to classify DC3 sample by study region (CO, AL or TX/OK) as opposed to gas and composition data. A PI-Neph sample was associated with a given study region if the aircraft coordinates were within the corresponding domain and the corresponding flight path

was designed to target active storms in the region. Additionally, in order to restrict the assigned cases to storm inflow measurements, the classification was only applied if the observation was made below 6km. This constraint produced much more homogeneous aerosol properties for each storm domain by eliminating the cases with highly variable scattering properties found in the higher altitude outflow aerosols.

Table 4.1 shows the number of cases assigned to each category, as well as the number of unique flights containing at least one of the corresponding cases. 70% of the SEAC<sup>4</sup>RS cases received a classification (other than 'unclassified') while 55% of the DC3 cases were classified. In both campaigns, the majority of the unclassified cases correspond to high altitude transit legs that are generally associated with relatively clean air masses. All categories have cases originating from multiple flight days, increasing the likelihood that a given category average is representative of the typical aerosol properties found in that type. The last column of this table provides statistics regarding the  $F_{11}$  residuals of the GRASP fit for each type and will be further discussed in Section 4.6.

Table 4.1: The total number of cases, the number of unique flights for which at least one case was present and the percent of cases for which the residual between the GRASP fit and the measured  $F_{11}(\theta)$  values was less than 12%.

Aerosol Type	# of cases	# of flights	$RES < \%12$
BB	105	8	94.3 %
Biogenic	252	11	86.5 %
Urban	28	7	85.7 %
Dust	15	2	0.00 %
CO Storms	329	4	60.5 %
TX/OK Storms	535	5	96.8 %
AL Storms	140	2	99.2 %
Unclassified	986	17	52.3 %
All Cases	2390	37	75.9 %

Figure 4.2 shows the geographic locations of all classified PI-Neph samples.

The extent of the three DC3 study regions can be seen in the spread of the red, beige and maroon circles corresponding to the CO, TX/OK and AL storms categories, respectively. In the summer months, biogenic emissions often dominate the southeastern United States (SEUS) while the western portion of the country is frequently influenced by wildfire smoke. While the SEAC<sup>4</sup>RS categories are not determined by location, clear patterns emerge that are in strong agreement with these physical expectations.

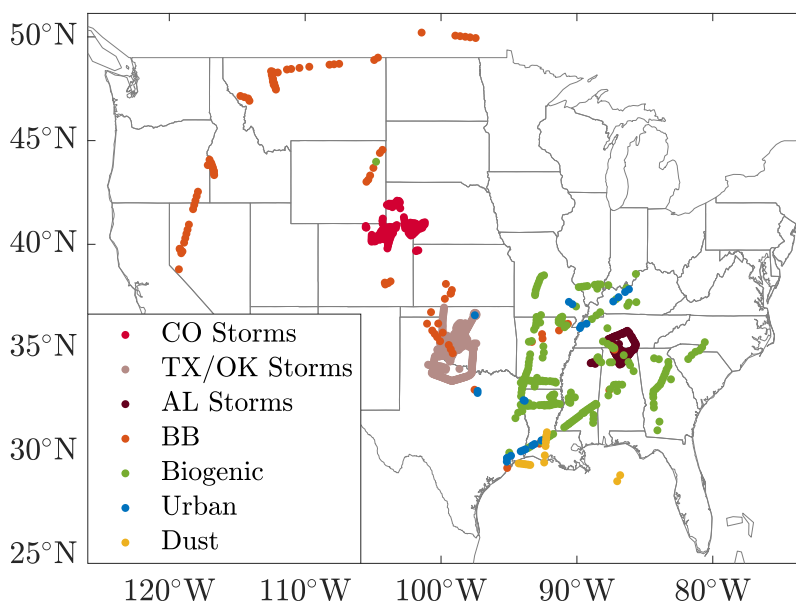


Figure 4.2: The results of the air mass classification scheme as a function of geographic location for DC3 and SEAC<sup>4</sup>RS.

The California Rim Fire was one of the dominant sources of biomass burning emissions during the SEAC<sup>4</sup>RS deployment. The fire began on August 17<sup>th</sup> in Stanislaus National Forest, California and continued to burn until after the end of the SEAC<sup>4</sup>RS deployment [Saide et al., 2015]. Before the fire was fully extinguished its total burn area had grown to 104,000 ha, making it the third largest fire in California’s history [Peterson et al., 2015]. The arch of biomass burning cases that is

shown in the northwestern portion of Figure 4.2 and traverses from California into southern Canada represents samples dominated by Rim Fire smoke. Emissions from this fire made up 58% of all classified BB cases. The overwhelming majority of the remaining cases came from smaller wildfires within the United States, primarily from three fires located in Wyoming, Colorado and Kansas [Toon et al., 2016]. While many agricultural fires were sampled in SEAC<sup>4</sup>RS these measurements were almost always discarded by the averaging algorithm described in Section 4.2.2 due to the very short duration, and high variability, of the corresponding measurement.

The 15 points that met the requirements of the dust classification are shown in yellow in Figure 4.2. This type was only observed in early August over Louisiana and the northern Gulf of Mexico. These cases likely correspond to a transported Saharan Air Layer (SAL) that was present over this region at the start of the campaign. There is strong evidence, based on aerosol concentration and composition, that this air mass was relatively pristine and had not mixed significantly with continental air [Ziemba et al., 2016].

In August and September biogenic emissions are ubiquitous in the south eastern United States. The classification scheme shown here conveyed this fact well, with most of these cases in this region falling under the biogenic category. The second most prevalent category over the SEUS is the urban type. This classification corresponds well to city centers like Houston and Dallas Texas, whose emissions were frequently sampled by the DC-8. Additionally, a large strip of urban cases can be seen around the Ohio River Valley, an area with a very high concentration of fossil fuel based power plants. It is shown in Section 4.5 that the optical properties of aerosols associated with cities are quite different from the industrial emissions of the Ohio River Valley. The possibility of dividing the urban category into two sub-groups was explored, but the already limited number of cases made this division impractical.

It is likely that other datasets, with a larger number of samples corresponding to urban and industrial emissions, can be more easily understood by dividing the urban classification described here into two separated sub-categories that are separated by  $\text{SO}_2$  concentrations, for example.

#### 4.4 Measurement of Phase Matrix Elements

A robust averaging procedure was applied to all sample averages of  $\tilde{F}_{11}$  and  $-F_{12}/F_{11}$  data of a given aerosol type to obtain curves that are typical of each category. Figure 4.3 shows the results of this averaging for all three DC3 storm domains as well as the dust category and the average of all three fine mode dominated aerosols (biogenic, urban and BB) from SEAC<sup>4</sup>RS.

A progression in both  $\tilde{F}_{11}$  and  $-F_{12}/F_{11}$  averages is evident as the DC3 storm domain transitions from AL to TX/OK to CO. The increase in forward scattering peak through this sequence suggests an increased scattering contribution from particles in the larger size ranges that direct the bulk of their scattered energy into the forward angles. Models have shown that large convective systems can agitate surface dust, drawing these particles up into the atmosphere and acting as a significant source of dust aerosol [Seigel and van den Heever, 2012; Takemi et al., 2006]. The elevated forward scattering peaks are likely driven by increasingly arid surface features, leading to an increased availability of this relatively large dust aerosol [Tulet et al., 2010]. Variations in typical storm wind speeds may have also contributed to variations in the quantity of dust that was suspended over a given region.

The same progression is evident in the backscattering angles of the DC3 storm categories, with CO having the strongest backscattering intensities, followed by TX/OK and then AL. In the relevant size and refractive index regimes this region of the phase

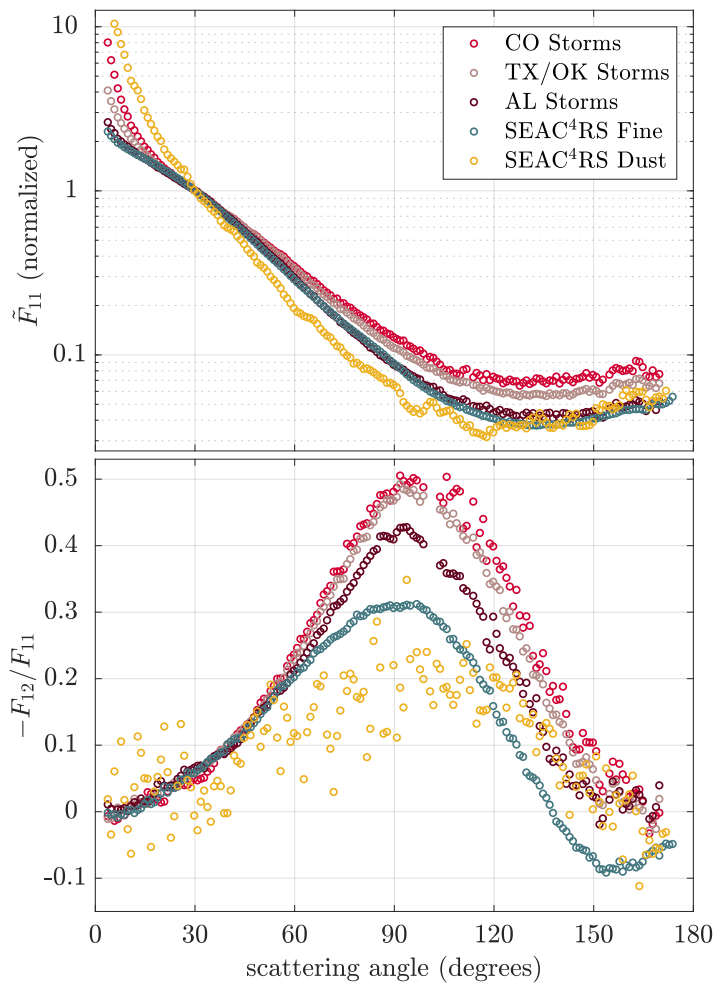


Figure 4.3: Average  $\tilde{F}_{11}$  and  $-F_{12}/F_{11}$  data for all three DC3 storm domains as well as dust and fine mode aerosols (biogenic, urban and BB) from SEAC<sup>4</sup>RS.

function is very sensitive to the diameter of the fine mode particles, suggesting significantly smaller fine mode particles in the CO inflow than in AL. A fine mode peak shifted toward smaller diameters also produces larger values of  $-F_{12}/F_{11}$  at side scattering angles, although this effect is partially moderated by differences in refractive index (see Section 4.6.2).

The average  $\tilde{F}_{11}$  data, corresponding to the SEAC<sup>4</sup>RS fine mode dominated categories, shows very weak forward scattering which is inline with the expectation of relatively few coarse mode particles. The low peak value of  $-F_{12}/F_{11}$  observed in this fine mode dominated data is likely driven primarily by fine mode particles with slightly larger diameters than those found in the three DC3 categories. The features of the dust scattering matrix elements, specifically the presence of an extremely strong forward scattering peak, are typical of an aerosol whose scattering properties are dominated by coarse mode particles. While the typical integrating scattering intensity for dust was comparable to other aerosol types, the strong forward scattering peak significantly limits the amount of light scattered at other angles. The combination of this low absolute scattering intensity and systematic instrument noise resulting from stray light may produce significant biases in the dust  $\tilde{F}_{11}$  and  $-F_{12}/F_{11}$  measurement averages at angles above 90°.

The averages of the three SEAC<sup>4</sup>RS fine mode cases are examined individually in Figure 4.4. Visually the averages of the three types produce very similar angular scattering patterns, especially the biogenic and urban averages. The  $-F_{12}/F_{11}$  peak was slightly larger on average in the biomass burning cases, with this feature most clearly separating the BB aerosols from the other two types. Additionally, small differences in the shape of  $\tilde{F}_{11}$  can also be observed in the Biomass Burning averages, where the forward and backward scattering peaks are suppressed relative to the other two types.

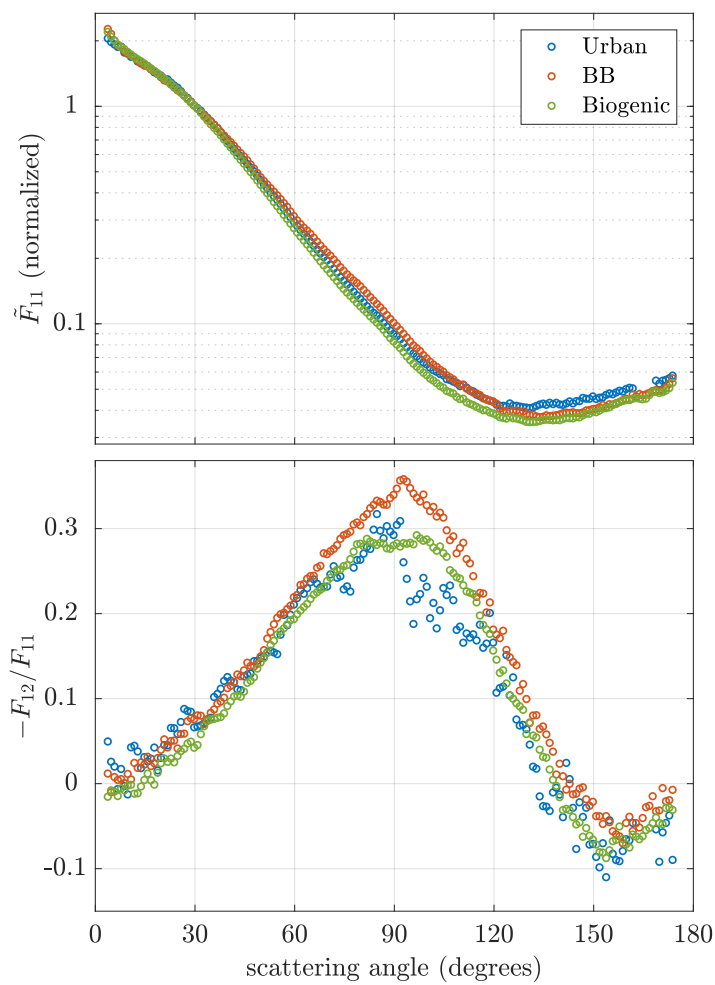


Figure 4.4: Average  $\tilde{F}_{11}$  and  $-F_{12}/F_{11}$  data for the three fine mode aerosol classifications in SEAC<sup>4</sup>RS. Small gaps in the data (ex. urban points  $\sim 165^\circ$ ) were removed due to strong biases from stray light.

The variability within a given type’s scattering data (not shown) was the highest in the case of the samples associated with urban emissions. Further examination of this variability showed two distinct subgroups, with the conditions around the Ohio River Valley differing significantly from conditions near urban centers. The starkest difference between these two subgroups occurred in the  $-F_{12}/F_{11}$  maxima, with significantly higher peaks occurring in measurements made near the Ohio River Valley. The GRASP retrieval generally attributed these differences to much larger fine mode diameters in the urban center cases than in the cases near the Ohio River Valley.

## 4.5 PCA Analysis

It is evident from the results of the previous section that there are differences in the averaged scattering data that agree well with the physical expectations of each aerosol type. While this result is encouraging, the averages alone do not tell us if these differences are characteristic of the majority of samples or are driven by a relatively few extreme cases. The regularity of the geographic patterns observed in Figure 4.2 does suggest a consistent physical basis for the classification scheme in the majority of SEAC<sup>4</sup>RS cases but it says nothing about the DC3 classification where sample location is already the primary classification metric. Additionally, as none of the properties used by the SEAC<sup>4</sup>RS classification scheme are directly related to aerosol optical measurements, it is possible that the geographic distributions observed capture patterns in features of the air masses that are not reflected in the optical properties of the corresponding aerosol populations. In order to confidently say that the majority of cases have aerosol optical properties that are clearly characteristic of the corresponding type we must examine PI-Neph measurements as a function of type on the level of individual cases. Unfortunately, the subtle differences between

many of the scattering measurements and the high dimensionality of the data set complicates a direct analysis of the relevant features. In the following section, this analysis is simplified by reducing the dimensionality of the PI-Neph measurements with principal component analysis. This approach leads to a clear picture of the type-driven clustering of cases that occurs in scattering element space as well as permits easy identification of the features that are characteristic of each aerosol category.

Principal component analysis was performed on all PI-Neph measurement averages to simplify the scattering data and more easily explore its relationship with the classification categories. Intuitively, PCA transforms the data to a new coordinate system in such a way that the greatest variance in the data lies along the first coordinate, the next largest variance lies along the second axis and so forth. The basis vectors of this new coordinate system are the eigenvectors of the original data's covariance matrix. As most of the data's variance is captured in the first few principal components, the dimensionality of the measurement can be significantly reduced while still maintaining the bulk of the original information content. In this work, the orthonormal basis vectors making up this new coordinate system (i.e. the normalized eigenvectors of the covariance matrix) are referred to as 'loadings', and the basis vectors coefficients required to represent each data point are referred to as 'scores'. It is important to note that PCA is an unsupervised technique and the results are therefore independent of any hypothesis regarding the data, including the ancillary data classification scheme.

PCA was performed on all 532nm PI-Neph averages from the combined SEAC<sup>4</sup>RS and DC3 datasets (2,334 samples) simultaneously. While the data from the two campaigns was merged, the unpolarized and polarized measurements were kept separate in the final analysis (i.e. the PCA routine was run twice, once for  $\tilde{F}_{11}$  and again for the  $-F_{12}/F_{11}$  dataset). Individual  $\tilde{F}_{11}$  measurements can often span several orders

of magnitude between the forward scattering peak and side scattering angles. To prevent the first few principal component loadings from being dominated by the large absolute variations in forward scattering intensity the analysis was performed on the natural logarithm of the  $\tilde{F}_{11}$  values. This transformation produces a set of principal components where the first component, for example, explains the most possible *relative* variance in data [Shcherbakov et al., 2016]. No transformation was applied to the  $-F_{12}/F_{11}$  measurements. The angular range of the final inputs to the PCA routine was  $5^\circ$  to  $170^\circ$  in the case of both the  $\tilde{F}_{11}$  and the  $-F_{12}/F_{11}$  datasets. This range corresponds to the angles where data was present during all measurement periods over both campaigns. Data points where instrument noise produced non-physical (i.e.  $F_{11}(\theta) < 0$  or  $|F_{12}(\theta)/F_{11}(\theta)| > 1$ ) values were excluded from the analysis.

The decision to treat the intensity and polarization information separately when performing the PCA was based on two factors. The first stems from the fact that most modern measurements of the optical properties of atmospheric aerosol are polarization insensitive. Isolating the polarization information permits conclusions that are more applicable to polarization insensitive instrumentation while simultaneously helping to illuminate the potential benefits of adding polarization capabilities to future instrumentation. The second factor results from the fact that PI-Neph data often contains systematic noise that is strongly correlated over time and scattering angle but is very weakly correlated between  $\tilde{F}_{11}$  and  $-F_{12}/F_{11}$ . By separating these datasets, the variability in the data corresponding to these systematic artifacts can be more effectively isolated, allowing the remaining components to more accurately capture the physical variation among the samples. This hypothesis is supported by the fact that some of the loadings closely matched the angular error correlations known to result from certain instrumental artifacts. Additionally, a significantly reduced separation of aerosol types in PCA score space was observed when PCA was performed

on the intensity and polarized measurements simultaneously. This observation was consistent regardless of the relative weights applied to the  $\tilde{F}_{11}$  and  $-F_{12}/F_{11}$  variances.

#### 4.5.1 PCA Loadings and Scores

The PCA loadings derived from the combined dataset off all DC3 and SEAC<sup>4</sup>RS measurements are shown in Figure 4.5. The first three  $\tilde{F}_{11}$  components explained 84% of the total variance in the  $\tilde{F}_{11}$  data, while the corresponding three  $-F_{12}/F_{11}$  components were able to explain 65% of the variance in the  $-F_{12}/F_{11}$  measurements. The second  $-F_{12}/F_{11}$  loading closely matched a known measurement artifact that is driven by small variations in PI-Neph laser power over the course a given measurement. Similarly, the fourth  $\tilde{F}_{11}$  loading (not shown) matched a known artifact produced by relative drifts in the calibration of the forward and backward scattering angles, often driven by fouling of the beam folding mirror inside the PI-Neph chamber.

A 3D scatter plot of the scores from the first two  $\tilde{F}_{11}$  principal components and the first  $-F_{12}/F_{11}$  component is shown in Figure 4.6. The points are colored according to the classified results of the aerosol typing algorithm described in Section 4.3 (unclassified points are excluded for clarity). A simple physical interpretation of the individual principal components is not readily apparent but strong clustering of the points as a function of aerosol type is evident. The grouping of aerosol types by purely optical means suggests that the optically independent typing algorithm is capable of capturing significant underlying commonalities in particle properties that extend beyond the metrics directly used by the algorithm itself.

In order to qualify the level of clustering by aerosol types in PCA score space the success of two different prediction algorithms are evaluated against the data.

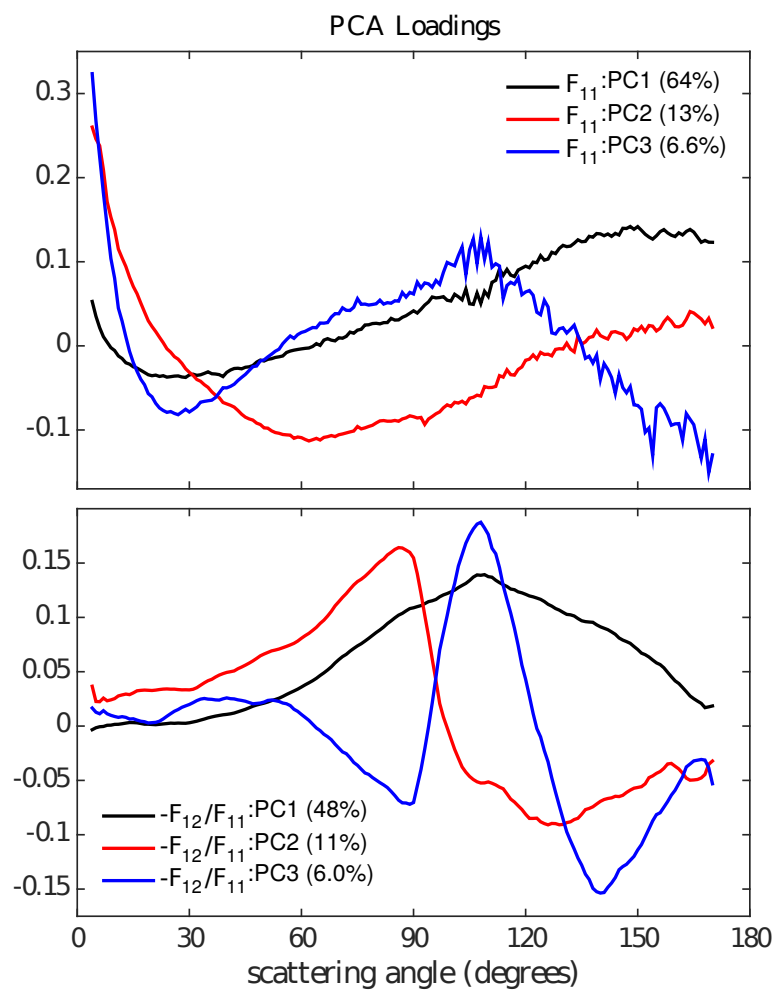


Figure 4.5: The resulting loadings of the first three principal components from both the  $\tilde{F}_{11}$  and  $-F_{12}/F_{11}$  data.

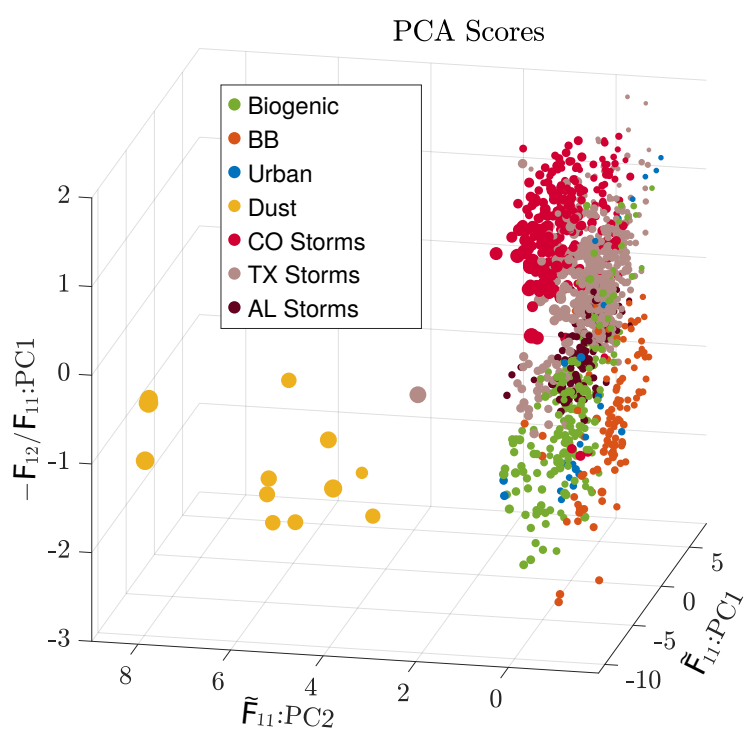


Figure 4.6: The resulting PCA scores, color coded by type, as a function of the first two  $\tilde{F}_{11}$  principal component scores and the first  $-F_{12}/F_{11}$  score. The points are sized according to the effective radius determined by the GRASP retrieval.

These algorithms attempt to predict the results of the optically independent typing algorithm using only the PCA scores of the corresponding PI-Neph average by exploiting the clustering of each aerosol type. The dimensionality of the original data (166 angles in both  $\tilde{F}_{11}$  and  $F_{11}/F_{12}$ ) is often significantly higher than the number of measurements available for a given aerosol type. If all principal component scores were used in the prediction scheme many aerosol types could be identified with very high fidelity based only on the noise “fingerprints” of their individual measurements. Reducing the dimensionality of data down to only a few key variables (i.e. the first few principal components) forces the classification to rely primarily on physical features of the measured aerosol that are common to all samples of that type. Sections 4.5.2 and 4.5.3 describe two prediction schemes used to quantify the degree of separation between each of these populations, while simultaneously exploring the distinguishing optical characteristics of each category.

#### 4.5.2 Identifying Types by Mahalanobis Distance

The first of the two prediction schemes estimates the optically independent classification of a given sample based on the Mahalanobis distance between that sample’s point in PCA score space and the corresponding clusters of points defined by the classification algorithm. Mathematically the Mahalanobis distance  $D_M(\vec{x})$  of a given point  $\vec{x} = (x_1, x_2, \dots, x_n)^T$  from the mean of a cluster of points  $\vec{\mu} = (\mu_1, \mu_2, \dots, \mu_n)^T$  is defined by

$$D_M(\vec{x}) = \sqrt{(\vec{x} - \vec{\mu})^T \mathbf{S}^{-1} (\vec{x} - \vec{\mu})} \quad (4.1)$$

where  $\mathbf{S}$  represents the covariance matrix of all points in the cluster and the superscript  $T$  represents the transpose of the corresponding vector [McLachlan, 2004]. Intuitively, the Mahalanobis distance provides a metric of the separation between a

test point and a cluster of points, scaled by the dispersion of the cluster along the axis passing through the test point and the center of cluster. The use of Mahalanobis distance in this prediction technique permits the algorithm to take the size and shape of each cluster into account when attempting to discriminate between types. This feature prevents classification types with more loosely bound clusters from being “disadvantaged” when evaluating the distance to a given point from the cluster in question. For example, a point lying halfway between (in euclidean space) the dust and AL storms clusters would have a much shorter Mahalanobis distance to the center of the more disperse dust cluster.

Specifically, the predicted optically independent classification of a given sample corresponds to the cluster with the shortest Mahalanobis distance to the PCA scores representing the sample in question. For any given sample, the Mahalanobis distance to the cluster containing the pertinent data point is calculated with the relevant point excluded (i.e.  $\vec{x}$  is never included in the calculation of  $\vec{\mu}$  or  $T$  when determining  $D_M(\vec{x})$ ). All points classified as urban by the optically independent scheme were excluded from this prediction scheme due to the limited number of data points and large variability in PCA scores. Additionally, all unclassified points were also excluded, leaving six remaining types to which a given point in PCA score space could be assigned.

The Mahalanobis distance prediction technique is implemented using five different combinations of the first three  $\tilde{F}_{11}$  PCA scores and first  $-F_{12}/F_{11}$  scores. All other PCA score were excluded from this analysis either because of clear influences from known instrument artifacts or due to their inability to explain a significant portion of the data’s variance. The ability of this separation technique to identify cases of the correct type, for each combination of component scores, is then quantified

through the true positive rate (*TPR*). The TPR, also known as recall, is defined as

$$TPR = \frac{N_{predicted}^{type}}{N_{total}^{type}} \quad (4.2)$$

where  $N_{predicted}^{type}$  is the number of cases of the given type correctly predicted and  $N_{total}^{type}$  is the total number cases of the that type. The resulting TPR values for five different combinations of PCA scores is shown in Table 4.2. If a sufficient number of principal component scores are considered recall values are generally quite high, often exceeding 85%. The fact that such a high proportion of individual cases can be correctly identified is surprising considering the very small differences observed among the  $\tilde{F}_{11}$  and  $-F_{12}/F_{11}$  averages shown in Figures 4.3 and 4.4. This result reinforces the validity of the optically independent classification scheme. Moreover, it demonstrates the potential power of the PCA technique when applied to light scattering measurements with high angular resolution and range to distinguish aerosol type without the need for ancillary data.

The improvements in recall resulting from the inclusion of additional components provides a measure of their relative importance when attempting to distinguish aerosol types. In the biomass burning and CO storm cases the addition of the first  $-F_{12}/F_{11}$  scores always results in an increase in recall by over 10%, suggesting  $-F_{12}/F_{11}$  can play an important role in correctly identifying these types. Conversely, the TX/OK and AL storm cases showed no meaningful improvement in the prediction ability of the Mahalanobis distance algorithm when  $-F_{12}/F_{11}$  scores were incorporated. Similar conclusions can be made regarding the different  $\tilde{F}_{11}$  components. For example, the biogenic recall is always significantly improved with the addition of the second and third  $\tilde{F}_{11}$  principal components.

The Mahalanobis distance based prediction scheme is significantly less success-

ful on the AL storms than the other aerosol types. In order to better understand this discrepancy, we examine the incorrectly classified cases in more detail. The confusion matrix [Stehman, 1997] detailing the prediction scheme's performance for the case where all four principal components are used is listed in Table 4.3. The rows of this matrix represent instances of the actual optically independent classification while the columns show the corresponding number of cases predicted by Mahalanobis distance scheme. It is apparent that the Mahalanobis distance approach has significant difficulty discriminating the AL storm cases from the biogenic cases. This result is not surprising given that the AL region corresponds to a region that was dominated by biogenic emissions during SEAC<sup>4</sup>RS according to the original classification scheme. It is likely that some of these SEAC<sup>4</sup>RS biogenic cases were even measured within the vicinity of strong convective systems, further blurring the boundary between these two types. Additionally, as this is a relatively wet and vegetated region dust emissions that are driven by the strong winds associated with convective systems are expected to be significantly less than the other two storm domains.

Table 4.2: Recall (TPR) for the Mahalanobis distance based clustering for each aerosol type, given different combinations of principal component scores.

Type	$\tilde{F}_{11} : PC_{1-2}$	$\tilde{F}_{11} : PC_1; F_{12} : PC_1$	$\tilde{F}_{11} : PC_{1-3}$	$\tilde{F}_{11} : PC_{1-2}; F_{12} : PC_1$	$\tilde{F}_{11} : PC_{1-3}; F_{12} : PC_1$
Biogenic	64.4%	51.8%	87.2%	81.0%	90.7%
BB	72.4%	29.8%	63.8%	84.6%	83.7%
Dust	100.0%	100.0%	100.0%	100.0%	100.0%
CO Storms	72.7%	85.1%	76.4%	86.2%	86.2%
TX/OK Storms	58.0%	48.3%	81.4%	60.1%	81.6%
AL Storms	12.9%	15.9%	42.9%	12.3%	47.1%

Table 4.3: Confusions matrix for the Mahalanobis distance based clustering technique for the case where the first three  $\tilde{F}_{11}$  and first  $-F_{12}/F_{11}$  principal component scores are used (corresponding to the last column of Table 4.2). Several rows of the table sum to slightly less than the number of cases shown in Table 4.1 because PCA scores could not be calculated for averages containing non-physical measurements at one or more angles.

		Predicted Classification					
		Biogenic	BB	Dust	CO Storms	TX/OK Storms	AL Storms
Actual	Biogenic	224	8	1	2	9	3
	BB	15	87	0	0	1	1
	Dust	0	0	12	0	0	0
	CO Storms	0	0	0	225	35	1
	TX/OK Storms	13	0	1	72	429	11
	AL Storms	52	5	0	2	14	65

### 4.5.3 Identifying Types with a Dividing Plane

The Mahalanobis distance technique effectively identified types that are surrounded by other clusters, but clusters lying on the edge of the PCA score space can potentially be identified more accurately using other techniques. In this section, a plane is used to divide three dimensional PCA score spaces into two regions, representing positive and negative predictions of a given optically independent classification. The location of this separating plane is unique to each aerosol type and is chosen to produce the highest quality predictions possible. This technique proves to have stronger predictive power than the Mahalanobis distance technique for several aerosol types, while simultaneously providing a more intuitive picture of the characteristic optical features of a given classification. It also allows for the inclusion of the urban and unclassified points that were discarded in the Mahalanobis distance prediction scheme.

In this prediction scheme the distance of a given point from the dividing plane strongly corresponds to the likelihood of this point being a member of the relevant aerosol type. Similarly, light scattering features characteristic of the aerosol type in question can be identified by examining the basis vector that corresponds to the line normal to the separating plane in PCA score space. Since the direction of this normal line is determined by a plane, the scattering features corresponding to this direction in PCA score space are always the same, regardless of the location of the point in question. This fact results from the use of a plane to separate the aerosol types, and is not true of the Mahalanobis distance technique where the classification boundaries are much more complex. For example, in the Mahalanobis distance classification scheme, two points that are diametrically opposite the center of a cluster will require opposite changes in their scattering patterns to increase their probability of being associated with the relevant cluster. It should be emphasized though that the separating plane

technique only produces a binary classification (the test point either is or is not predicted to be of the relevant aerosol type) and the method is ineffective at identifying points in clusters that are surrounded by other clusters.

The dust, biomass burning and CO storms clusters are especially well-suited for the separating plane technique as their principal component scores lie on the outer edge of the other datasets in most dimensions. The technique was applied to each of these aerosol types, once using all three  $\tilde{F}_{11}$  principal component scores and again using only the first two of these scores as well as the first  $-F_{12}/F_{11}$  score (i.e. the scores plotted in Figure 4.6). Unless otherwise stated the separating plane was chosen to divide the relevant aerosol type from all other aerosol types, including the 'unclassified' samples.

When using the Mahalanobis distance based technique each point was only assigned to one category so false positives in one aerosol type resulted in a reduction of the TPR value in another type. In the separating plane technique, each aerosol type is treated as binary classification problem that is independent of the other air mass types. Therefore, the percentage of cases of a given type that were correctly classified is an insufficient metric as a plane chosen infinitely far from the origin will always result in  $TPR = 100\%$ . In order to address this issue, we also make use of the true negative rate

$$TNR = \frac{N_{predicted}^{other}}{N_{total}^{other}} \quad (4.3)$$

where  $N_{predicted}^{other}$  is the number of cases that were correctly predicted as not being of the relevant type and  $N_{total}^{other}$  is the total number cases that are not of the relevant type. For each aerosol type the location and orientation of the separating plane was chosen to maximize the product  $TPR \times TNR$ . This metric—the fraction of cases of the relevant type that were correctly predicted times the fraction of cases not of the

relevant type that were correctly predicted—takes into account both the sensitivity of the prediction as well as its ability to exclude cases of other types.

To further examine the technique’s ability to separate different aerosols, comparisons were made between a given category and subsets of categories containing only types with very similar aerosol properties. The first of these comparisons attempted to separate the biomass burning samples from other fine mode aerosols. The fine mode aerosols used in this test included all aerosol types whose average size distribution, as retrieved by GRASP, yielded a fine mode that had greater than five times the volume of the coarse mode. These remaining categories included the biomass burning, biogenic, urban/industrial types as well as convective storm inflow from the Alabama domain. Additionally, an attempt was made to separate all the CO storm cases from the AL storm cases. This comparison serves both to exemplify the significance of the differences between the storms as well as better clarify the continuum on which the light scattering properties of all DC3 storm domains can be projected.

Table 4.4 shows the resulting *TPR* and *TNR* values from the separating plane prediction technique. In most cases the algorithm can predict the classification correctly as well as rejecting cases that are not of the relevant type with better than 90% accuracy. The last column of Table 4.4 contains a parameter quantifying the role of the first principal component of  $-F_{12}/F_{11}$  in identifying the corresponding aerosol type. This value  $F_{12} : PROJ$  corresponds to the projection of the unit vector normal to the separating plane, pointing in the direction of the desired classification, onto the axis corresponding to the scores of the first principal component of  $-F_{12}/F_{11}$ . An absolute value of  $F_{12} : PROJ$  approaching unity indicates that the separation is completely determined by  $-F_{12}/F_{11}$ , while values approaching zero indicate no sensitivity in the first principal component of  $-F_{12}/F_{11}$  to the corresponding type. The sign of  $F_{12} : PROJ$  indicates whether “more” or “less” of the first principal component of

$-F_{12}/F_{11}$  is indicative of the type in question.

In all cases where the  $-F_{12}/F_{11}$  component is included, the algorithm predicts the classification correctly with better than 90% accuracy and, with the exception of the CO storms, it shows equivalent skill rejecting cases that are not of the relevant type. The predictive accuracy of the scheme when using the third  $F_{11}$  component is similar, except in the case of the BB samples. This is consistent with the results suggested by previous section, where the first  $-F_{12}/F_{11}$  component was found to be crucial in obtaining high biomass burning recall under the Mahalanobis distance technique. Interestingly, the ability of the dividing plane technique to correctly reject points that were not of the CO storm classification was significantly improved when the first  $-F_{12}/F_{11}$  principal component was replaced by the third  $F_{11}$  component. This result is contrary to the very large values of  $F_{12} : PROJ$  and the conclusion of Section 4.5.2. Investigations of both of these components' PCA scores in the case of the CO storms showed that this peculiarity resulted from both apparently random features in the distributions of the PCA scores as well as significant sensitivity to this type in the third  $F_{11}$  component. The dividing plane technique also demonstrated strong predictive power in the case of the dust samples, eliminating many of the false positives shown in Table 4.3, regardless of the choice of included principal components.

Table 4.4:  $TPR$  and  $TNR$  values for the separating plane classification prediction technique. The  $\tilde{F}_{11} : PC_{1-3}$  columns correspond to the case where only phase function principal components are used, while the columns of  $\tilde{F}_{11} : PC_{1-2}; F_{12} : PC_1$  make use of the first two phase function PCA scores as well as the first  $-F_{12}/F_{11}$  score.

Separated Types	$\tilde{F}_{11} : PC_{1-3}$		$\tilde{F}_{11} : PC_{1-2}; F_{12} : PC_1$		
	$TPR$	$TNR$	$TPR$	$TNR$	$F_{12} : PROJ$
Dust vs. All	94.1%	97.6%	93.8%	98.3 %	0.37
BB vs. All	90.3%	80.3%	90.3%	95.0%	-0.54
BB vs. Fine	74.8%	89.2%	91.3%	91.6%	-0.50
CO Storms vs. All	91.3%	91.6%	94.3%	81.2%	0.80
CO vs. AL Storms	97.6%	95.7%	96.2%	97.8%	0.83

Figure 4.7 is colored by aerosol type and shows the frequency distribution of the PCA scores' distances from the pertinent separation plane. Sub-panels (a) and (c) show the distribution of biomass burning and CO storm distances against the distribution of distances for all other types. In both cases the targeted type separates clearly from the remaining cases. The strong separation between the biomass burning samples and other fine mode averages shown in sub-panel (b) shows that the distinguishing features of the BB cases extends significantly beyond the magnitude of the coarse mode. Sub-panel (d) shows the separation between the AL and CO storms. The TX/OK storms are also included to illustrate how this type has many characteristics that fall in between the two other storm domains. The overlap between TX/OK storm distributions and the AL and CO storm distributions makes sense in light of the fact that these types are often confused with each other in the Mahalanobis distance based scheme (see Table 4.3) and have clusters that overlap in Figure 4.6.

The normalized rotated loadings shown in Figure 4.8 represent the basis vector corresponding to the normal line of the relevant separating plane. These curves were derived from the first three  $\tilde{F}_{11}$  principal components and can be intuitively conceptualized as the scattering features contained in these components that become increasingly pronounced as a point's distance from the separating plane increases. Correspondingly, when these features are present to sufficient degree, there is a high probability of the corresponding aerosol belonging to the relevant type. Relatively high values of  $\tilde{F}_{11}$  around scattering angles of  $60^\circ$  and very low forward scattering peaks are the most prominent characteristics of the BB cases. The other extreme, exemplified by strong forward scattering and low relative values of side scattering is generally indicative of dust. The rotated loadings for CO storms indicates that they are well characterized by strong backscattering combined with a moderately strong

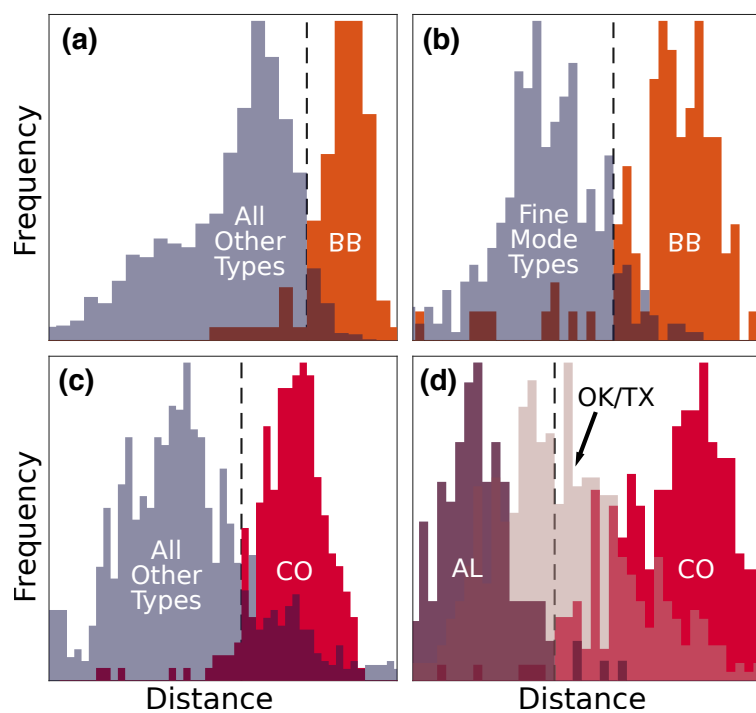


Figure 4.7: Histograms showing the separation of aerosol types along their corresponding rotated basis component. Panel (a) shows the biogenic cases (orange) against all other types (grey), while panel (b) shows the biogenic cases against only the fine mode points. Panels (c) shows the CO storms (red) against all other types, with panel (d) showing the CO storms along with only the AL (maroon) and OK/TX (beige) storms. The black vertical dashed lines represent the threshold between positive and negative classifications determined by the separating plane technique.

forward scattering peak.

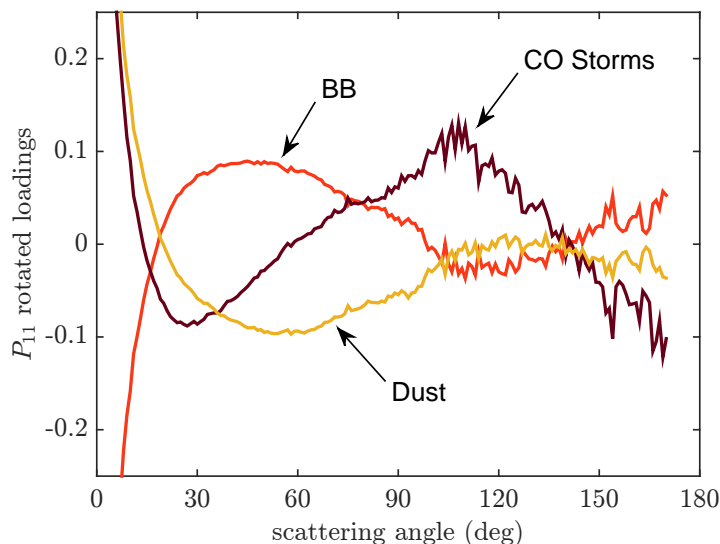


Figure 4.8: The rotated loadings corresponding to various aerosol types.

Thus, we have demonstrated that scattering properties alone, as measured by the PI-Neph, reduced to a few principal components, and analyzed by either the Mahalanobis or Dividing Plane technique can distinguish the same aerosol types as identified by a classification scheme that uses only composition, size and gas tracer data. We now apply a sophisticated inversion scheme to the PI-Neph-measured scattering properties to make use of the distinguishing features of these measurements to obtain physical and optical properties of each aerosol type.

## 4.6 GRASP Retrievals

The GRASP algorithm was applied to each case independently and the resulting size distributions, real part of the refractive indices and spherical fractions were averaged to obtain values representative of each aerosol type. Parameterizations of the resulting size distributions were also performed to provide values that are easily transferable

to other applications, as well as to better understand the variations within a given classification. The fine and coarse mode are parameterized separately, with the two modes being separated by the minimum in the retrieved size distribution closest to  $r = 400\text{nm}$ . The metrics used to characterize each mode in the PSD are chosen to be consistent with the parameterizations used in Dubovik et al. [2002]. Specifically, the volume median radius  $r_v$ , standard deviation of the volume median radius  $\sigma$  and volume concentrations  $C_v$  are all provided along with the one standard deviation variability in the corresponding retrieved values. Note that the one standard deviation range reported includes both retrieval error *and* natural variability in the samples. While the retrieved modes of the size distributions do not exactly match log normal distributions these parameters were chosen to match those of true log normal size distributions if a real log normal mode was observed [Dubovik et al., 2002].

The retrievals were performed by inverting  $F_{11}$  and  $-F_{12}/F_{11}$  data simultaneously for each case. As in the principal component analysis, measurement angles containing non-physical values were excluded from the retrieval. The inversions of the SEAC<sup>4</sup>RS data incorporates all three PI-Neph wavelengths but only the retrieved refractive indices corresponding to 532nm are shown here. The retrievals of DC3 data were limited to 532nm data as the red and blue channels were not available at the time of this campaign.

As a result of their low scattering efficiencies, the size distribution retrieved by GRASP does not account for particles with radii smaller than  $\sim 60\text{nm}$ . While these particles are important to many applications, their effect on the total visible light scattered by a typical polydisperse, atmospheric aerosol is quite small. To better quantify the effect of these particles the SMPS size distribution, which extends down to  $r = 5\text{nm}$ , was stitched to the size distribution retrieved by GRASP and the results were averaged over the entire SEAC<sup>4</sup>RS experiment. A Mie code [Mishchenko et al.,

2002] was then used to estimate the total amount of 532nm light scattered by particles smaller than the center diameter of the first non-zero size bin ( $r = 66\text{nm}$ ). It was found that these particles were responsible for only 0.1% of the total light scattered by the fine mode ( $r < 400\text{nm}$ ) of the stitched size distribution. As the shape of  $F_{11}$  can depend significantly on size parameter the contribution of these particles to the absolute phase function was also examined. It was found that the particles with radii smaller than 66nm had the largest contribution to  $F_{11}$  around  $152^\circ$ , where they made up 0.9% of the total signal. Additionally, the tiny scattering signal produced by the smallest particles can be transferred into other size bins (and potentially very small changes in refractive index) producing an “optically equivalent” set of parameters. Therefore, we do not expect the ability of the retrieved parameters to reproduce the true optical properties of the aerosol in question to be significantly hindered by GRASP’s exclusion of the smallest particle sizes.

Except for the dust category, samples for which the residual between the GRASP fit and measured data  $F_{11}$  was greater than 12% were excluded from the data shown in this section. No dust cases had residuals that met this criterion so, to prevent the exclusion of this aerosol type, all dust cases were included regardless of the  $F_{11}$  residual. The total scattering was reasonably high for many of the dust samples ( $\bar{\beta}_{sca} = 38 \text{ Mm}^{-1}$ ) but the strong forward scattering peak produced by these aerosols means that most of the scattered light is directed toward low scattering angles. In turn, the measurements at higher scattering angles were often very weak and dominated by instrument noise. The noise likely has a significant impact, both on the quality of the retrieval fit but also on the accuracy of the retrieved parameters which are highly sensitive to the backward scattering angles, like real refractive index [Zhao et al., 1997].

The final column of Table 4.1 shows the percentages of cases that had  $F_{11}$

GRASP residuals that met the 12% threshold condition. In the CO storm cases only 61% of cases meet the 12% threshold. Excluding the dust category, this percentage is significantly lower than all other classified types and is at least partially driven by very low particle concentrations ( $\bar{\beta}_{sca} = 27 \text{ Mm}^{-1}$ ) found in these samples. Additionally, the CO storm observations contained a significant coarse mode which, as in the case of the dust samples, drove a large fraction of the scattered light into the forward angles. While this effect was less dramatic than what was observed in the dust phase functions, it still may have contributed significantly to the differences between the fit and measurement. It is also important to note that while GRASP does contain a non-spherical aerosol model in its retrieval, significant assumptions are still required (i.e. homogenous spheroids, constrained shape distribution, etc.). As the CO storms and dust cases likely have the most optically significant deviations from spherical particles (they both have relatively low retrieved spherical fractions and significant coarse modes), it is possible that the large residuals are driven, at least in part, by deviations in true particle morphology from the assumptions made by GRASP's non-spherical aerosol model.

The large number of unclassified points with high residuals is driven by very low aerosol loading ( $\bar{\beta}_{sca} < 20 \text{ Mm}^{-1}$ ) observed in the majority of the unclassified cases. In the other categories, many of the residuals are quite low, often less than what is expected between the true value and the PI-Neph measurement given instrumental errors alone. This suggests that GRASP is successful fitting some features of the measurement that correspond to instrumental artifacts.

In order to test the consistency of the retrieval, GRASP was also applied once to the scattering data averaged over all cases of a given aerosol type. The results agreed well with the averages of all GRASP retrievals for each case of a given type, when no filtering of the final averages based on the residuals was imposed. This result

is encouraging as the mapping between particle populations and their absolute phase functions is linear, so for reasonably small levels of instrument noise the linear average of the retrievals and the retrieval of the average are expected to agree well.

#### 4.6.1 Retrieved Size Distributions

The normalized size distributions retrieved from PI-Neph data, averaged by sample type, are shown in Figure 4.9. Significant difference in the magnitude of the coarse mode between the separate categories is clearly evident. Size distributions from all three DC3 storm domains contained notable coarse modes, with the most coarse particles found in the CO storms, followed by OK/TX and then AL storm samples. The presence of these coarse mode particles is consistent with the large amount of dust that is believed to have been lifted by the associated storms [Corr et al., 2016]. Additionally, the relationship between the fraction of particle belonging to the coarse mode and the climatological features of the three storm domains supports the hypothesis that surface aridity plays an important role in determining the properties of aerosols associated with convective systems. No detectable coarse mode was found in any of the SEAC<sup>4</sup>RS types except for dust, which had the largest relative number of coarse mode particles of any classification. We note that the coarse modes presented in Figure 4.6.1 are all skewed to smaller sizes than those retrieved by GRASP-like inversions applied to the total column ambient sky radiance measurements of AERONET [Dubovik et al., 2002]. As mentioned in Section 2.1.3, the inlet feeding aerosols to the PI-Neph on the DC-8 had a 50% passing efficiency at an aerodynamic radius of  $1.8\mu\text{m}$  [McNaughton et al., 2007], thereby severely limiting coarser particles in the sample and skewing the retrieval results.

The fine modes of all types have relatively similar distribution shapes. The

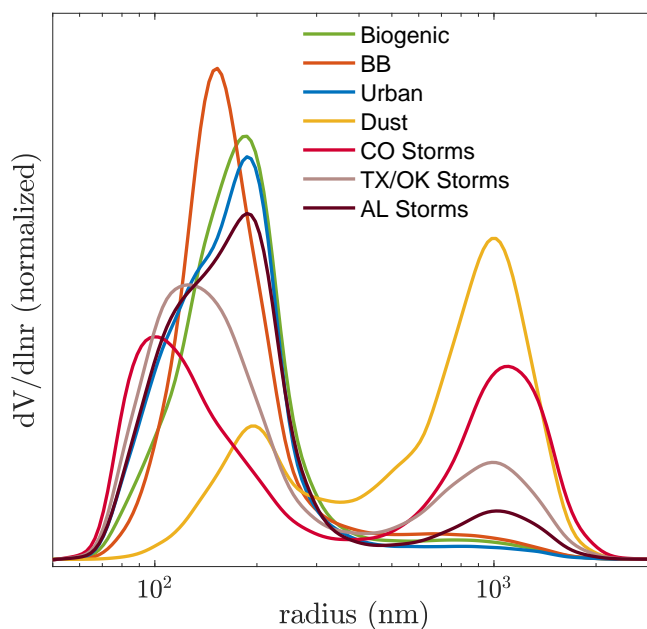


Figure 4.9: Retrieved mean particle size distributions for all classification types.

clearest differences are apparent in the storm inflow cases, especially in CO (and TX/OK to a lesser extent), where the size distributions are significantly shifted toward the smaller size bins. The average fine mode distributions of the DC3 storm cases are also slightly wider than the other distributions. The width of the distributions plotted in Figure 4.9 can be driven both by retrieved size distributions that are consistently broader in the bulk of individual cases, as well as averaging artifacts arising from high variability in peak of the distribution. The wide fine mode observed in the urban classification is driven primarily by the later effect, with a wide range of center diameters being found among the individual averages of that type. Outside of this feature, there is little difference among the size distributions of the SEAC<sup>4</sup>RS fine mode dominant classifications.

The wide spread in urban size distribution peak diameters can be better understood by separating the category into two distinct subpopulations. The first of

these two subpopulations is associated with very high scores of the first  $-F_{12}/F_{11}$  principal component and in turn relatively high  $-F_{12}/F_{11}$  maxima. The retrieved values indicate that the fine mode of these aerosols was composed of some of the smallest particles ( $r_{vf} = 148 \pm 29\text{nm}$ ) observed during SEAC<sup>4</sup>RS. The measurement locations of this subpopulation were also correlated strongly with the aircraft's proximity to the Ohio River Valley, a region known for high industrial activity. The second subpopulation was composed primarily of negative  $-F_{12}/F_{11}$  first principal component scores, with GRASP indicating fine particle sizes that were significantly larger ( $r_{vf} = 171 \pm 11\text{nm}$ ). Sampling periods corresponding to this second subpopulation correlated strongly with the DC-8's distance to population centers, particularly Houston and Dallas Texas. Despite the differences between these two classes of particles, the two types were combined into a single group due to underlying anthropogenic nature of the emissions and the limited number of cases of each subtype.

Table 4.5: Fine and coarse mode parameterizations of retrieved size distribution as well as real refractive index and spherical fractions for each aerosol type as well as the unclassified cases (Unclas.). All spectrally dependent parameters are listed at 532nm.

Aerosol Type	$r_{vf}(\text{nm})$	$r_{vc}(\text{nm})$	$\sigma_f$	$\sigma_c$	$C_{vf}(\frac{\mu\text{m}^3}{\text{cm}^3})$	$C_{vc}(\frac{\mu\text{m}^3}{\text{cm}^3})$	$n_{532\text{nm}}$	$sphere$ (%)
Biogenic	$171 \pm 19$	$1022 \pm 124$	$0.37 \pm 0.08$	$0.23 \pm 0.04$	$13 \pm 4.9$	$0.59 \pm 0.71$	$1.50 \pm 0.03$	$89 \pm 24$
BB	$168 \pm 11$	$998.3 \pm 119$	$0.37 \pm 0.07$	$0.22 \pm 0.04$	$23 \pm 19$	$1.1 \pm 1.4$	$1.54 \pm 0.03$	$90 \pm 19$
Urban	$164 \pm 24$	$1055 \pm 155$	$0.36 \pm 0.05$	$0.23 \pm 0.03$	$16 \pm 7$	$1.3 \pm 3.9$	$1.49 \pm 0.04$	$95 \pm 19$
Dust	$194 \pm 40$	$940.6 \pm 188$	$0.34 \pm 0.09$	$0.31 \pm 0.07$	$7.5 \pm 3.3$	$18 \pm 11$	$1.47 \pm 0.05$	$72 \pm 35$
CO	$134 \pm 15$	$1018 \pm 135$	$0.36 \pm 0.08$	$0.29 \pm 0.04$	$4.7 \pm 2.4$	$3.8 \pm 1.8$	$1.56 \pm 0.06$	$46 \pm 38$
TX/OK	$144 \pm 15$	$957.4 \pm 145$	$0.39 \pm 0.08$	$0.27 \pm 0.04$	$8.9 \pm 3$	$2.7 \pm 1.2$	$1.55 \pm 0.05$	$80 \pm 32$
AL	$157 \pm 11$	$1022 \pm 95.1$	$0.38 \pm 0.06$	$0.25 \pm 0.03$	$9.9 \pm 4$	$1.1 \pm 0.59$	$1.51 \pm 0.03$	$93 \pm 16$
Unclas.	$149 \pm 43$	$936 \pm 188$	$0.36 \pm 0.12$	$0.26 \pm 0.06$	$8.7 \pm 6$	$3.9 \pm 9.9$	$1.52 \pm 0.07$	$77 \pm 33$

In addition to potentially aiding the parameterization of aerosol properties in remote sensing and climate modeling contexts, the statistics shown in Table 4.5 provide additional context to the retrieved parameters, beyond what is shown in Figure 4.9. As these values are calculated for each individual retrieval and then combined to obtain values representative of the relevant type, the averaging artifacts discussed above are eliminated. For example, the low values of  $\sigma_f$  and high  $r_{vf}$  standard deviation observed in the urban type confirms the wide fine mode seen in Figure 4.9 was not representative of individual cases.

Several interesting features stand out in the parameterizations of the retrieved values. The parameters representing the BB size distributions are almost identical to other fine mode types, suggesting that the scattering characteristics that uniquely isolate these particles in PCA score space are likely driven by differences in other features, like refractive index. The values of  $r_{vf}$  in the three DC3 storm types further emphasizes that this convective inflow had relatively small fine modes particles. A satisfactory physical explanation for this fact will require further study, but significant new particle formation, often occurring in and around convective systems [Jeong and Li, 2010; Eck et al., 2014], may have played a role. Lastly, it should be noted that the values of  $C_v$  highlight the uniqueness of the dust samples. These samples averaged coarse mode volumes that were over twice that of the fine mode, a value that is significantly higher than the corresponding ratios of any other category.

#### 4.6.2 Retrieved Real Refractive Indices and Spherical Fractions

The mean real refractive index retrieved from PI-Neph measurements is shown in Table 4.5 and generally falls between 1.5 and 1.56 for all aerosol types. The inversions of the biogenic, urban and AL storm categories all produced relatively small values

of  $n_{532nm}$ , with the values falling very close to 1.5. This value increased to 1.55 and then to 1.56 in the TX/OK and CO storm cases, respectively. The real refractive index of dust aerosol is often higher than that of other particles found over the study region [Dubovik et al., 2002; Curtis et al., 2008; Petzold et al., 2009]. Therefore, these elevated values of  $n_{532nm}$  are consistent with the hypothesis that the differences in aerosol properties between the three storm domains are primarily driven by increasing amounts of dust.

Figure 4.10 contains a box and whisker plot showing the full distribution of retrieved real refractive indices broken down by aerosol type. Several of the individual CO and TX/OK storm retrievals bumped up against the upper bound of the inversion at  $n_{532nm} = 1.65$ . These cases represented less than 5% of all retrievals corresponding to the CO and TX/OK types so it is unlikely that the limits of the inversion significantly biased the mean values reported in Table 4.5. No other values retrieved among the classified types approached the bounds of the inversion.

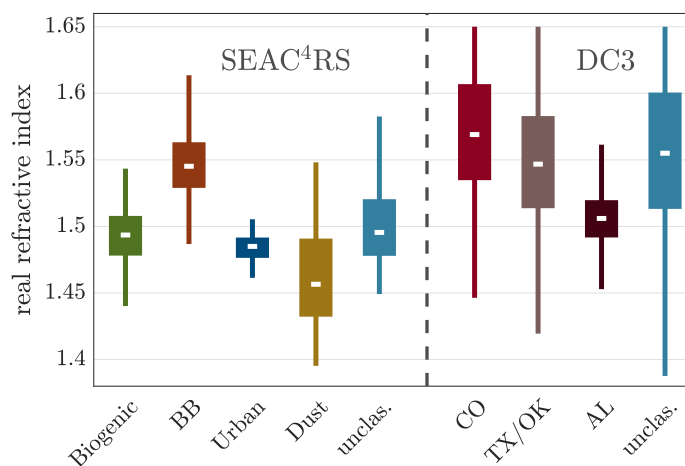


Figure 4.10: Retrieved real refractive index for all classifications types. Boxes contain the middle 50 % of the distribution, while the extent of the whiskers conveys the full range of retrieved values. The white dashes represent the median values of each aerosol type.

It is apparent from Figure 4.10 that the DC3 unclassified real refractive indices were significantly elevated relative to SEAC<sup>4</sup>RS unclassified cases. This result is not surprising as the storm categories often have higher values of  $n_{532nm}$  than other types and many of the DC3 unclassified cases may still have been influenced by convective systems. These influences include both outflow cases that were above 6km as well as potential convective system inflow that were sampled outside of the three identified storm domains.

The real refractive index values retrieved for the Saharan dust cases are significantly lower than the values reported in previous works [Dubovik et al., 2002; Petzold et al., 2009]. The high relative noise (resulting from very weak scattering intensities) in the backward scattering angles that have the most sensitivity to  $n$  may have significantly biased the retrieval. It should be noted that the large variability in dust  $r_{vf}$  shown in Table 4.5 is likely also driven by measurement artifacts produced by significant relative noise.

The PCA results of section 4.5 demonstrate that unique scattering features exist in the biomass burning cases that clearly distinguish these samples from other fine mode aerosols. Furthermore, using the separating plane technique of Section 4.5.3, the BB cases could be separated from just the biogenic samples with  $TPR$  and  $TNR$  values greater than 90%. Except for higher values of  $n_{532nm}$  in the case of the biomass burning samples, the retrieved parameters for these two types are almost identical in all aspects relevant to the PCA scores (normalized scattering components are independent of total particle concentration). This suggests that the scattering differences that are clearly evident between these two populations may be driven almost entirely by differences in real refractive index. It is also possible that changes in particle morphology may play a role, especially if these differences happen to closely mimic changes in real refractive index within the context of GRASP's aerosol model.

The retrieved imaginary parts of the refractive index were, on average, the same for the BB and biogenic samples ( $k_{532nm} = 0.01$ ). There are significant similarities, especially in  $-F_{12}/F_{11}$ , in the scattering changes produced by changes in the real and imaginary parts of the refractive index, in the relevant size ranges. While these similarities do meaningfully reduce the sensitivity of the retrieval to imaginary refractive index, it is unlikely that they explain a significant portion of the differences between BB and biogenic retrieved real refractive index values. The magnitude of the change in scattering patterns is opposite in sign but similar in magnitude for a fixed change in real and imaginary parts of the refractive index. This means that unrealistically large values of absorption ( $k_{532} \approx 0.05$ ) would be required to raise the retrieved biogenic real refractive index from 1.5 to 1.54. Correspondingly, forcing the imaginary refractive index to zero in the inversion of the biomass burning cases would only result in only about a 0.01 decrease in the retrieved real refractive index. Lastly, AERONET inversions of biomass burning aerosol have found imaginary refractive indices that are both similar to other fine mode aerosols and in line with the values retrieved here [Dubovik et al., 2002].

The retrieved fraction of spherical particles, shown in the last column of Table 4.1, was quite high for most categories. The retrieval indicated that 72% of the particles in the dust classification could be fit well with GRASP's spherical aerosol model. This result is contrary to much of the existing literature which suggests that dust is composed almost entirely of particle with aspect ratios significantly greater than unity [Reid et al., 2003; Chou et al., 2008; Legrand et al., 2014]. It is very likely that the retrieved dust spherical fractions may have also been contaminated by the high relative noise at high scattering angles, as this region conveys significant information regarding sphericity [Dubovik et al., 2006]. Additionally, aircraft inlet cutoff effects can artificially inflate the proportion of spherical particles sampled as

cutoff biases predominately impact the larger particle sizes where non-sphericity is expected to be greatest.

The CO storms had the lowest fraction of spherical particles (46%) of all air-mass types. This fact, combined with moderately increased non-sphericity in the OK/TX cases, further confirms the hypothesis that increasing amount of dust were present in these storms. The biogenic and urban categories also had spherical fractions in line with expectations as these aerosols are very frequently dominated by spherical particles.

The morphology of biomass burning particles can take on a variety of shapes including chain aggregates, solid irregulars and spheres, depending on the combustion material, burn conditions and the time since emission [Reid et al., 2005]. In the retrievals of SEAC<sup>4</sup>RS BB cases, 90% of the particles were found to have scattering patterns that were best reproduced by the spherical aerosol model. This high spherical fraction, combined with the fact that over 94% of BB cases had  $F_{11}$  residuals that were less than 12%, indicates that a spherical model can reproduce the optical properties of the sampled smoke well. This conclusion however does not necessarily imply that the BB particles were geometrically spherical. In fact, several studies have shown that the optical properties of a variety of smokes can correspond strongly with the expectations of spherical particles while scanning electron microscope (SEM) images reveal much more complex morphologies [Weiss et al., 1992; Martins et al., 1998], although this is not the case for all BB emissions [Chakrabarty et al., 2007]. Additionally, it's important to note the biomass burning size distributions were dominated by the fine mode and the sensitivity to sphericity from light scattering measurements is significantly reduced for smaller particle sizes.

## CHAPTER 5

# Conclusions

This work has presented a detailed conceptual and mathematical model for the potential calibration and data reduction of I-Neph datasets. This procedure was applied to PI-Neph measurements made both in the laboratory and during multiple airborne field campaigns to obtain measurements of phase function and polarized phase function for a wide range of aerosol types. A technique for retrieving size distribution, complex refractive index and spherical fractions from the resulting dataset was then explored. The resulting retrieved products correspond well with the existing literature and established instrumentation measuring in parallel to the PI-Neph, with the limited number of assumption required by this retrieval technique suggesting that it may represent a significant advance over many existing techniques. PI-Neph data from two large field campaigns, DC3 and SEAC<sup>4</sup>RS, are then examined in detail. An ancillary data classification scheme is developed to categorize the individual measurements and strong closure is observed between the scattering data and this optically independent classification. The GRASP retrieval is then used to find microphysical and optical parameterizations that are representative of each aerosol class. Several

novel geophysical conclusions originate from these parameterizations, including varying amounts of mineral dust in convective systems measured during DC3 as well as an elevated real refractive index in biomass burning emissions sampled during SEAC<sup>4</sup>RS.

## 5.1 Overview of I-Neph Data Reduction and Error

A procedure for calibrating, deriving scattering matrix elements and estimating the resulting errors of an I-Neph has been described in Chapter 2. The base calibration procedure involves mapping the angular response of the camera and combining these results with polarimeter measurements to determine the polarization states of the input laser in the scattering plane coordinate system. Gasses are then sampled by the instrument and the known Rayleigh scattering signal is used to calibrate the radiometric response of the system. Scattering matrix elements can then be recovered from the measured intensities using the Equations 2.39 through 2.42 of Section 2.4. These equations take into account known instrument artifacts, including stray light contamination of the image and laser power variations at various stages of the measurement.

The dominant source of calibration error results from uncertainty in the  $q_n$  element of the stokes vector in the scattering plane coordinate system. Relatively simple formulas expressing this error in terms of only the scattering angle and corresponding scattering matrix elements were derived. The results showed relative errors that were generally on the order of 3% to 4%, when  $\sigma_q = 0.05$  was assumed. An empirical method was devised for estimating the time-dependent component of the uncertainty. The time-dependent errors vary significantly with aerosol loading but these errors are generally comparable to the  $q_n$  errors, producing total instrumental errors that are around 5%.

## 5.2 Concluding Remarks on Retrievals of I-Neph Data

The work described in Chapter 3 represents the first time that aerosol optical and microphysical properties were retrieved from airborne, polar nephelometer data. Additionally, the GRASP inversion of PI-Neph data makes fewer assumptions regarding the shape of the recovered size distribution and particle sphericity than previous in situ light scattering retrievals. The resulting products are in good agreement with expectations, and compare well with existing measurement techniques. Furthermore, the GRASP fit to PI-Neph data is consistent with the PI-Neph's level of error, indicating that the assumptions made in the retrieval are sufficient to faithfully reproduce the light scattering of realistic, fine mode dominated, natural aerosols.

The real refractive index of humidified salts retrieved with this method agree well with the predictions made by  $\kappa$ -Köhler theory and existing dry measurements. The PI-Neph retrieval of PSL refractive index agrees with other contemporary techniques to within the uncertainty present in those reported values. Furthermore, inversions of airborne SEAC<sup>4</sup>RS data produced refractive indices that were in good agreement with the existing literature.

There is significant spread in the aerosol size distribution measurements made by the OPCs, but the corresponding GRASP retrievals of PI-Neph data generally fall within the range of the existing measurements. A major part of the differences in the measured size distributions stem from the need to assume a refractive index during the calibration process. The GRASP retrieval of PI-Neph data has sufficient sensitivity to constrain the refractive index with enough accuracy to potentially reduce these biases. The fact that the PSD retrievals fell between the two UHSAS calibrations, in a manner consistent with the retrieved refractive index, supports this conclusion.

### 5.3 Summary of Geophysical Analysis

In Chapter 4 PI-Neph measurements from the DC3 and SEAC<sup>4</sup>RS field experiments were sub-selected and averaged over all periods corresponding to stable, high quality data. An optically independent aerosol typing scheme, making use of ancillary data, was developed and the resulting 2390 cases were separated into seven classified categories, as well as an eighth unclassified category corresponding to cases that did not meet any of the classification criteria. SEAC<sup>4</sup>RS measurements were separated into biogenic, biomass burning, urban and dust types, based on composition measurements from the PALMS instrument, APS data and the concentrations of various gas tracers. The geographic distribution of the resulting classification was in strong agreement with expectations suggesting a strong physical basis for the classification criteria. The DC3 dataset was divided into periods corresponding to the inflow of convective systems over one of three storm domains located in Colorado, Texas/Oklahoma and Alabama. 1307 cases were assigned to one of these seven categories and the remaining 1083 cases, not meeting any of the other classification criteria, were labeled as unclassified.

Phase function and  $-F_{12}/F_{11}$  data are averaged over each aerosol type to obtain scattering patterns characteristic of each classification. The dust category produced a significantly stronger forward scattering peak than all other types, likely driven by a coarse mode that contained a relatively large fraction of the total particle volume concentration. The next strongest forward peak was found in the CO storms, followed by the storms in TX/OK and then AL. There were very small differences in the scattering patterns of the SEAC<sup>4</sup>RS fine mode dominated aerosols. The largest differences between these types was observed in the peak values of  $-F_{12}/F_{11}$ , occurring around  $90^\circ$ , with the biomass burning cases being more strongly polarizing than the

other two types.

In order to more easily explore the scattering measurements, as well as further validate the optically independent aerosol typing scheme, principal component analysis was applied to the PI-Neph measurements and the results were examined as a function of aerosol type. The first few principal components of the  $F_{11}$  data and the first principal component of the  $-F_{12}/F_{11}$  data showed strong relationships with aerosol type. Two schemes were developed to divide the PCA score space into regions that predicted the result of the optically independent classification. The first of these schemes was based on the Mahalanobis distances between a given point and the center of the cluster corresponding to each aerosol type. The second scheme simply used a plane to divide the PCA score space into two regions corresponding to positive and negative classifications of a given type. In both schemes, individual cases were assigned to the correct category with very high accuracy and recall. This result both further supports the validity of the optically independent aerosol typing scheme and highlights the potential of using PI-Neph data to identify aerosol types. The characteristics producing the clear separation of aerosol types are very subtle and often rely on the relationships between many angles simultaneously. This fact emphasizes the value of scattering measurements composed of many sampling angles, as well as principal component analysis's ability to reveal the underlying patterns in these datasets.

The GRASP retrieval was applied to PI-Neph measurements to obtain aerosol microphysical and optical properties that are representative of each category. The progression observed in the scattering properties of the DC3 storm domains was also evident in the retrieved parameters. The magnitude of the retrieved coarse mode and the value of the real refractive index increased with the aridity of the storm domain. This result suggests that dry surface conditions may have permitted the corresponding

convective systems to loft more mineral dust particles into the atmosphere. The real refractive index of the biomass burning cases ( $n_{532nm} = 1.54$ ) was the only retrieved feature that significantly differentiated these particles from other fine mode dominated aerosols. Therefore, the distinct scattering properties consistently associated with the biomass burning type, evident in the PCA results, can be almost completely explained (at least within the context of GRASP's aerosol model) by an elevated real refractive index in the BB cases. The magnitude of the side scattering peak of  $-F_{12}/F_{11}$  was found to be the most sensitive scattering feature to these differences in refractive index. This fact supports the conclusion that polarimetric remote sensing can significantly improve our ability to accurately distinguish different fine mode aerosols from space [Mishchenko and Travis, 1997].

#### 5.4 Topics of Future Study

There are several instrumental enhancements that could significantly reduce the uncertainties associated with PI-Neph measurements. Variations in laser power could be more accurately corrected with addition of two high-quality, position insensitive reference detectors at the start and end of the laser's path, eliminating the need for the laser power corrections  $G$ ,  $\chi$  and  $\xi$ . The addition of a variable beam expander before the PI-Neph's sample chamber would permit the instrument operator to relatively easily increase the illuminated sample volume when particle sampling statistics are expected to be a problem. In conditions with low scattering strength, laser stray light is often the dominant source of error. Placing a proper spatial filter (including both lenses and a collimator) directly before the laser enters the sample chamber would help to reduce this background stray light. Lastly, future chamber based Imaging Nephelometers should strive to keep the orientation of the scattering plane constant

(i.e.  $\eta$  does not change with  $\theta$ ) across the entire length of the beam. This could be accomplished using custom optics, like those used in the OI-Neph, or by using two cameras placed at opposite ends of the chamber, instead of folding the laser beam.

There are also additional steps that could be taken in the data reduction process to improve data quality. During the Rayleigh calibration, the weakest scattering angles of the second image are very sensitive to the polarization state  $\vec{S}_{n,k}^{in\theta}$  of the laser. This sensitivity could potentially be exploited to better constrain the values of  $q_1$  and  $q_2$ . Another known relationship, that remains unexploited, is the fact that  $P_{13}(\theta) = P_{14}(\theta) = 0$  in the case of a macroscopically isotropic and mirror-symmetric scattering medium. Unavoidable artifacts of the instrument geometry and optical elements often produce significant  $u_n$  and  $v_n$  values that could be used, in conjunction with this assumption, to constrain the Rayleigh calibration slope, for example. Alternatively, these non-zero values of  $u_n$  and  $v_n$  could be used to test the underlying assumption of a macroscopically isotropic and mirror-symmetric scattering medium. In this case, the relationships of Equation 1.1 might yield insights as to whether the assumption of random orientation or mirror-symmetry was being violated. Lastly, the nearest neighbor assumption, used in calculating the products that are integrated over all  $\theta$  (i.e.  $\beta_{sca}$  and  $g$ ), could be significantly improved. Other potentially more accurate options that should be explored in future studies include stitching the Henyey-Greenstein [Thomas and Stamnes, 2002] or GRASP retrieved phase function to the extreme angles as well as the use of more complex methods like those described by Liu et al. [2003].

A few potential approaches to improving the uncertainty estimation are described in detail inside Section 2.5.3. In general, the equations of Section 2.4 and 2.3 need to be combined into two single equations for  $F_{11}$  and  $F_{12}$  and partial derivatives need to be taken with respect to all fundamental calibration variables. Alternatively,

a similar approach could be carried out numerically with a Monte Carlo simulation for a wide array of realistic  $F_{11}$  and  $F_{12}$  functions.

There were several aspects of the GRASP aerosol retrieval that should be explored further in future work. Aerosol absorption is a key parameter both to our understanding of climate as well as our interpretation of remote sensing data. The GRASP inversion of PI-Neph data has shown moderate sensitivity to absorption but a detailed assessment of the accuracy of this retrieved parameter is beyond the scope of this work and will have to remain the subject of future study. A better understanding of the accuracy of GRASP's retrieval of the imaginary part of the refractive index, with and without the inclusion of a traditional absorption measurement, may lead to useful insights into the absorption of ambient aerosols. Moreover, promising results were obtained regarding the retrieval of sphericity in the case of the humidified salts as well as in sensitivity studies, but because of the limited morphological information available in the SEAC<sup>4</sup>RS and DC3 datasets, a robust evaluation of this product is limited at this time.

It is not clear if the large GRASP residuals found in aerosols with significant coarse mode particle concentrations is driven entirely by the high relative noise produced from low scattering intensities or a fundamental inability of GRASP's aerosol model to capture the particle morphology. Additional angular scattering measurements of aerosols with high dust concentrations are needed to answer this question as well as potentially produce more reliable retrievals than those obtained for the dust category in this study. Numerical studies, involving retrievals of synthetic data corresponding to non-spherical particles with a wide array shapes, may also help shed light on this question.

Additional field measurements may help to more clearly illuminate the differences between the urban samples associated with population centers and aerosols

sampled near to the industrial sources present in the Ohio River Valley. It may also be possible to better characterize these differences by leveraging other measurements that were made during SEAC<sup>4</sup>RS, like particles size distributions and trace gas data.

There are a multitude of additional ways in which the existing I-Neph data could be leveraged to better understand of the strengths and weaknesses of existing aerosol models. New techniques quantifying the increase in aerosol scattering as a function of humidity, size resolved changes in particle diameter, and detailed measurements of particle growth in the laboratory [Orozco et al., 2016; Shingler et al., 2016] have made the conversion of dry aerosol properties (measured inside an aircraft) to ambient conditions much more reliable. These strategies could be applied to PI-Neph measurements to obtain ambient equivalent aerosol properties that are derived entirely from light scattering measurements. The resulting properties could be compared with existing models, like the aerosol models of Levy et al. [2007] that are used in the MODIS aerosol retrieval. The results could also be compared directly with AERONET to better understand the limitations of its retrieved aerosol properties. Additionally, while the current dataset is limited to measurements over Colorado's Front Range, measurements and retrievals of ambient particle properties from the OI-Neph compared with remote sensing variables, without the need for any hygroscopic growth corrections. The ability of I-Neph measurements to characterize an aerosol in such detail, purely through optical means, makes the resulting data extremely pertinent to remote sensing applications.

## Bibliography

- A. S. Ackerman, O. Toon, D. Stevens, A. Heymsfield, V. Ramanathan, and E. Welton. Reduction of tropical cloudiness by soot. *Science*, 288(5468):1042–1047, 2000.
- B. A. Albrecht. Aerosols, cloud microphysics, and fractional cloudiness. *Science*, 245(4923):1227–1231, 1989.
- T. Anderson and J. Ogren. Determining aerosol radiative properties using the TSI 3563 integrating nephelometer. *Aerosol Science and Technology*, 29:57–69, 1998.
- T. L. Anderson, D. S. Covert, S. F. Marshall, M. L. Laucks, R. J. Charlson, A. P. Waggoner, J. A. Ogren, R. Caldow, R. L. Holm, F. R. Quant, G. J. Sem, A. Wiedensohler, N. A. Ahlquist, and T. S. Bates. Performance Characteristics of a High-Sensitivity, Three-Wavelength Total Scattering/Backscatter Nephelometer. *Journal of Atmospheric and Oceanic Technology*, 13:967–986, 1996.
- A. Ångström. On the atmospheric transmission of sun radiation and on dust in the air. *Geografiska Annaler*, 11:156–166, 1929.
- K. B. Aptowicz, Y.-L. Pan, S. D. Martin, E. Fernandez, R. K. Chang, and R. G. Pinnick. Decomposition of atmospheric aerosol phase function by particle size and asphericity from measurements of single particle optical scattering patterns. *Journal of Quantitative Spectroscopy and Radiative Transfer*, apr 2013. ISSN 00224073. doi: 10.1016/j.jqsrt.2013.03.020.
- R. W. Atkinson, G. W. Fuller, H. R. Anderson, R. M. Harrison, and B. Armstrong. Urban ambient particle metrics and health: a time-series analysis. *Epidemiology*, 21(4):501–511, 2010.
- F. Auriol, J. Gayet, G. Feuvre, and O. Jourdan. In Situ Observation of Cirrus Scattering Phase Functions with 22 and 46 Halos : Cloud Field Study on 19 February 1998. *Journal of the Atmospheric Sciences*, 58(February 1998):3376–3390, 2001.
- B. Ayres, H. Allen, D. Draper, S. Brown, R. Wild, J. Jimenez, D. Day, P. Campuzano-Jost, W. Hu, J. d. Gouw, et al. Organic nitrate aerosol formation via no 3+

- biogenic volatile organic compounds in the southeastern united states. *Atmospheric Chemistry and Physics*, 15(23):13377–13392, 2015.
- N. Bacon and B. Swanson. Laboratory measurements of light scattering by single levitated ice crystals. *Journal of the atmospheric sciences*, 57:2094–2104, 2000.
- A. J. Baran, V. N. Shcherbakov, B. a. Baker, J. F. Gayet, and R. P. Lawson. On the scattering phase-function of non-symmetric ice-crystals. *Quarterly Journal of the Royal Meteorological Society*, 131(611):2609–2616, oct 2005. ISSN 00359009. doi: 10.1256/qj.04.137.
- B. Barkey, S. E. Paulson, and A. Chung. Genetic Algorithm Inversion of Dual Polarization Polar Nephelometer Data to Determine Aerosol Refractive Index. *Aerosol Science and Technology*, 41(8):751–760, 2007. ISSN 0278-6826. doi: 10.1080/02786820701432640.
- B. Barkey, H. Kim, and S. E. Paulson. Genetic Algorithm Retrieval of Real Refractive Index from Aerosol Distributions that are not Lognormal. *Aerosol Science and Technology*, 44(12):1089–1095, 2010. ISSN 0278-6826. doi: 10.1080/02786826.2010.512025.
- M. C. Barth, C. A. Cantrell, W. H. Brune, S. A. Rutledge, J. H. Crawford, H. Huntrieser, L. D. Carey, D. MacGorman, M. Weisman, K. E. Pickering, E. Bruning, B. Anderson, E. Apel, M. Biggerstaff, T. Campos, P. Campuzano-Jost, R. Cohen, J. Crouse, D. A. Day, G. Diskin, F. Flocke, A. Fried, C. Garland, B. Heikes, S. Honomichl, R. Hornbrook, L. G. Huey, J. L. Jimenez, T. Lang, M. Lichtenstern, T. Mikoviny, B. Nault, D. O’Sullivan, L. L. Pan, J. Peischl, I. Pollack, D. Richter, D. Riemer, T. Ryerson, H. Schlager, J. St. Clair, J. Walega, P. Weibring, A. Weinheimer, P. Wennberg, A. Wisthaler, P. J. Wooldridge, and C. Ziegler. The Deep Convective Clouds and Chemistry (DC3) Field Campaign. *Bulletin of the American Meteorological Society*, 96(8):1281–1309, 2015. ISSN 0003-0007. doi: 10.1175/BAMS-D-13-00290.1.
- J. Bateman, E. Weneck, and D. Eshler. Determination of particle size and concentration from spectrophotometric transmission. *Journal of Colloid Science*, 14(3): 308–329, 1959. ISSN 00958522. doi: 10.1016/0095-8522(59)90055-8.
- T. S. Bates, T. L. Anderson, T. Baynard, T. Bond, O. Boucher, G. Carmichael, a. Clarke, C. Erlick, H. Guo, L. Horowitz, S. Howell, S. Kulkarni, H. Maring, a. McComiskey, a. Middlebrook, K. Noone, C. D. O’Dowd, J. Ogren, J. Penner, P. K. Quinn, a. R. Ravishankara, D. L. Savoie, S. E. Schwartz, Y. Shinozuka, Y. Tang, R. J. Weber, and Y. Wu. Aerosol direct radiative effects over the northwest Atlantic, northwest Pacific, and North Indian Oceans: estimates based on in-situ chemical and optical measurements and chemical transport modeling. *Atmospheric*

- Chemistry and Physics Discussions*, 6(1):175–362, jan 2006. ISSN 1680-7375. doi: 10.5194/acpd-6-175-2006.
- D. Baumgardner, J. E. Dye, B. W. Gandrud, and R. G. Knollenberg. Interpretation of measurements made by the forward scattering spectrometer probe (fssp-300) during the airborne arctic stratospheric expedition. *Journal of Geophysical Research: Atmospheres*, 97(D8):8035–8046, 1992. ISSN 2156-2202. doi: 10.1029/91JD02728.
- D. Baumgardner, H. Jonsson, W. Dawson, D. O’Connor, and R. Newton. The cloud, aerosol and precipitation spectrometer: a new instrument for cloud investigations. *Atmospheric research*, 59:251–264, 2001.
- D. Baumgardner, J. Brenguier, A. Bucholtz, H. Coe, P. DeMott, T. J. Garrett, J. Gayet, M. Hermann, A. Heymsfield, A. Korolev, et al. Airborne instruments to measure atmospheric aerosol particles, clouds and radiation: A cook’s tour of mature and emerging technology. *Atmospheric Research*, 102(1):10–29, 2011.
- D. Baumgardner, R. Newton, M. Krmer, J. Meyer, A. Beyer, M. Wendisch, and P. Vochezer. The cloud particle spectrometer with polarization detection (cpspd): A next generation open-path cloud probe for distinguishing liquid cloud droplets from ice crystals. *Atmospheric Research*, 142:2 – 14, 2014. ISSN 0169-8095. doi: <http://dx.doi.org/10.1016/j.atmosres.2013.12.010>. The 16th International Conference on Clouds and Precipitation.
- A. E. Beaton and J. W. Tukey. The Fitting of Power Series, Meaning Polynomials, Illustrated on Band-Spectroscopic Data. *Technometrics*, 16(2):147–185, 1974. ISSN 00401706. doi: 10.2307/1267936.
- N. Bellouin, O. Boucher, J. Haywood, and M. S. Reddy. Global estimate of aerosol direct radiative forcing from satellite measurements. *Nature*, 438(7071):1138–1141, 2005.
- J. R. Bence. Analysis of Short Time Series: Correcting for Autocorrelation. *Ecology*, 76(2):628–639, 1995. ISSN 00129658. doi: 10.2307/1941218.
- Y. Bian, C. Zhao, W. Xu, G. Zhao, J. Tao, and Y. Kuang. Development and validation of a ccd-laser aerosol detective system for measuring the ambient aerosol phase function. *Atmospheric Measurement Techniques*, 10(6):2313–2322, 2017. doi: 10.5194/amt-10-2313-2017.
- M. Bilal, J. E. Nichol, M. P. Bleiweiss, and D. Dubois. A Simplified high resolution MODIS aerosol retrieval algorithm (SARA) for use over mixed surfaces. *Remote Sensing of Environment*, 136:135–145, 2013. ISSN 00344257. doi: 10.1016/j.rse.2013.04.014.

- T. C. Bond, D. S. Covert, and T. Müller. Truncation and Angular-Scattering Corrections for Absorbing Aerosol in the TSI 3563 Nephelometer. *Aerosol Science and Technology*, 43(9):866–871, aug 2009. ISSN 0278-6826. doi: 10.1080/02786820902998373.
- A. G. Borovoi and I. A. Grishin. Scattering matrices for large ice crystal particles. *JOSA A*, 20(11):2071–2080, 2003.
- S. Burton, R. Ferrare, C. Hostetler, J. Hair, R. Rogers, M. Obland, C. Butler, A. Cook, D. Harper, and K. Froyd. Aerosol classification using airborne high spectral resolution lidar measurements-methodology and examples. *Atmospheric Measurement Techniques*, 5(1):73, 2012.
- J. C. Cabada. Light scattering by fine particles during the Pittsburgh Air Quality Study: Measurements and modeling. *Journal of Geophysical Research*, 109(D16):D16S03, 2004. ISSN 0148-0227. doi: 10.1029/2003JD004155.
- Y. Cai, D. C. Montague, W. Mooiweer-Bryan, and T. Deshler. Performance characteristics of the ultra high sensitivity aerosol spectrometer for particles between 55 and 800 nm: Laboratory and field studies. *Journal of Aerosol Science*, 39(9):759–769, 2008. ISSN 00218502. doi: 10.1016/j.jaerosci.2008.04.007.
- B. Cairns, L. Travis, and E. Russell. The research scanning polarimeter: calibration and ground-based measurements. In *Proc. SPIE*, volume 3754, pages 186–196, 1999.
- A. Carlton, C. Wiedinmyer, and J. Kroll. A review of secondary organic aerosol (soa) formation from isoprene. *Atmospheric Chemistry and Physics*, 9(14):4987–5005, 2009.
- J.-L. Castagner and I. J. Bigio. Particle sizing with a fast polar nephelometer. *Applied optics*, 46(4):527–32, feb 2007. ISSN 0003-6935.
- R. K. Chakrabarty, H. Moosmüller, W. P. Arnott, M. A. Garro, J. G. Slowik, E. S. Cross, J.-H. Han, P. Davidovits, T. B. Onasch, and D. R. Worsnop. Light scattering and absorption by fractal-like carbonaceous chain aggregates: Comparison of theories and experiment. *Applied optics*, 46(28):6990–7006, 2007.
- S. Chamberlain-Ward and F. Sharp. Advances in nephelometry through the Ecotech Aurora nephelometer. *TheScientificWorldJournal*, 11:2530–5, jan 2011. ISSN 1537-744X. doi: 10.1100/2011/310769.
- R. J. Charlson, N. C. Ahlquist, H. Selvidge, and P. B. MacCready. Monitoring of Atmospheric Aerosol Parameters with the Integrating Nephelometer. *Journal of the Air Pollution Control Association*, 19(12):937–942, dec 1969. ISSN 0002-2470. doi: 10.1080/00022470.1969.10469360.

- R. J. Charlson, J. Langner, H. Rodhe, C. Leovy, and S. Warren. Perturbation of the northern hemisphere radiative balance by backscattering from anthropogenic sulfate aerosols. *Tellus A*, 43(4):152–163, 1991.
- C. Chou, P. Formenti, M. Maille, P. Ausset, G. Helas, M. Harrison, and S. Osborne. Size distribution, shape, and composition of mineral dust aerosols collected during the african monsoon multidisciplinary analysis special observation period 0: Dust and biomass-burning experiment field campaign in niger, january 2006. *Journal of Geophysical Research: Atmospheres*, 113(D23):n/a–n/a, 2008. ISSN 2156-2202. doi: 10.1029/2008JD009897. D00C10.
- D. A. Chu, R. Ferrare, J. Szykman, J. Lewis, A. Scarino, J. Hains, S. Burton, G. Chen, T. Tsai, C. Hostetler, et al. Regional characteristics of the relationship between columnar aod and surface pm 2.5: Application of lidar aerosol extinction profiles over baltimore–washington corridor during discover-aq. *Atmospheric Environment*, 101:338–349, 2015.
- P. Chylek and J. Wong. Effect of absorbing aerosols on global radiation budget. *Geophysical research letters*, 22(8):929–931, 1995.
- J. A. Coakley Jr, R. D. Cess, and F. B. Yurevich. The effect of tropospheric aerosols on the earth’s radiation budget: A parameterization for climate models. *Journal of the Atmospheric Sciences*, 40(1):116–138, 1983.
- S. Colak, C. Yeh, and L. W. Casperson. Scattering of focused beams by tenuous particles. *Applied optics*, 18(3):294–302, 1979.
- C. A. Corr, L. D. Ziemba, E. Scheuer, B. E. Anderson, A. J. Beyersdorf, G. Chen, E. Crosbie, R. H. Moore, M. Shook, K. L. Thornhill, E. Winstead, R. P. Lawson, M. C. Barth, J. R. Schroeder, D. R. Blake, and J. E. Dibb. Observational evidence for the convective transport of dust over the central united states. *Journal of Geophysical Research: Atmospheres*, 121(3):1306–1319, 2016. ISSN 2169-8996. doi: 10.1002/2015JD023789. 2015JD023789.
- A. W. Correia, C. A. Pope III, D. W. Dockery, Y. Wang, M. Ezzati, and F. Dominici. The effect of air pollution control on life expectancy in the united states: an analysis of 545 us counties for the period 2000 to 2007. *Epidemiology (Cambridge, Mass.)*, 24(1):23, 2013.
- D. B. Curtis, B. Meland, M. Aycibin, N. P. Arnold, V. H. Grassian, M. A. Young, and P. D. Kleiber. A laboratory investigation of light scattering from representative components of mineral dust aerosol at a wavelength of 550 nm. *Journal of Geophysical Research: Atmospheres*, 113(D8):n/a–n/a, 2008. ISSN 2156-2202. doi: 10.1029/2007JD009387. D08210.

- J. Deuzé, F. Bréon, C. Devaux, P. Goloub, M. Herman, B. Lafrance, F. Maignan, A. Marchand, F. Nadal, G. Perry, et al. Remote sensing of aerosols over land surfaces from polder-adeos-1 polarized measurements. *Journal of Geophysical Research: Atmospheres*, 106(D5):4913–4926, 2001.
- W. D. Dick, P. J. Ziemann, and P. H. McMurry. Multiangle Light-Scattering Measurements of Refractive Index of Submicron Atmospheric Particles. *Aerosol Science and Technology*, 41(5):549–569, apr 2007. ISSN 0278-6826. doi: 10.1080/02786820701272012.
- D. Diner, F. Xu, M. Garay, J. Martonchik, B. Rheingans, S. Geier, A. Davis, B. Hancock, V. Jovanovic, M. Bull, et al. The airborne multiangle spectropolarimetric imager (airmspi): a new tool for aerosol and cloud remote sensing. *Atmospheric Measurement Techniques*, 6(8):2007, 2013.
- D. J. Diner, J. C. Beckert, T. H. Reilly, C. J. Bruegge, J. E. Conel, R. A. Kahn, J. V. Martonchik, T. P. Ackerman, R. Davies, S. A. Gerstl, et al. Multi-angle imaging spectroradiometer (misr) instrument description and experiment overview. *IEEE Transactions on Geoscience and Remote Sensing*, 36(4):1072–1087, 1998.
- G. Dolgos and J. V. Martins. Polarized Imaging Nephelometer for in situ airborne measurements of aerosol light scattering. *Optics Express*, 22(18):21972–21990, sep 2014. ISSN 1094-4087. doi: 10.1364/OE.22.021972.
- O. Dubovik. Optimization of Numerical Inversion in Photopolarimetric Remote Sensing. *Photopolarimetry in Remote Sensing*, pages 65–106, 2004. doi: 10.1007/1-4020-2368-5\_3.
- O. Dubovik and M. King. A flexible inversion algorithm for retrieval of aerosol optical properties from Sun and sky radiance measurements. *Journal of Geophysical Research*, 105:20,673–20,696, 2000.
- O. Dubovik, a. Smirnov, B. N. Holben, M. D. King, Y. J. Kaufman, T. F. Eck, and I. Slutsker. Accuracy assessments of aerosol optical properties retrieved from Aerosol Robotic Network (AERONET) Sun and sky radiance measurements. *Journal of Geophysical Research: Atmospheres*, 105(D8):9791–9806, apr 2000. ISSN 01480227. doi: 10.1029/2000JD900040.
- O. Dubovik, B. Holben, T. Eck, A. Smirnov, Y. Kaufman, and M. King. Variability of absorption and optical properties of key aerosol types observed in worldwide locations. *Journal of the Atmospheric Sciences*, 59:590–608, 2002.
- O. Dubovik, A. Sinyuk, T. Lapyonok, B. N. Holben, M. Mishchenko, P. Yang, T. F. Eck, H. Volten, O. Muñoz, B. Veihelmann, W. J. van der Zande, J.-F. Leon, M. Sorokin, and I. Slutsker. Application of spheroid models to account for aerosol

- particle nonsphericity in remote sensing of desert dust. *Journal of Geophysical Research*, 111(D11):D11208, 2006. ISSN 0148-0227. doi: 10.1029/2005JD006619.
- O. Dubovik, M. Herman, a. Holdak, T. Lapyonok, D. Tanré, J. L. Deuzé, F. Ducos, a. Sinyuk, and a. Lopatin. Statistically optimized inversion algorithm for enhanced retrieval of aerosol properties from spectral multi-angle polarimetric satellite observations. *Atmospheric Measurement Techniques*, 4(5):975–1018, 2011. ISSN 1867-8548. doi: 10.5194/amt-4-975-2011.
- O. Dubovik, T. Lapyonok, P. Litvinov, M. Herman, D. Fuertes, F. Ducos, B. Torres, Y. Derimian, X. Huang, A. Lopatin, A. Chaikovsky, M. Aspetsberger, and C. Federspiel. GRASP: a versatile algorithm for characterizing the atmosphere. *SPIE Newsroom*, pages 2–5, 2014. ISSN 18182259. doi: 10.1117/2.1201408.005558.
- T. F. Eck, B. N. Holben, J. S. Reid, A. Arola, R. A. Ferrare, C. A. Hostetler, S. N. Crumeyrolle, T. A. Berkoff, E. J. Welton, S. Lolli, A. Lyapustin, Y. Wang, J. S. Schafer, D. M. Giles, B. E. Anderson, K. L. Thornhill, P. Minnis, K. E. Pickering, C. P. Loughner, A. Smirnov, and A. Sinyuk. Observations of rapid aerosol optical depth enhancements in the vicinity of polluted cumulus clouds. *Atmospheric Chemistry and Physics*, 14(21):11633–11656, 2014. doi: 10.5194/acp-14-11633-2014.
- R. Eiden. The elliptical polarization of light scattered by a volume of atmospheric air. *Applied optics*, 5(4):569–75, 1966. ISSN 0003-6935.
- C. Erlick, J. P. D. Abbatt, and Y. Rudich. How Different Calculations of the Refractive Index Affect Estimates of the Radiative Forcing Efficiency of Ammonium Sulfate Aerosols. *Journal of the Atmospheric Sciences*, 68(9):1845–1852, 2011. ISSN 0022-4928. doi: 10.1175/2011JAS3721.1.
- W. R. Espinosa, L. A. Remer, O. Dubovik, L. Ziemba, A. Beyersdorf, D. Orozco, G. Schuster, T. Lapyonok, D. Fuertes, and J. V. Martins. Retrievals of aerosol optical and microphysical properties from imaging polar nephelometer scattering measurements. *Atmospheric Measurement Techniques*, 10(3):811, 2017.
- R. Esworthy. Air quality: Epas 2013 changes to the particulate matter (pm) standard. *Congressional Research Service*, pages 7–5700, 2013.
- Y. Fang, V. Naik, L. Horowitz, and D. Mauzerall. Air pollution and associated human mortality: the role of air pollutant emissions, climate change and methane concentration increases from the preindustrial period to present. *Atmospheric Chemistry and Physics*, 13(3):1377–1394, 2013.
- R. W. Fenn, S. a. Clough, W. O. Gallery, R. E. Good, F. X. Kneizys, J. Mill, L. Rothman, E. Shettle, and F. Volz. Optical and Infrared Properties of the Atmosphere. In *Handbook of Geophysics and the Space Environment*, chapter 18. NTIS, 1985. ISBN 9780521269827.

- A. Fried, G. Diskin, P. Weibring, D. Richter, J. Walega, G. Sachse, T. Slate, M. Rana, and J. Podolske. Tunable infrared laser instruments for airborne atmospheric studies. *Applied Physics B*, 92(3):409–417, 2008.
- J. Gayet, O. Crépel, J. Fournol, and S. Oshchepkov. A new airborne polar Nephelometer for the measurements of optical and microphysical cloud properties. Part I : Theoretical design. *Annales Geophysicae*, 15:451–459, 1997.
- J. Gayet, F. Auriol, S. Oshchepkov, F. Schroder, C. Duroure, G. Febvre, J. Fournol, O. Crepel, P. Personne, and D. Daugereon. In situ measurements of the scattering phase function of stratocumulus, contrails and cirrus. *Geophysical Research Letters*, 25(7):971–974, 1998.
- D. M. Giles, B. N. Holben, T. F. Eck, A. Sinyuk, A. Smirnov, I. Slutsker, R. R. Dickerson, A. M. Thompson, and J. S. Schafer. An analysis of aeronet aerosol absorption properties and classifications representative of aerosol source regions. *Journal of Geophysical Research: Atmospheres*, 117(D17):n/a–n/a, 2012. ISSN 2156-2202. doi: 10.1029/2012JD018127. D17203.
- A. Glen and S. Brooks. A new method for measuring optical scattering properties of atmospherically relevant dusts using the cloud and aerosol spectrometer with polarization (caspol). *Atmospheric Chemistry and Physics*, 13(3):1345–1356, 2013.
- G. Grams, A. Dascher, and C. Wymna. Laser Polar Nephelometer for Airborne Measurements of Aerosol Optical Properties. *Optical Engineering*, 14(1):85–90, 1975.
- G. M. Hale and M. R. Querry. Optical Constants of Water in the 200-nm to 200-microm Wavelength Region. *Applied optics*, 12(3):555–563, 1973. ISSN 0003-6935. doi: 10.1364/AO.12.000555.
- M. Hallquist, J. Wenger, U. Baltensperger, Y. Rudich, D. Simpson, M. Claeys, J. Dommen, N. Donahue, C. George, A. Goldstein, et al. The formation, properties and impact of secondary organic aerosol: current and emerging issues. *Atmospheric Chemistry and Physics*, 9(14):5155–5236, 2009.
- P. Hamill, M. Giordano, C. Ward, D. Giles, and B. Holben. An aeronet-based aerosol classification using the mahalanobis distance. *Atmospheric Environment*, 140:213 – 233, 2016. ISSN 1352-2310. doi: <http://dx.doi.org/10.1016/j.atmosenv.2016.06.002>.
- J. Hansen, M. Sato, and R. Ruedy. Radiative forcing and climate response. *Journal of Geophysical Research: Atmospheres*, 102(D6):6831–6864, 1997.
- J. E. Hansen and L. D. Travis. Light scattering in planetary atmospheres. *Space science reviews*, 16(4):527–610, 1974.

- J. Heintzenberg and R. Charlson. Design and Application of the Integrating Nephelometer: A Review. *Journal of Atmospheric and Oceanic Technology*, 13:987–1000, 1996.
- W. C. Hinds. *Aerosol Technology: Properties, Behavior, and Measurement of Airborne Particles*. Wiley, 1999. ISBN 978-0-471-19410-1.
- R. M. Hoff and S. A. Christopher. Remote sensing of particulate pollution from space: have we reached the promised land? *Journal of the Air & Waste Management Association*, 59(6):645–675, 2009.
- B. N. Holben, T. Eck, I. Slutsker, D. Tanre, J. Buis, A. Setzer, E. Vermote, J. Reagan, Y. Kaufman, T. Nakajima, et al. Aeroneta federated instrument network and data archive for aerosol characterization. *Remote sensing of environment*, 66(1):1–16, 1998.
- a. C. Holland and J. S. Draper. Analytical and experimental investigation of light scattering from polydispersions of Mie particles. *Applied optics*, 6(3):511–8, mar 1967. ISSN 0003-6935.
- A. Hunt and D. Huffman. A new polarization modulated light scattering instrument. *Review of Scientific Instruments*, 1973.
- M. Z. Jacobson. Strong radiative heating due to the mixing state of black carbon in atmospheric aerosols. *Nature*, 409(6821):695, 2001.
- M.-J. Jeong and Z. Li. Separating real and apparent effects of cloud, humidity, and dynamics on aerosol optical thickness near cloud edges. *Journal of Geophysical Research: Atmospheres*, 115(D7):n/a–n/a, 2010. ISSN 2156-2202. doi: 10.1029/2009JD013547. D00K32.
- M. R. Jones, K. H. Leong, M. Q. Brewster, and B. P. Curry. Inversion of light-scattering measurements for particle size and optical constants: experimental study. *Applied optics*, 33(18):4035–4041, 1994. ISSN 0003-6935. doi: 10.1364/AO.33.004035.
- S. H. Jones, M. D. King, and A. D. Ward. Determining the unique refractive index properties of solid polystyrene aerosol using broadband Mie scattering from optically trapped beads. *Physical chemistry chemical physics : PCCP*, 15(47):20735–41, 2013. ISSN 1463-9084. doi: 10.1039/c3cp53498g.
- R. A. Kahn and B. J. Gaitley. An analysis of global aerosol type as retrieved by misr. *Journal of Geophysical Research: Atmospheres*, 120(9):4248–4281, 2015. ISSN 2169-8996. doi: 10.1002/2015JD023322. 2015JD023322.

- W. Kaller. A new polar nephelometer for measurement of atmospheric aerosols. *Journal of Quantitative Spectroscopy and Radiative Transfer*, 87(2):107–117, aug 2004. ISSN 00224073. doi: 10.1016/j.jqsrt.2003.12.018.
- P. Kaye, E. Hirst, J. Clark, and F. Micheli. Airborne Particle-Shape and Size Classification from Spatial Light-Scattering Profiles. *Journal of Aerosol Science*, 23(6): 597–611, 1992.
- K. A. Koehler, S. M. Kreidenweis, P. J. DeMott, A. J. Prenni, C. M. Carrico, B. Ervens, and G. Feingold. Water activity and activation diameters from hygroscopicity data - Part II: Application to organic species. *Atmospheric Chemistry and Physics Discussions*, 5(5):10881–10924, 2006. ISSN 1680-7324. doi: 10.5194/acpd-5-10881-2005.
- a. V. Korolev, E. F. Emery, J. W. Strapp, S. G. Cober, G. a. Isaac, M. Wasey, and D. Marcotte. Small Ice Particles in Tropospheric Clouds: Fact or Artifact? Airborne Icing Instrumentation Evaluation Experiment. *Bulletin of the American Meteorological Society*, 92(8):967–973, aug 2011. ISSN 0003-0007. doi: 10.1175/2010BAMS3141.1.
- J. Lee, J. Kim, P. Yang, and N. C. Hsu. Improvement of aerosol optical depth retrieval from MODIS spectral reflectance over the global ocean using new aerosol models archived from AERONET inversion data and tri-axial ellipsoidal dust database. *Atmospheric Chemistry and Physics*, 12(15):7087–7102, 2012. ISSN 16807316. doi: 10.5194/acp-12-7087-2012.
- S.-H. Lee, D. M. Murphy, D. S. Thomson, and A. M. Middlebrook. Chemical components of single particles measured with particle analysis by laser mass spectrometry (palm) during the atlanta supersite project: Focus on organic/sulfate, lead, soot, and mineral particles. *Journal of Geophysical Research: Atmospheres*, 107(D1), 2002.
- T. E. Lee, S. D. Miller, F. J. Turk, C. Schueler, R. Julian, S. Deyo, P. Dills, and S. Wang. The npoess viirs day/night visible sensor. *Bulletin of the American Meteorological Society*, 87(2):191–199, 2006.
- M. Legrand, O. Dubovik, T. Lapyonok, and Y. Derimian. Accounting for particle nonsphericity in modeling of mineral dust radiative properties in the thermal infrared. *Journal of Quantitative Spectroscopy and Radiative Transfer*, 149:219 – 240, 2014. ISSN 0022-4073. doi: <http://dx.doi.org/10.1016/j.jqsrt.2014.07.014>.
- K. Leong and M. Jones. Design and Test of Polar Nephelometer. *Aerosol science and technology*, 23:341–356, 1995.

- R. C. Levy, L. A. Remer, and O. Dubovik. Global aerosol optical properties and application to Moderate Resolution Imaging Spectroradiometer aerosol retrieval over land. *Journal of Geophysical Research Atmospheres*, 112(13):1–15, 2007. ISSN 01480227. doi: 10.1029/2006JD007815.
- R. C. Levy, L. A. Munchak, S. Mattoo, F. Patadia, L. A. Remer, and R. E. Holz. Towards a long-term global aerosol optical depth record: Applying a consistent aerosol retrieval algorithm to MODIS and VIIRS-observed reflectance. *Atmospheric Measurement Techniques*, 8(10):4083–4110, 2015. ISSN 18678548. doi: 10.5194/amt-8-4083-2015.
- J. Li and J. T. Mao. Properties of Atmospheric Aerosols Inverted from Optical Remote-Sensing. *Atmospheric Environment Part a-General Topics*, 24(9):2517–2522, 1990. ISSN 00046981.
- B. R. Lienert, J. N. Porter, and S. K. Sharma. Aerosol size distribution from genetic inversion of polar nephelometer data. *Journal of Atmospheric and Oceanic Technology*, 20(10):1403–1410, 2003. ISSN 0739-0572. doi: 10.1175/1520-0426(2003)020<1403:ASDFGI>2.0.CO;2.
- L. Liu, M. I. Mishchenko, J. W. Hovenier, H. Volten, and O. Muñoz. Scattering matrix of quartz aerosols: comparison and synthesis of laboratory and lorenz-mie results. *Journal of Quantitative Spectroscopy and Radiative Transfer*, 79:911–920, 2003.
- Y. Liu and D. J. Diner. Multi-angle imager for aerosols: A satellite investigation to benefit public health. *Public Health Reports*, 132(1):14–17, 2017.
- Y. Liu, J. A. Sarnat, V. Kilaru, D. J. Jacob, and P. Koutrakis. Estimating ground-level pm<sub>2.5</sub> in the eastern united states using satellite remote sensing. *Environmental science & technology*, 39(9):3269–3278, 2005.
- J. Löndahl, J. Pagels, E. Swietlicki, J. Zhou, M. Ketzel, A. Massling, and M. Bohgard. A set-up for field studies of respiratory tract deposition of fine and ultrafine particles in humans. *Journal of Aerosol Science*, 37(9):1152–1163, 2006.
- X. Ma, J. Q. Lu, R. S. Brock, K. M. Jacobs, P. Yang, and X.-H. Hu. Determination of complex refractive index of polystyrene microspheres from 370 to 1610 nm. *Physics in Medicine and Biology*, 48(24):4165–4172, 2003. ISSN 0031-9155. doi: 10.1088/0031-9155/48/24/013.
- W. C. Malm and S. M. Kreidenweis. The effects of models of aerosol hygroscopicity on the apportionment of extinction. *Atmospheric Environment*, 31(13):1965–1976, 1997.

- T. Marbach, P. Phillips, and P. Schlüssel. 3mi: The multi-viewing multi-channel multi-polarization imaging mission of the eumetsat polar system-second generation (eps-sg) dedicated to aerosol characterization. In *AIP Conference Proceedings*, volume 1531, pages 344–347. AIP, 2013.
- H. Maring, D. Savoie, M. Izaguirre, L. Custals, and J. Reid. Mineral dust aerosol size distribution change during atmospheric transport. *Journal of Geophysical Research: Atmospheres*, 108(D19), 2003.
- J. V. Martins, P. V. Hobbs, R. E. Weiss, and P. Artaxo. Sphericity and morphology of smoke particles from biomass burning in brazil. *Journal of Geophysical Research: Atmospheres*, 103(D24):32051–32057, 1998. ISSN 2156-2202. doi: 10.1029/98JD01153.
- R. A. McCormick and J. H. Ludwig. Climate modification by atmospheric aerosols. *Science*, 156(3780):1358–1359, 1967.
- G. J. McLachlan. *Discriminant Analysis and Statistical Pattern Recognition*. Wiley, 2004.
- C. S. McNaughton, A. D. Clarke, S. G. Howell, M. Pinkerton, B. Anderson, L. Thornhill, C. Hudgins, E. Winstead, J. E. Dibb, E. Scheuer, and H. Maring. Results from the DC-8 Inlet Characterization Experiment (DICE): Airborne Versus Surface Sampling of Mineral Dust and Sea Salt Aerosols. *Aerosol Science and Technology*, 41(2):136–159, 2007. ISSN 0278-6826. doi: 10.1080/02786820601118406.
- K. Meister, C. Johansson, and B. Forsberg. Estimated short-term effects of coarse particles on daily mortality in stockholm, sweden. *Environmental health perspectives*, 120(3):431, 2012.
- T. Mikoviny, L. Kaser, and A. Wisthaler. Development and characterization of a high-temperature proton-transfer-reaction mass spectrometer (ht-ptr-ms). *Atmospheric Measurement Techniques*, 3(3):537–544, 2010.
- M. I. Mishchenko and L. D. Travis. Satellite retrieval of aerosol properties over the ocean using polarization as well as intensity of reflected sunlight. *Journal of Geophysical Research: Atmospheres*, 102(D14):16989–17013, 1997. ISSN 2156-2202. doi: 10.1029/96JD02425.
- M. I. Mishchenko, L. D. Travis, and A. A. Lacis. *Scattering, absorption, and emission of light by small particles*. Cambridge university press, 2002.
- M. I. Mishchenko, B. Cairns, J. E. Hansen, L. D. Travis, R. Burg, Y. J. Kaufman, J. V. Martins, and E. P. Shettle. Monitoring of aerosol forcing of climate from space: analysis of measurement requirements. *Journal of Quantitative Spectroscopy and Radiative Transfer*, 88(1):149–161, 2004.

- M. I. Mishchenko, B. Cairns, J. E. Hansen, L. D. Travis, G. Kopp, C. F. Schueler, B. a. Fafaul, R. J. Hooker, H. B. Maring, and T. Itchkawich. Accurate Monitoring of Terrestrial Aerosols and Total Solar Irradiance: Introducing the Glory Mission. *Bulletin of the American Meteorological Society*, 88(5):677–691, may 2007. ISSN 0003-0007. doi: 10.1175/BAMS-88-5-677.
- M. I. Mishchenko, I. V. Geogdzhayev, L. Liu, A. A. Lacis, B. Cairns, and L. D. Travis. Toward unified satellite climatology of aerosol properties: What do fully compatible MODIS and MISR aerosol pixels tell us? *Journal of Quantitative Spectroscopy and Radiative Transfer*, 110:402–408, apr 2009. ISSN 00224073.
- T. Müller, M. Laborde, G. Kassell, and a. Wiedensohler. Design and performance of a three-wavelength LED-based total scatter and backscatter integrating nephelometer. *Atmospheric Measurement Techniques*, 4(6):1291–1303, jun 2011. ISSN 1867-8548. doi: 10.5194/amt-4-1291-2011.
- O. Muñoz, F. Moreno, D. Guirado, J. L. Ramos, H. Volten, and J. W. Hovenier. The IAA cosmic dust laboratory: Experimental scattering matrices of clay particles. *Icarus*, 211(1):894–900, 2011. ISSN 00191035. doi: 10.1016/j.icarus.2010.10.027.
- G. Myhre, B. Samset, M. Schulz, Y. Balkanski, S. Bauer, T. Berntsen, H. Bian, N. Bellouin, M. Chin, T. Diehl, et al. Radiative forcing of the direct aerosol effect from aerocom phase ii simulations. *Atmospheric Chemistry and Physics*, 13(4): 1853, 2013.
- R. Nessler, E. Weingartner, and U. Baltensperger. Adaptation of dry nephelometer measurements to ambient conditions at the Jungfraujoch. *Environmental Science and Technology*, 39(7):2219–2228, 2005. ISSN 0013936X. doi: 10.1021/es035450g.
- C. D. O’Dowd, M. H. Smith, I. E. Consterdine, and J. A. Lowe. Marine aerosol, sea-salt, and the marine sulphur cycle: A short review. *Atmospheric Environment*, 31(1):73–80, 1997.
- A. H. Omar, J. G. Won, D. M. Winker, S. C. Yoon, O. Dubovik, and M. P. McCormick. Development of global aerosol models using cluster analysis of Aerosol Robotic Network (AERONET) measurements. *Journal of Geophysical Research D: Atmospheres*, 110(10):1–14, 2005. ISSN 01480227. doi: 10.1029/2004JD004874.
- D. Orozco, A. J. Beyersdorf, L. D. Ziemba, T. Berkoff, Q. Zhang, R. Delgado, C. J. Hennigan, K. Thornhill, D. E. Young, C. Parworth, H. Kim, and R. M. Hoff. Hygroscopicity Measurements of Aerosol Particles in the San Joaquin Valley, CA, Baltimore, MD, and Golden, CO. *Journal of Geophysical Research: Atmospheres*, 121:7344–7359, 2016. ISSN 2169897X. doi: 10.1002/2015JD023971.

- J. a. Pena, J. M. Norman, and D. W. Thomson. Isokinetic Sampler for Continuous Airborne Aerosol Measurements. *Journal of the Air Pollution Control Association*, 27(4):337–341, apr 1977. ISSN 0002-2470. doi: 10.1080/00022470.1977.10470428.
- D. A. Peterson, E. J. Hyer, J. R. Campbell, M. D. Fromm, J. W. Hair, C. F. Butler, and M. A. Fenn. The 2013 rim fire: Implications for predicting extreme fire spread, pyroconvection, and smoke emissions. *Bulletin of the American Meteorological Society*, 96(2):229–247, 2015.
- A. Petroff, A. Mailliat, M. Amiellh, and F. Anselmet. Aerosol dry deposition on vegetative canopies. part i: Review of present knowledge. *Atmospheric Environment*, 42(16):3625–3653, 2008.
- M. D. Petters and S. M. Kreidenweis. A single parameter representation of hygroscopic growth and cloud condensation nucleus activity. *Atmospheric Chemistry and Physics*, 7(8):1961–1971, 2007. doi: DOI:10.5194/acp-7-1961-2007.
- A. Petzold, K. Rasp, B. Weinzierl, et al. Saharan dust absorption and refractive index from aircraft-based observations during samum 2006. *Tellus B*, 61(1):118–130, 2009. ISSN 1600-0889. doi: 10.1111/j.1600-0889.2008.00383.x.
- C. Pierangelo, A. Chédin, S. Heilliette, N. Jacquinet-Husson, and R. Armante. Dust altitude and infrared optical depth from airs. *Atmospheric Chemistry and Physics*, 4(7):1813–1822, 2004.
- C. Pilinis, S. N. Pandis, and J. H. Seinfeld. Sensitivity of direct climate forcing by atmospheric aerosols to aerosol size and composition. *Journal of Geophysical Research: Atmospheres*, 100(D9):18739–18754, 1995.
- R. G. Pinnick, J. D. Pendleton, and G. Videen. Response for estimating the refractive index characteristics of the particle measuring systems active scattering aerosol spectrometer probes. *Aerosol Science and Technology*, 33(4):334–352, 2000. ISSN 0278-6826. doi: DOI10.1080/02786820050121530.
- A. Pluchino. Scattering photometer for measuring single ice crystals and evaporation and condensation rates of liquid droplets. *Journal of the Optical Society of America A*, 4(3):614, mar 1987. ISSN 1084-7529. doi: 10.1364/JOSAA.4.000614.
- I. B. Pollack, B. M. Lerner, and T. B. Ryerson. Evaluation of ultraviolet light-emitting diodes for detection of atmospheric no<sub>2</sub> by photolysis - chemiluminescence. *Journal of Atmospheric Chemistry*, 65(2):111–125, 2010. ISSN 1573-0662. doi: 10.1007/s10874-011-9184-3.
- C. A. Pope, R. T. Burnett, M. J. Thun, E. E. Calle, D. Krewski, K. Ito, and G. D. Thurston. Lung cancer, cardiopulmonary mortality, and long-term exposure to fine particulate air pollution. *Jama*, 287(9):1132–1141, 2002.

- S. J. Prais and C. B. Winsten. Trend estimators and serial correlation. Technical report, Cowles Commission discussion paper Chicago, 1954.
- L. F. Radke, P. V. Hobbs, and M. W. Eltgroth. Scavenging of aerosol particles by precipitation. *Journal of Applied Meteorology*, 19(6):715–722, 1980.
- J. Redemann, R. P. Turco, K. N. Liou, P. B. Russell, R. W. Bergstrom, B. Schmid, J. M. Livingston, P. V. Hobbs, W. S. Hartley, S. Ismail, R. A. Ferrare, and E. V. Browell. Retrieving the vertical structure of the effective aerosol complex index of refraction from a combination of aerosol in situ and remote sensing measurements during TARFOX. *Journal of Geophysical Research: Atmospheres*, 105(D8):9949–9970, 2000. ISSN 01480227. doi: 10.1029/1999JD901044.
- E. A. Reid, J. S. Reid, M. M. Meier, M. R. Dunlap, S. S. Cliff, A. Broumas, K. Perry, and H. Maring. Characterization of african dust transported to puerto rico by individual particle and size segregated bulk analysis. *Journal of Geophysical Research: Atmospheres*, 108(D19):n/a–n/a, 2003. ISSN 2156-2202. doi: 10.1029/2002JD002935. 8591.
- J. Reid, R. Koppmann, T. Eck, and D. Eleuterio. A review of biomass burning emissions part ii: intensive physical properties of biomass burning particles. *Atmospheric Chemistry and Physics*, 5(3):799–825, 2005.
- L. A. Remer and Y. J. Kaufman. Dynamic aerosol model: Urban/industrial aerosol. *Journal of Geophysical Research: Atmospheres*, 103(D12):13859–13871, 1998. ISSN 2156-2202. doi: 10.1029/98JD00994.
- L. A. Remer, S. Gass, D. A. Hegg, Y. J. Kaufman, and B. N. Holben. Urban / industrial aerosol : Ground-based Sun / sky radiometer. *Journal of Geophysical Research*, 102(96):16849–16859, 1997.
- L. A. Remer, Y. Kaufman, D. Tanré, S. Mattoo, D. Chu, J. V. Martins, R.-R. Li, C. Ichoku, R. Levy, R. Kleidman, et al. The modis aerosol algorithm, products, and validation. *Journal of the atmospheric sciences*, 62(4):947–973, 2005.
- D. Rosenfeld, U. Lohmann, G. B. Raga, et al. Flood or drought: how do aerosols affect precipitation? *Science*, 321(5894):1309–1313, 2008.
- P. B. Russell, M. Kacenelenbogen, J. M. Livingston, O. P. Hasekamp, S. P. Burton, G. L. Schuster, M. S. Johnson, K. D. Knobelspiesse, J. Redemann, S. Ramachandran, and B. Holben. A multiparameter aerosol classification method and its application to retrievals from spaceborne polarimetry. *Journal of Geophysical Research: Atmospheres*, 119(16):9838–9863, 2014. ISSN 2169-8996. doi: 10.1002/2013JD021411. 2013JD021411.

- T. B. Ryerson, E. J. Williams, and F. C. Fehsenfeld. An efficient photolysis system for fast-response no<sub>2</sub> measurements. *Journal of Geophysical Research: Atmospheres*, 105(D21):26447–26461, 2000. ISSN 2156-2202. doi: 10.1029/2000JD900389.
- P. E. Saide, D. A. Peterson, A. da Silva, B. Anderson, L. D. Ziemba, G. Diskin, G. Sachse, J. Hair, C. Butler, M. Fenn, J. L. Jimenez, P. Campuzano-Jost, A. E. Perring, J. P. Schwarz, M. Z. Markovic, P. Russell, J. Redemann, Y. Shinozuka, D. G. Streets, F. Yan, J. Dibb, R. Yokelson, O. B. Toon, E. Hyer, and G. R. Carmichael. Revealing important nocturnal and day-to-day variations in fire smoke emissions through a multiplatform inversion. *Geophysical Research Letters*, 42(9): 3609–3618, 2015. ISSN 1944-8007. doi: 10.1002/2015GL063737. 2015GL063737.
- K. Sassen and K. Liou. Scattering of Polarized Laser Light by Water Droplet, Mixed-Phase and Ice Crystal Clouds. Part I: Angular Scattering Patterns. *Journal of the Atmospheric Sciences*, 36:838–851, 1979.
- M. Schnaiter and G. Wurm. Experiments on light scattering and extinction by small, micrometer-sized aggregates of spheres. *Applied optics*, 41(6):1175–80, feb 2002. ISSN 0003-6935.
- M. Schulz, C. Textor, S. Kinne, Y. Balkanski, S. Bauer, T. Berntsen, T. Berglen, O. Boucher, F. Dentener, S. Guibert, et al. Radiative forcing by aerosols as derived from the aerocom present-day and pre-industrial simulations. *Atmospheric Chemistry and Physics*, 6(12):5225–5246, 2006.
- G. L. Schuster, B. Lin, and O. Dubovik. Remote sensing of aerosol water uptake. *Geophysical Research Letters*, 36(3):1–5, 2009. ISSN 00948276. doi: 10.1029/2008GL036576.
- SEAC4RS. Studies of Emissions and Atmospheric Composition, Clouds and Climate Coupling by Regional Surveys Data Archive, 2013.
- R. B. Seigel and S. C. van den Heever. Dust lofting and ingestion by supercell storms. *Journal of the Atmospheric Sciences*, 69(5):1453–1473, 2012.
- A. S. Shah, J. P. Langrish, H. Nair, D. A. McAllister, A. L. Hunter, K. Donaldson, D. E. Newby, and N. L. Mills. Global association of air pollution and heart failure: a systematic review and meta-analysis. *The Lancet*, 382(9897):1039–1048, 2013.
- V. Shcherbakov, O. Jourdan, C. Voigt, J.-F. Gayet, A. Chauvigne, A. Schwarzenboeck, A. Minikin, M. Klingebiel, R. Weigel, S. Borrmann, T. Jurkat, S. Kaufmann, R. Schlage, C. Gourbeyre, G. Febvre, T. Lapyonok, W. Frey, S. Molleker, and B. Weinzierl. Porous aerosol in degassing plumes of mt. etna and mt. stromboli. *Atmospheric Chemistry and Physics*, 16(18):11883–11897, 2016.

- T. Shingler, E. Crosbie, A. Ortega, M. Shiraiwa, A. Zuend, A. Beyersdorf, L. Ziemba, B. Anderson, L. Thornhill, A. E. Perring, J. P. Schwarz, P. Campazano-Jost, D. A. Day, J. L. Jimenez, J. W. Hair, T. Mikoviny, A. Wisthaler, and A. Sorooshian. Airborne characterization of subsaturated aerosol hygroscopicity and dry refractive index from the surface to 6.5 km during the seac4rs campaign. *Journal of Geophysical Research: Atmospheres*, 121(8):4188–4210, 2016.
- S. V. Stehman. Selecting and interpreting measures of thematic classification accuracy. *Remote sensing of Environment*, 62(1):77–89, 1997.
- A. Stewart-Oaten, W. W. Murdoch, and K. R. Parker. Environmental impact assessment:” pseudoreplication” in time? *Ecology*, 67(4):929–940, 1986.
- T. Stocker. *Climate change 2013: the physical science basis: Working Group I contribution to the Fifth assessment report of the Intergovernmental Panel on Climate Change*. Cambridge University Press, 2014.
- N. G. Sultanova, I. D. Nikolov, and C. D. Ivanov. Measuring the refractometric characteristics of optical plastics. *Optical and Quantum Electronics*, 35(1):21–34, 2003. ISSN 03068919. doi: 10.1023/A:1021811200953.
- B. Svenningsson, J. Rissler, E. Swietlicki, M. Mircea, M. Bilde, M. C. Facchini, S. Decesari, S. Fuzzi, J. Zhou, J. Mønster, and T. Rosenørn. Hygroscopic growth and critical supersaturations for mixed aerosol particles of inorganic and organic compounds of atmospheric relevance. *Atmospheric Chemistry and Physics*, 6(7):1937–1952, 2006. doi: 10.5194/acp-6-1937-2006.
- M. a. Sviridenkov, S. S. Vlasenko, and E. Y. Nebosko. Retrieval of the aerosol optical and microphysical parameters from the data of measurements by means of Aurora 4000 nephelometer. In O. A. Romanovskii, editor, *Proc. of SPIE, 20th International Symposium on Atmospheric and Ocean Optics: Atmospheric Physics*, volume 9292, pages 92922U–1–92922U–6, nov 2014. doi: 10.1117/12.2076156.
- T. Takemi, M. Yasui, J. Zhou, and L. Liu. Role of boundary layer and cumulus convection on dust emission and transport over a midlatitude desert area. *Journal of Geophysical Research: Atmospheres*, 111(D11):n/a–n/a, 2006. ISSN 2156-2202. doi: 10.1029/2005JD006666. D11203.
- M. Tanaka, T. Takamura, and T. Nakajima. Refractive index and size distribution of aerosols as estimated from light scattering measurements. *Journal of Applied Meteorology*, 22(7):1253–1261, 1983.
- I. Tang. Chemical and size effects of hygroscopic aerosols on light scattering coefficients. *Journal of Geophysical Research*, 101(D14):19245–19250, 1996.

- I. Tegen, P. Hollrig, M. Chin, I. Fung, D. Jacob, and J. Penner. Contribution of different aerosol species to the global aerosol extinction optical thickness: Estimates from model results. *Journal of Geophysical Research: Atmospheres*, 102(D20): 23895–23915, 1997.
- G. E. Thomas and K. Stamnes. *Radiative transfer in the atmosphere and ocean*. Cambridge University Press, 2002.
- D. S. Thomson, M. E. Schein, and D. M. Murphy. Particle analysis by laser mass spectrometry wb-57f instrument overview. *Aerosol Science & Technology*, 33(1-2): 153–169, 2000.
- O. B. Toon and J. B. Pollack. The Optical Constants of several Atmospheric Aerosol Species: Ammonium Sulfate, Aluminium Oxide, and Sodium Chloride. *Journal of Geophysical Research*, 81(33):5733–5748, 1976.
- O. B. Toon, H. Maring, J. Dibb, R. Ferrare, D. J. Jacob, E. J. Jensen, Z. J. Luo, G. G. Mace, L. L. Pan, L. Pfister, K. H. Rosenlof, J. Redemann, J. S. Reid, H. B. Singh, Robert Yokelson, P. Minnis, G. Chen, K. W. Jucks, and A. Pszenny. Planning, implementation and scientific goals of the Studies of Emissions and Atmospheric Composition, Clouds and Climate Coupling by Regional Surveys (SEAC4RS) field mission. *Journal of Geophysical Research: Atmospheres*, 121:4967–5009, 2016. ISSN 2169897X. doi: 10.1002/2015JD024297.
- O. Torres, A. Tanskanen, B. Veihelmann, C. Ahn, R. Braak, P. K. Bhartia, P. Veefkind, and P. Levelt. Aerosols and surface uv products from ozone monitoring instrument observations: An overview. *Journal of Geophysical Research: Atmospheres*, 112(D24), 2007.
- P. Tulet, K. Crahan-Kaku, M. Leriche, B. Aouizerats, and S. Crumeyrolle. Mixing of dust aerosols into a mesoscale convective system. *Atmospheric Research*, 96(2):302–314, 2010. ISSN 0169-8095. doi: <http://dx.doi.org/10.1016/j.atmosres.2009.09.011>. 15th International Conference on Clouds and Precipitation.
- S. Twomey. The influence of pollution on the shortwave albedo of clouds. *Journal of the atmospheric sciences*, 34(7):1149–1152, 1977.
- A. Van Donkelaar, R. V. Martin, M. Brauer, R. Kahn, R. Levy, C. Verduzco, and P. J. Villeneuve. Global estimates of ambient fine particulate matter concentrations from satellite-based aerosol optical depth: development and application. *Environmental health perspectives*, 118(6):847, 2010.
- H. Volten, O. Munoz, E. Rol, J. Haan, V. W, and J. Hovenier. Scattering matrices of mineral aerosol particles at 441.6 nm and 632.8 nm. *Journal of Geophysical Research*, 106(D115):17,375–17,401, 2001.

- J. M. Wallace and P. V. Hobbs. *Atmospheric science: an introductory survey*, volume 92. Academic press, 2006.
- R. E. Weiss, V. N. Kapustin, and P. V. Hobbs. Chain-aggregate aerosols in smoke from the kuwait oil fires. *Journal of Geophysical Research: Atmospheres*, 97(D13): 14527–14531, 1992. ISSN 2156-2202. doi: 10.1029/92JD01372.
- M. Wendisch, A. Keil, and A. Korolev. Fssp characterization with monodisperse water droplets. *Journal of Atmospheric and Oceanic Technology*, 13(6):1152–1165, 1996.
- M. Wendisch, H. Coe, D. Baumgardner, J. Brenguier, V. Dreiling, M. Fiebig, P. Formenti, M. Hermann, M. Krämer, Z. Levin, et al. Aircraft particle inlets: State-of-the-art and future needs. *Bulletin of the American Meteorological Society*, 85(1): 89–91, 2004.
- R. West and L. Doose. Laboratory measurements of mineral dust scattering phase function and linear polarization. *Journal of Geophysical Research*, 102(D14): 16,871–16,881, 1997.
- D. L. Westphal and O. B. Toon. Simulations of microphysical, radiative, and dynamical processes in a continental-scale forest fire smoke plume. *Journal of Geophysical Research*, 96(D12):22379–22400, 1991. ISSN 0148-0227. doi: DOI10.1029/91jd01956.
- M. S. Wong, J. E. Nichol, and K. H. Lee. An operational MODIS aerosol retrieval algorithm at high spatial resolution, and its application over a complex urban region. *Atmospheric Research*, 99(3-4):579–589, 2011. ISSN 01698095. doi: 10.1016/j.atmosres.2010.12.015.
- L. Wu and Q.-C. Zeng. Classifying asian dust aerosols and their columnar optical properties using fuzzy clustering. *Journal of Geophysical Research: Atmospheres*, 119(5):2529–2542, 2014. ISSN 2169-8996. doi: 10.1002/2013JD020751.
- F. Xu, O. Dubovik, P.-W. Zhai, D. J. Diner, O. V. Kalashnikova, F. C. Seidel, P. Litvinov, A. Bovchaliuk, M. J. Garay, G. van Harten, and A. B. Davis. Joint retrieval of aerosol and water-leaving radiance from multispectral, multiangular and polarimetric measurements over ocean. *Atmospheric Measurement Techniques*, 9(7):2877–2907, 2016. ISSN 1867-8548. doi: 10.5194/amt-9-2877-2016.
- M. a. Yamasoe, Y. J. Kaufman, O. Dubovik, L. a. Remer, B. N. Holben, and P. Ar-taxo. Retrieval of the real part of the refractive index of smoke particles from Sun/sky measurements during SCAR-B. *Journal of Geophysical Research*, 103(98):31893–31902, 1998. ISSN 0148-0227. doi: 10.1029/98JD01211.

- A. T. Young. Revised depolarization corrections for atmospheric extinction. *Applied optics*, 19(20):3427–3428, 1980.
- H. Yu, Y. Kaufman, M. Chin, G. Feingold, L. Remer, T. Anderson, Y. Balkanski, N. Bellouin, O. Boucher, S. Christopher, et al. A review of measurement-based assessments of the aerosol direct radiative effect and forcing. *Atmospheric Chemistry and Physics*, 6(3):613–666, 2006.
- J. Zhang, J. S. Reid, D. L. Westphal, N. L. Baker, and E. J. Hyer. A system for operational aerosol optical depth data assimilation over global oceans. *Journal of Geophysical Research: Atmospheres*, 113(D10), 2008.
- F. Zhao. Determination of the complex index of refraction and size distribution of aerosols from polar nephelometer measurements. *Applied optics*, 38(12):2331–2336, 1999.
- F. Zhao, Z. Gong, H. Hu, M. Tanaka, and T. Hayasaka. Simultaneous determination of the aerosol complex index of refraction and size distribution from scattering measurements of polarized light. *Applied optics*, 36(30):7992–8001, 1997.
- L. D. Ziemba, A. J. Beyersdorf, G. Chen, C. A. Corr, S. N. Crumeyrolle, G. Diskin, C. Hudgins, R. Martin, T. Mikoviny, R. Moore, M. Shook, K. L. Thornhill, E. L. Winstead, A. Wisthaler, and B. E. Anderson. Airborne observations of bioaerosol over the southeast united states using a wideband integrated bioaerosol sensor. *Journal of Geophysical Research: Atmospheres*, 121(14):8506–8524, 2016. ISSN 2169-8996. doi: 10.1002/2015JD024669. 2015JD024669.

